Magneto-Capillary Dynamics of Particles at Curved Liquid Interfaces

Wenjie Fei

Submitted in partial fulfillment of the
requirements for the degree
of Doctor of Philosophy
in the Graduate School of Arts and Sciences

COLUMBIA UNIVERSITY

2019

ABSTRACT

Magneto-Capillary Dynamics of Particles at Curved Liquid Interfaces

Wenjie Fei

The ability to manipulate colloidal particles with magnetic fields has profound applications both in industry and academic research ranging from automobile shock absorbers to robotic micro-surgery. Many of these applications use field gradients to generate forces on magnetic objects. Such methods are limited by the complexity of the required fields and by the magnitude of the forces generated. Spatially uniform fields only apply torques, but no forces, on magnetic particles. However, by coupling the particles' orientation and location, even static uniform fields can drive particle motion.

We demonstrate this idea using particles adsorbed at curved liquid interfaces. We first review the intersection between active colloidal particles and (passive) particles at the fluid-fluid interface (chapter 1), followed by the introduction of magnetism, magnetic manipulation, and magnetic Janus particle fabrication techniques (chapter 2). In chapter 3, we use magnetic Janus particles with amphiphilic surface chemistry adsorbed at the spherical interface of water drop in decane as a model system to study particle response to a uniform field. Owing to capillary constraints, Janus particles adsorbed at curved interfaces will move in a uniform magnetic field to align their magnetic moment parallel to the applied field. This phenomenon is labeled as the magneto-capillary effect in this thesis. As explained quantitatively by a simple model, the effective magnetic force on the particle induced by static uniform field scales linearly with the curvature of the interface. For particles adsorbed on small droplets such as those found in emulsions, these magneto-capillary forces can far exceed those due to magnetic field gradients in both magnitude and range. The time-varying fields induce more complex particle motions that persist as long as the field is applied (chapter 4). Depending on the angle and frequency of a precessing

field, particles orbit the drop poles or zig-zag around the drop equator. Magneto-capillary effects are not limited to Janus particles. Similar behaviors are observed in commercially available carbonyl iron particles. Periodic particle motion at the liquid interface can drive fluid flows inside the droplets, which may be useful for enhancing mass transport in droplet micro-reactors.

The magneto-capillary effect at curved liquid interfaces offers new capabilities in magnetic manipulation: even static uniform fields can propel magnetic particles and the use of time-varying fields leads to steady particle motions of increasing complexity. These experimental demonstrations and the quantitative models that accompany them should both inspire and enable continued innovations in the use of magnetic fields to drive active processes in colloid and interface science. The final chapter highlights some specific directions for future work in this area.

Table of Contents

List of Figures

Acknowledgements

First and foremost I would like to thank my advisor, Professor Kyle Bishop. I am grateful to him for welcoming me to his research group, where I had the opportunity to work with many brilliant and innovative students. I appreciate his patience, guidance, and support during my thesis project and for his valuable insights and pieces of advice that helped me both academically and professionally.

I would like to thank my committee members, Professor Sanat Kumar, Professor Oleg Gang, Professor Allie Obermeyer, and Professor Ilona Kretzchmar for their insightful discussions and valuable suggestions on my thesis work. Professor Paul Chaikin and Professor Michelle Driscoll at New York University have provided me much help in understanding magnetic particle responses in applied rotating fields.

The faculty and staff at Penn State University and Columbia University have been instrumental in helping me during my time as a PhD student including: Professor Darrell Velegol and his student Astha Garg, for their insights on planning micro-particle experiments with optical microscopy, Rachel Fitzgerald, Israel Rodriguez and Roger Dunlap, who helped organize the move to Columbia, Bonnie (Boyeon) Choi for SQUID measurement, Cathy Krause, Kathy Marte-Garcia, Rezarta Binaj, Emely Aquino, Irina Katz and Ariel Sanchez for administrative help at Penn State and Columbia.

Many past and present members of Bishop research group have offered much help. Sun Haera Shin, Hee Young Lee help me get started in the lab. Charles Cartier, Syeda Sabrina, Allan Brooks, John Schreck, Dimitri Livitz, Yang Gu, Yong Dou, Kiran Dhatt-Gauthier, Zhengyan Zhang, Lisa Tran, and Ghanim Hableel offered great insights in presentation styles and experiments. I appreciate the help of undergraduate student Peter Tzelios.

Lastly, I would like to thank my parents Chunlei, Lianhua and my boyfriend Yuexiao, for their endless love and support.

Chapter 1

Active colloidal particles at fluid-fluid interfaces

1.1 Abstract

This Review explores the intersection between two important fields of colloid and interface science – that of active colloidal particles and of (passive) particles at fluid-fluid interfaces. The former uses energy input at the particle level to propel particle motions and direct dynamic assemblies. The latter relies on the spontaneous adsorption of particles at fluid interfaces to modify the interfacial energy, rheology, and permeability of biphasic materials. Here, we address two key questions that connect these otherwise distinct fields of study. How do liquid interfaces influence the dynamics of active or driven colloidal particles? How can particle activity influence the dynamics of liquid interfaces? These questions motivate the pursuit of active particle surfactants that move and organize at fluid interfaces to perform useful functions such as enhancing mass transport or modulating interfacial properties. Drawing examples from the literature, we discuss how fluid interfaces can provide a unique environment for the study of active colloids, how surface tension can be harnessed to propel particle motions, and how capillary interactions can be activated to achieve dynamically tunable emulsions and foams. We highlight opportunities for the future study and application of active particles at liquid interfaces.

1.2 Introduction

Two growing fields of colloid and interface science – that of active colloidal particles and of particles at fluid-fluid interfaces – are increasingly overlapping. This Review examines the intersection between these fields, highlighting some of the open questions and new opportunities for both communities (Fig. 1.1). We begin with a brief overview of the core pursuits within each field, directing the reader to more thorough review articles where

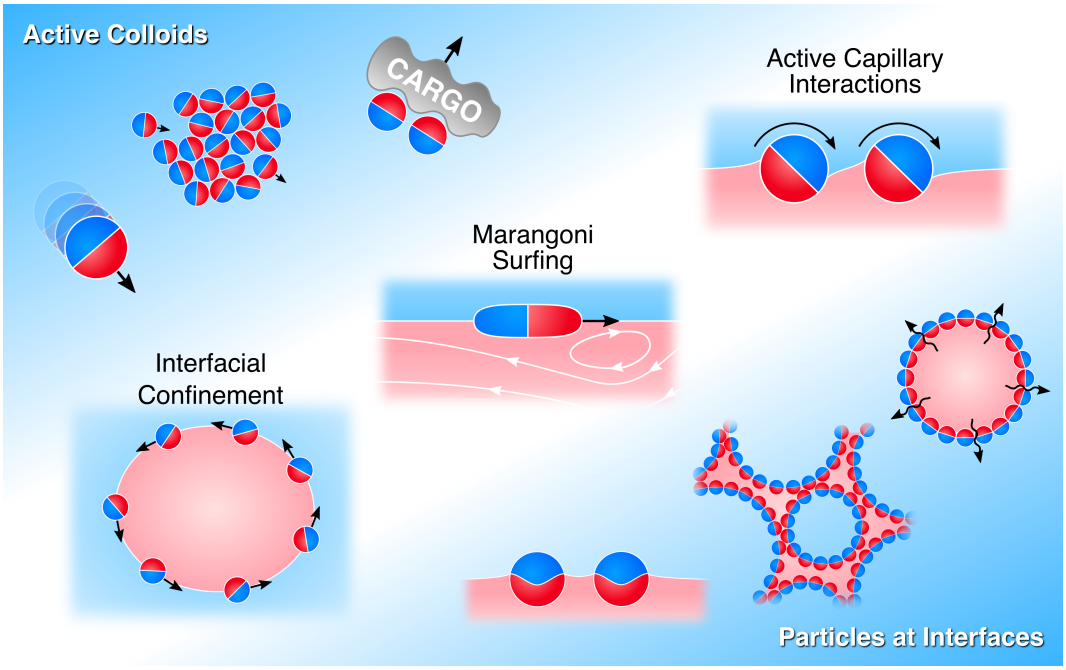

Figure 1.1: The three topics of this Review lie at the intersection between the areas of active colloidal particles (left) and particles at fluid-fluid interfaces (right). Interfacial confinement: fluid interfaces provide a unique 2D environment for the study of self-propelled particles. Marangoni surfers: self-generated surface tension gradients provide a versatile strategy for propelling active particles. Active capillary interactions: external fields and shape-changing particles provide a basis for tunable interactions that guide dynamic particle assemblies.

available.

1.2.1 Active Colloidal Particles

Active colloidal particles harness energy from their environment to power directed motions relative to their fluid surroundings [15, 16, 17, 18, 19]. Interest in these colloidal motors spans many disciplines and a variety of fundamental and applied research topics. The study of active colloids is motivated by the following key questions: How do inanimate particles propel themselves through viscous fluids? How can their motions be guided by external stimuli or environmental cues? What types of collective behaviors can arise within

ensembles of active particles? How can their unique characteristics and capabilities enable new applications?

A wide variety of propulsion mechanisms have been applied to power the motion of active particles at the micro- and nanoscales. Arguably the most well-studied is a form of phoretic self-propulsion, whereby chemical reactions at the particle surface create local gradients in scalar quantities such as the electric potential, chemical concentration, or temperature that drive particle motions via interfacial flows [20]. Such phoretic swimmers rely on asymmetries in the particle shape or surface chemistry to direct linear and/or rotation motions through viscous fluids at speeds of ~ 10 μm/s. Similarly, active emulsion droplets generate local gradients in the concentration of surface-active species, which drive Marangoni flows that propel drop motions [21]. Another class of active particles relies on the chemical generation of gas bubbles and their directed release to propel low-Reynolds number "rockets" at speeds of $\sim 10^3$ body lengths/s [22]. In addition to chemical reactions, external fields are also used to power the autonomous motion of colloidal particles. Uniform magnetic and electric fields induce torques on particle dipoles, which can drive active motions through hydrodynamic coupling of rotation and translation [23]. External fields can also power force- and torque-free motions such as those due to electrokinetic flows [18] or nonreciprocal swimming gaits [24]. Ultrasound offers a promising energy source for powering colloidal motors that allows for remote actuation using bio-compatible stimuli [25]. The above mechanisms are effective in viscous fluids; however, additional swimming strategies become possible in complex, non-Newtonian fluids [26]. Looking forward, the diversity of propulsion mechanisms is likely to grow further in pursuit of ever faster, safer, and more efficient motors.

Once the particles are moving, the focus shifts toward directing their motions with increasing levels of control. This effort starts with the particles themselves, as the type of

motion (e.g., translation or rotation) is often dictated by the particles' symmetry. Colloidal motors of various shapes and sizes are fabricated by a range of techniques from templated electrodeposition and physical vapor deposition [15, 27] to bulk colloidal synthesis [28]. During the fabrication process, magnetic materials are commonly incorporated to enable steering of self-propelled particles by external magnetic fields [15]. Active colloids can also move in response to gradients in their environment through the non-biological analogs of chemotaxis, phototaxis, gravitaxis, and rheotaxis [19]. When moving near solid walls, active particles sense the nearby boundaries through the hydrodynamic and chemical fields they create, thereby enabling navigation within structured environments [19, 17, 18].

Beyond the dynamics of individual particles, ensembles of active colloids show a variety of collective behaviors reminiscent of schooling and flocking among living organisms [3]. Such systems provide synthetic realizations of active matter in which energy is converted to motion at the level of discrete microscopic components [29]. These nonequilibrium systems allow for new types of material organization such as "living crystals" of self-propelled particles [19] and self-organized vortices of active colloidal rollers [23]. Owing to hydrodynamic coupling among self-propelled particles, dispersions of active colloids can generate chaotic flows at low Reynolds numbers – so-called active turbulence – first discovered in suspensions of motile bacteria [18]. The non-Brownian motions of active colloids can also be harnessed to do useful work such as pushing or rotating passive objects of asymmetric shapes [18]. These and other systems of active colloids remain fertile ground for the discovery and investigation of dynamic (dissipative) self-organization.

Progressing in parallel to these fundamental developments, a variety of applied research topics have emerged that seek to use active colloids to address challenges ranging from precision surgery at the microscale to the remediation of polluted waters. In biomedicine,

the science fiction vision of the Fantastic Voyage is giving way to a reality, in which micro- and nanorobots are capable of delivering therapeutic payloads, performing precision surgery, diagnosing disease, and neutralizing toxins *in vivo* [30]. The ability of active colloids to navigate complex environments and deliver cargo to targeted locations is also being used to perform lab-on-a-chip operations [31]. The fluid flows induced by particle motions can serve to enhance rates of mass transfer to and from the particle surface, with emerging applications in water remediation [32] and chemical detection [33]. Despite these promising directions, commercial technologies based on active colloids have yet to materialize since their discovery more than a decade ago. By contrast, the use of passive colloidal particles at fluid-fluid interfaces is ubiquitous to many industries such as cosmetics, food, and petroleum. One objective of this Review is to consider how particle activity can contribute new capabilities to these existing applications.

1.2.2 Particles at Fluid-Fluid Interfaces

Colloidal particles adsorb spontaneously at fluid-fluid interfaces thereby modifying the interfacial energy, rheology, and permeability [34, 35, 36]. Such particle-laden interfaces are widely studied for their relevance to the stabilization of emulsions [37, 38] and foams [39, 40] and to the development of new materials such as bijels [41], capsules [42], liquid marbles [43], and lightweight composites [44]. In this brief overview, we address the following questions that arise in the study of particles at interfaces: Why do solid particles adsorb at fluid-fluid interfaces? How do adsorbed particles interact and assemble with one another? How do such particles influence the mechanical and rheological properties of the interface? How do the properties of particle-laden interfaces support their widespread application?

The adsorption of a solid particle at the fluid-fluid interface is driven by the reduction

in the interfacial energy of the three-phase system [35]. Adsorption is most favorable when the particle is wetted equally by the respective fluids corresponding to a contact angle of 90^o. Even for nanoscale particles, this process is effectively irreversible due to high adsorption energies, typically many orders of magnitude larger than the thermal energy. Particles of anisotropic shapes such as rods or disks adsorb even more strongly than spheres and adopt a preferred orientation – one that maximizes the interfacial area occupied by the particle [35, 45]. Amphiphilic Janus particles with both hydrophobic and hydrophilic surface regions adsorb up to three times more strongly than homogeneous particles of comparable size with important implications to the thermodynamics of emulsion formation [46, 38]. At the nanoscale, particle adsorption is strongly influenced by the use of capping ligands which rearrange upon changes in their environment [47]; similar relaxation processes occur also for microgel particles [48]. While adsorption is often viewed from a thermodynamic perspective, the dynamics of wetting can be remarkably slow and depends on particles' nanoscale surface features [49].

Once adsorbed at the interface, particles experience a two-dimensional environment quite different from that of a bulk fluid. Their presence creates local disturbances in the shape of the interface that extend over long distances [50]. When the disturbances of two or more particles overlap, they modify the interfacial area and thereby the energy of the interface. The resulting capillary interactions can direct the formation of particle aggregates or ordered assemblies, which depend strongly on particle shape and surface chemistry [50]. Such aggregation is often opposed by repulsive electrostatic interactions, which are mediated by dipolar fields that extend unscreened through the non-polar fluid [51]. Guided by these long ranged interactions, the fluid interface provides a defect-free environment for the assembly of colloidal materials [52, 53].

At sufficiently high densities, steric interactions among particles can transform a fluid interface into an glassy solid, in which particles become "jammed" under the force of interfacial tension. This jamming phenomena provides a basis for the kinetic stabilization of Pickering emulsions [37] and for the realization of new materials such as bijels (for bicontinuous interfacially jammed emulsion gel) [41]. In emulsions, the coalescence of two particle-laden drops acts to decrease the interfacial area without significantly reducing the number of particles at the interface. After several such events, the drop surface becomes completely covered with solid-like barrier that resists further coalescence. The rheology of this particle-rich layer is strongly influenced by the shape of the individual particles. Anisotropic particles typically form stronger networks reinforced by mechanical entanglements and/or capillary interactions [50]. Rod-like particles with high aspect ratios are particularly effective in stabilizing the thin liquid films that accompany foam formation [39, 40]. It remains an outstanding challenge to understand how the particle microstructure determines the interfacial rheology and thereby the bulk properties of multiphase materials [54, 55, 56].

The ability of inert particles to stabilize emulsions and foams without the addition of surface active chemicals makes them particularly attractive for applications in food products, cosmetics, and biomedicine [57, 58]. In this context, bio-based materials such as proteins, cellulose, and fats are actively pursued for their ability to stabilize biphasic dispersions [40]. Beyond these traditional applications, particle-laden interfaces are increasingly used to create new materials that take advantage of their tunable permeability, light weight, and responsiveness to external stimuli [44, 38, 42]. Particles at fluid-fluid interfaces are also well positioned to perform catalytic functions such as accelerating biphasic reactions [59]. As discussed below, the incorporation of field responsiveness and other types of particle activ-

ity into these material systems offers the potential for enhanced functionality and tunable control.

1.2.3 Scope of the Review: Active particles at fluid-fluid interfaces

This Review examines the intersection of these two communities where their respective frontiers merge to form an exciting new field of study (Fig. 1.1). From the perspective of active colloids, fluid interfaces provide a unique environment for constraining particle motions in two-dimensions without the retarding effects of solid boundaries (section 1.3). Such interfaces need not be planar and allow for study of active matter on curved manifolds of various topologies. Owing to the importance of surface tension, fluid interfaces offer new strategies for the conversion of energy to motion at colloid scales (section 1.4). Active particles that create and respond to local surface tension gradients – so-called Marangoni surfers – can propel themselves at high speeds, navigate structured environments, and organize to form dynamic assemblies. From the complementary perspective of particles at interfaces, the introduction of particle activity using external fields allows for modulating capillary interactions to control how particles move, interact, and assemble (section 1.5). The use of such stimuli to control particle microstructure at the fluid-fluid interface enables responsive emulsions, foams, and capsules with dynamically tunable properties.

For each of these topics, we discuss the basic physics underlying the phenomena and highlight specific examples from the recent (and no-so-recent) literature. Rather than a comprehensive survey, we aim to provide a coherent synthesis of the key features that characterize the behaviors of active particles at liquid interfaces. These features often derive from the basic characteristics both of fluid-fluid interfaces (e.g., dimensionality, curvature, surface tension) and of particle activity (e.g., fluid flow, dissipation). From this high al-

titude, our coverage is necessary superficial but hopefully nontrivial and accessible to a wide audience of chemists, physicists, material scientists, and engineers. Overall, it is our hope that this Review will stimulate further interest in the following complementary questions: How do fluid interfaces influence the dynamics of active colloidal particles? How can particle activity influence the dynamics of fluid interfaces? These questions motivate the pursuit of active particle surfactants that move and organize at fluid interfaces to perform useful functions such as enhancing mass transport or modulating interfacial properties. We discuss these and other opportunities in our concluding remarks (section 1.6).

1.3 Interfacial Confinement of Active Colloids

Fluid-fluid interfaces provide a useful environment in which to study the motions of active colloidal particles. This environment is distinguished from that of bulk fluids by several factors such as the dimensionality, symmetry, and curvature. Obviously, interfaces are two-dimensional (2D). The dynamics of active particles in 2D can differ both quantitatively and qualitatively from their corresponding motions in the bulk. Moreover, fluid interfaces lack the mirror symmetry of bulk fluids, which enables particles to adopt preferred orientations and positions relative to the interface. Differences in the viscosities of the respective fluids acts to couple the translation and rotation of active particles. Capillary forces and torques serve to position particles at interfaces and contribute new dissipation mechanisms that impact particle motions. Fluid-fluid interfaces can also bend to form environments of constant mean curvature characterized by different topologies. The collective behaviors of active colloids are strongly influenced by such topological constraints. In this section, we discuss examples that illustrate the varied effects of interfacial confinement on the motions of active colloids.

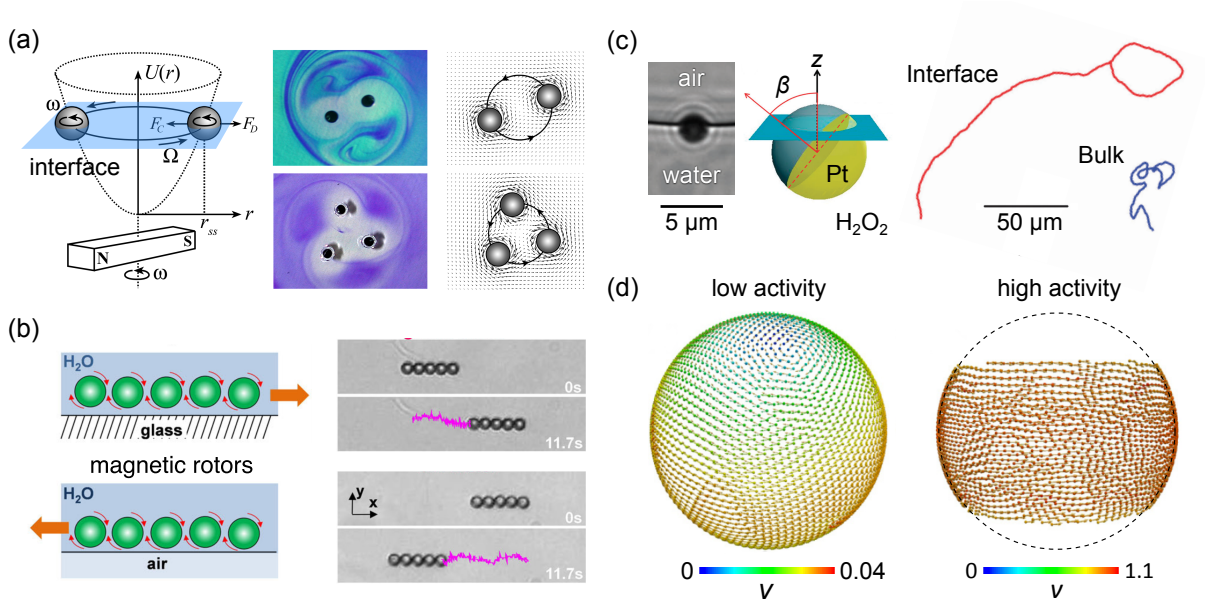

Figure 1.2: (a) Dynamic self-assembly of rotating particles at the liquid-air interface. (Adapted from Ref [1] with permission of The Royal Society of Chemistry.) (b) Colloidal microworms propelled by rotating magnetic fields move in opposite directions near water-glass and water-air interfaces. (Adapted with permission from Ref [2]. Copyrighted by the American Physical Society.) (c) Enhanced motion of active Janus spheres at the water-air interface. (Adapted from Ref [3] with permission of The Royal Society of Chemistry.) (d) Swarms of self-propelled particles on a sphere. (Adapted with permission from Ref [4]. Copyrighted by the American Physical Society.)

1.3.1 Dimensionality

The adsorption of active particles at fluid-fluid interfaces provides a convenient strategy by which to constrain their motion to 2-dimensions. Particle motions normal to the interface are prohibited by restoring forces due to surface tension; motions tangent to the interface give rise to drag forces comparable to those experienced by particles in the bulk. For example, millimeter-scale magnetic particles assemble at a liquid-air interface when actuated by a rotating magnetic field (Fig. 1.2a) [60]. Here, the interface simply limits particle motions to 2-dimensions without introducing additional physics such as capillary interactions. The assembly process, which involves repulsive hydrodynamic interactions and a confining magnetic potential, is faithfully reproduced by simulations of particles rotating in an unbounded fluid [61].

Planar gas-liquid interfaces are particularly useful for confining active particles as the gas phase imparts a negligible stress tangent to the interface. This boundary condition is identical to that of mirror symmetry for analogous bulk flows. In other words, the physics of active particles in an unbounded fluid with one plane of mirror symmetry is nearly identical to that at a gas-liquid interface. Propulsion mechanisms for active colloids that operate in bulk liquids can therefore be applied to power particle motions at interfaces. For example, self-electrophoretic mechanisms [62, 63] have been used to propel chemically-powered motors [64] and radio-powered diodes [65] across water-air interfaces.

1.3.2 Viscosity Contrast

The motions of active colloids are inevitably accompanied by hydrodynamic flows, which depend on the proximity and the nature of fluid boundaries. Such boundaries introduce the possibility of hydrodynamic coupling between particle translation and rotation even

for high-symmetry particles such as spheres [66]. This coupling allows for linear particle motions powered by driving torques due to magnetic [2, 67] or electric [68] fields. Most commonly, torque-driven particles move along a solid substrate in a manner similar to no-slip rolling but at slower speeds [67] (Fig. 1.2b). When the same particles "roll" along a fluid-air interface, they move in the opposite direction in what might be described as the colloidal moonwalk [2] (Fig. 1.2b). This counter-intuitive behavior is simple to understand: the side of the particle near the interface experience less viscous stress than the opposite side. The particle is therefore "rolling" along the liquid above rather than the interface below.

The motion of self-phoretic colloids is similarly influenced by rotation-translation coupling near fluid boundaries. Most experimental [69, 70] and theoretical [71, 72] studies have focused on the case of active colloids near solid boundaries. Less is known about the motion of self-phoretic colloids moving near fluid-fluid interfaces. Recent theoretical studies of active Janus particles moving at liquid interfaces by self-diffusiophoresis show how the viscosity contrast determines the existence of stable swimming modes [73]. The motion of an active particle at the interface causes the particle to rotate toward the more viscous fluid. This rotation may serve to inhibit or enhance particle motion depending on the source and nature of particle activity [73].

1.3.3 Capillary Forces

When active particles are adsorbed at an interface, their rotation is further constrained by capillary forces. These forces have been shown to alter the motions of self-phoretic colloids by enhancing the persistence of their swimming direction [3]. When a Pt-silica Janus sphere is deposited onto the surface of an aqueous solution of hydrogen peroxide fuel, it

exhibits self-phoretic motions at speeds similar to those observed in the bulk [3] (Fig. 1.2c). Surprisingly, however, the persistence length of the particle trajectories is nearly ten times greater at the interface than in the bulk, suggesting a reduction in the rate of rotational diffusion. This reduction is believed to arise from the enhanced drag due to thermally activated fluctuations of the interface at the the three phase contact line [74] (although see [75]).

Capillary forces also serve to prohibit particle rotations about the two axes parallel to the interface. As a result, active particle motions are strongly influenced by the initial particle orientation (e.g., on the angle β in Fig. 1.2c) [76, 77]. Ideally, this orientation is uniquely determined by the particle's shape and surface chemistry. In practice, however, surface roughness leads to pinning of the three phase contact line in non-equilibrium configurations that depend strongly on the system preparation. Variability in the orientation of active Janus particles at liquid interfaces can result in mixed populations of motile and non-motile particles [77]. The development of facile methods for the reliable and reproducible deposition of active particles at fluid interfaces would likely encourage more researchers to enter this emerging area.

1.3.4 Curvature and Topology

The examples above have focused on the motion of active colloids at or near planar interfaces. The collective behavior of such active matter becomes even richer when the particles are constrained to move on curved interfaces like that of a spherical drop. In general, the realization of long-ranged order on a sphere necessitates the introduction of topological defects. For example, a hexagonal lattice of colloidal particles requires 12 pentagonal defects in order to wrap itself onto a sphere [78]. Similarly, a nematic phase of aligned particles

on a sphere requires defects whose topological charge adds up to +2, where a charge of s denotes a defect that rotates the director field by $2\pi s$. In other words, you can't comb a hairy ball flat without creating a cowlick (actually two, each with a topological charge of +1). These topological constraints have important implications for the organization of active matter with nematic alignment such as that formed by active microtubule assemblies [79] or self-propelled particles [4].

Here, we highlight one simulation study that illustrates how interface topology can influence the collective dynamics of active particles [4] (Fig. 1.2d). In this model system, self-propelled particles move in two-dimensions with a constant speed and interact with one another through both soft repulsion and polar alignment. In the plane, such particles organize to into stable flocks in which all particles move in a common direction. By contrast, when confined to the surface of a sphere, the particles form two vortices – that is, two +1 topological defects (Fig. 1.2d) [4]. As the strength of particle activity is increased relative to that of repulsive interactions, the particles become concentrated within a circulating band. In this way, topological constraints can served to channel particle activity to create new types of organization.

1.4 Marangoni Surfers: Propulsion, Interactions, & Assemblies

The surface tension of fluid-fluid interfaces and its dependence on temperature and surfactant concentration enable powerful strategies for propelling active particles [80, 81, 82, 83]. These Marangoni surfers use chemical reactions or external energy inputs to create asymmetries in the tension of the surrounding interface. The resulting forces and torques propel particles at high speeds toward regions of higher surface tension, inducing flows that rein-

force the asymmetric temperature or surfactant fields. Particle motions are accompanied by Marangoni flows [84] due to surface tension gradients that contribute to interactions among particles and with system boundaries. These interactions can be attractive or repulsive and enable the formation of dynamic assemblies and particle swarms. In this section, we describe the recent progress in understanding the hydrodynamics of Marangoni surfers, directing their motions with programmable asymmetries, and exploring their collective behaviors.

1.4.1 Viscous Marangoni Propulsion

Hydrodynamic models of Marangoni surfing have focused largely on a regime, in which particle motions and the accompanying flows do not alter the distribution of temperature or surfactant concentration. This type of viscous Marangoni propulsion was first studied in the context of a circular disk moving at the surface of a viscous liquid [5]. The disk generates a surface active species on one side and consumes it on the other, thereby maintaining a non-uniform concentration around its perimeter (Fig. 1.3a, left). The resulting variations in the surface tension induce a net force on the disk in the direction of lower surfactant concentration. This driving force is balanced by the viscous drag due both to the motion of the disk and to the Marangoni flows caused by the surface tension gradients (Fig. 1.3a, right). By assuming that the interfacial tension decreases linearly with surface concentration as $\gamma = \gamma_0 - \beta\Gamma$, the disk velocity can be determined analytically, in qualitative agreement with the following estimate. The driving force scales as the magnitude of the surface tension variations times the disk cross-section, $F \sim \beta\Delta\Gamma a$; the viscous drag on the disk as $F \sim \eta a U$. Equating these forces, we obtain the characteristic disk velocity $U \sim \beta\Delta\Gamma/\eta$. Under dilute conditions (such that $\beta \sim k_B T$), even small variations in the surface concentration of order

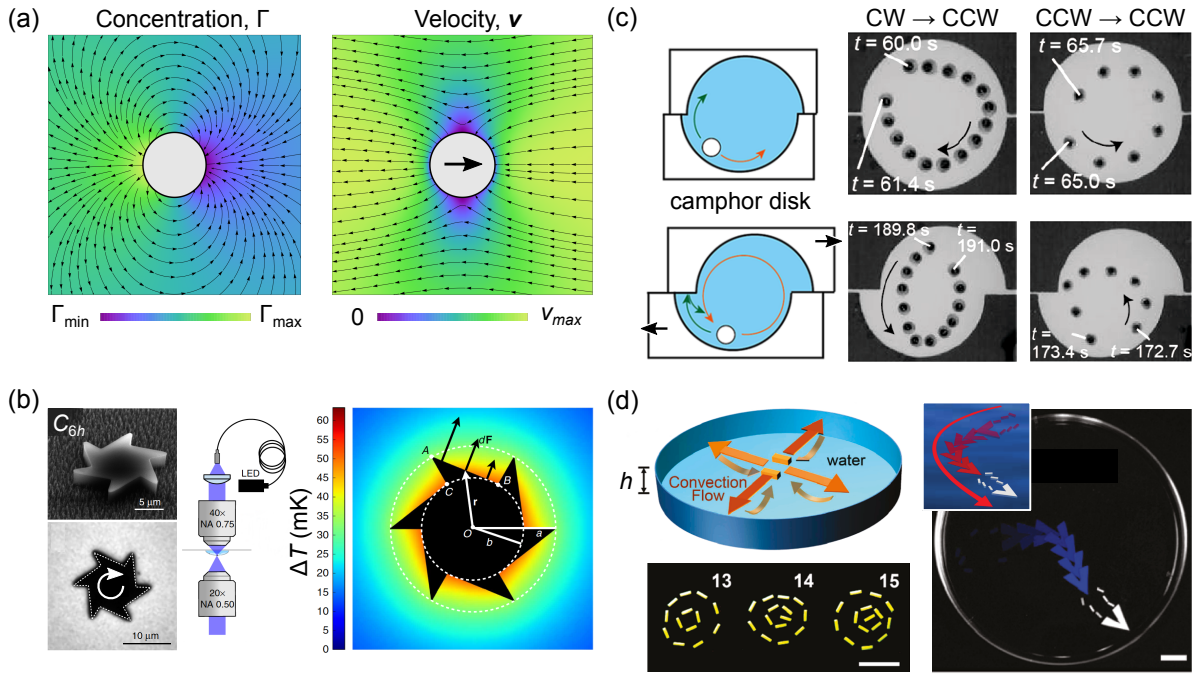

Figure 1.3: (a) Surface concentration and velocity accompanying viscous Marangoni propulsion [5]. (b) Shape-directed rotation of asymmetric microgears due to light-powered thermocapillary flows [6]. (c) Asymmetries in the boundaries of a water-air interface direct the orbital motions of camphor particles in a preferred direction. (Adapted with permission from Ref [7]. Copyright (2017) American Chemical Society.) (d) Dynamic assemblies (left) and motile swarms (right) formed by camphor-loaded gel particles. (Adapted with permission from Ref [8]. Copyright (2017) American Chemical Society.)

$\Delta\Gamma \sim 10^{-8}$ mol/m^2 (1 molecule per 13×13 nm^2) can propel particles at speeds of $U \sim 30$ mm/s across the water-air interface.

Importantly, this result assumes that both the Péclet and Reynolds numbers are small – that is, $= Ua/D \ll 1$ and $= \rho Ua/\eta \ll 1$ – such that nonlinearities due to convective flow are absent. This linear regime has been studied theoretically for disks [5], spheres [85], and spheroids [86, 87] propelled by self-generated chemical [5, 86, 87] and thermal [85] gradients. In practice, however, the condition of small Péclet number is rarely satisfied due to the high speeds of Maragoni propulsion (e.g., 500 body lengths per second for 100 μm particles [88]). Continuing the example above, the Péclet number is smaller than unity only for nanoscale particles of radius $a < 40$ nm. Beyond this linear regime, a variety of interesting phenomena emerge such as spontaneous symmetry breaking, oscillatory dynamics, and mode switching among metastable states.

1.4.2 Spontaneous Symmetry Breaking

In the linear regime ($\ll 1$ and $\ll 1$), Marangoni surfing requires asymmetries in the particle shape or surface chemistry to induce steady particle motions. In experiments, however, even symmetric particles such as circular gel disks loaded with camphor exhibit rapid translational and rotational motions when placed onto a water-air interface [89]. Such particle motions are caused by a convective instability that results in the spontaneous breaking of the initial axial symmetry. As the particle moves, it leaves a wake enriched with surfactant, which lowers the surface tension at the trailing edge. The particle is pulled forward by the higher surface tension at the leading edge thereby maintaining its steady motion. The onset of the instability occurs at some critical Péclet number, below which diffusion stabilizes the axially symmetric surfactant distribution and above which particle motion reinforces the

asymmetric distribution. Despite agreement in this qualitative mechanism [90, 8, 82], its details remain uncertain – for example, the value of the critical Péclet number, the role of fluid inertia, and the effects of surfactant losses due to dissolution, evaporation, or reaction. Notably, the nonlinear response of marangoni surfers can be engineered to achieve oscillatory particle motions ("programmed dancing") by tuning the rate at which surfactant is released [83].

Marangoni surfing of solid particles at liquid interfaces is closely related to the propulsion of liquid droplets via self-generated Marangoni flows [21]. Such swimming droplets also exhibit spontaneous symmetry breaking at high Péclet numbers that enables their steady motion [91]. Interestingly, the speed of fluid droplets propelled by Marangoni stresses is often orders of magnitude greater than that of solid particles moving by interfacial phoretic effects [92]. Marangoni surfing at liquid interfaces offers an effective strategy for propelling solid particles at equally fast speeds.

1.4.3 Shaped-Directed Motions

The direction of particle translation and/or rotation depends on the symmetry of the surfers [90, 93, 94, 8, 95, 6]. In one pioneering contribution, the shape of camphor particles was shown direct their spontaneous motion at the water-air interface [90]. In particular, U-shaped particles (C_{2v} point group) translated towards their convex side owing to the asymmetric release of camphor onto the interface. Similarly, comma-shaped particles (C_s point group) performed circular orbits in a preferred direction as specified by the chiral sense of the particle. More recently, micron-scale gears (C_{6h} point group) heated by visible light were found to rotate steadily due to thermocapillary torques induced by particle shape [6] (Fig. 1.3b). Such linear, circular, and rotational trajectories cover all the motions permitted

by symmetry for a steady surfer in a homogeneous 2D environment.

Physically, particle shape can influence Marangoni surfing in several ways. First, it acts to influence the distribution of surfactant (or temperature) along the three-phase contact line. The net force and torque on the particle due to the associated surface tension variations are determined by integrals over this boundary (Fig. 1.3b). Shape also influences the hydrodynamic flows due to particle motion and to Marangoni convection. The combination or competition of these shape effects are often difficult to anticipate. For example, an ellipsoidal particle experiences less viscous drag when it translates parallel to its long axis [66]. In experiment, however, ellipsoid-shaped particles of camphor are observed to surf perpendicular to their long axis as explained by a model that accounts for the shape-dependent transport of camphor onto the liquid interface [95]. Understanding the role of particle symmetry and shape on the motion of Marangoni surfers represents an interesting topic for further study.

1.4.4 Navigating Structured Environments

In 'deep waters', Marangoni surfers move at a constant speed independent of the water depth [96]. When, however, the depth is commensurate with the particle thickness, Marangoni surfers can actually reverse direction and swim toward regions of *lower* surface tension [8, 87]. This counter-intuitive behavior was observed for V-shaped camphor boats, which swam towards the apex in deep water but reversed direction in shallow water [8]. Hydrodynamic models in the low Pélcet number regime offer insights into the mechanisms underlying such reverse Marangoni surfing [87]. In shallow waters, the viscous force due to recirculating Marangoni flows can exceed that due to surface tension asymmetries, thereby reversing the swimming direction.

Marangoni surfers also interact strongly with the boundaries of the interface on which they move. Interactions between a surfer and a solid wall are typically repulsive due to the effects of the boundary on the surfactant distribution and the resulting hydrodynamic flows [97, 89, 85]. Qualitatively, the presence of an impermeable wall causes the accumulation of surfactant in the region separating the wall and the particle; the particle is then pulled away from this low surface tension region. Due to such repulsive interactions, a camphor disk moving in long trough performs regular oscillations like a swimmer doing laps [97]. Moreover, the symmetry and shape of the domain boundaries can be used to direct the motion of Marangoni surfers [7]. When confined to a circular domain, a camphor disk performs circular orbits in either direction. By breaking the symmetry of the boundary (C_{2h} point group), the same surfer can be biased to move only in the counterclockwise direction [7] (Fig. 1.3c).

In addition to their interactions with solid boundaries, surface active colloids also exhibit interactions with the interface itself. Prior to adsorbing at the fluid-fluid interface, the chemical (or thermal) field induced by an active particle can modify the interfacial tension to induce Marangoni flows, which advect the particle to or from the interface [98]. When the particle acts to lower the surface tension (e.g., by generating surface active species or heat), fluid at the interface flows away from the particle thereby drawing it closer to the surface and further reinforcing the Marangoni flows. This interesting theoretical prediction has yet to be demonstrated in experiment.

1.4.5 Assemblies and Swarms

When many Marangoni surfers move on an interface, they interact with one another both through chemical and hydrodynamic "communication". At low number density, collections

of camphor-loaded gel disks move autonomously at the water-air interface with occasional collisions mediated by the repulsive interactions discussed above [89]. Beyond a critical density, however, the disks transition to an ordered hexagonal arrangement, in which convective flows distribute camphor across the interface to inhibit the symmetry-breaking motions of the individual particles. In shallow water, Marangoni surfers can form similar dynamic assemblies even at low number density [8]. As noted above, particle motion in shallow water is determined by competing forces due to surface tension and to Marangoni flows, which can lead to attractive interactions among neighboring particles. Rectangular surfers were observed to organize spontaneously into ordered assemblies with characteristic particle spacings and orientations determined by recirculating Marangoni flows [8] (Fig. 1.3d). Recent theoretical studies suggest that similar assemblies are possible in deep water provided that particles act to *increase* the surface tension [99]. These interesting behaviors might be realized in experiment by engineering particles that consume rather than emit surface active species.

In addition to stationary assemblies, collections of Marangoni surfers in shallow waters can organize to form asymmetric configurations that move autonomously across the interface [8]. When a larger V-shaped surfer is mixed with many smaller rectangular surfers, the smaller "followers" position themselves behind the moving V-shaped "leader" like ducklings trailing mama duck [8] (Fig. 1.3d). These swarms of camphor emitting particles move collectively in response to gradients in the water depth or the temperature. Notably, surfer assemblies swim toward more shallow regions thereby reinforcing the influence of recirculating Marangoni flows essential to their formation [8]. Particles and their assemblies can also be guided by external chemical cues that modify or induce surface tension gradients and the associated Marangoni flows (e.g., to navigate complex mazes [100, 101]).

1.5 Active Capillary Interactions: Dynamic Colloidal Assemblies

Colloidal particles at fluid-fluid interfaces induce local disturbances in the height of the interface that increase its area and thereby its energy. When two or more such disturbances overlap one another, they interfere so as to increase or decrease the interfacial area, raising or lowering the surface energy. These capillary interactions can be modulated in time using external fields or shape-changing particles to direct particle motions or guide particle assemblies. Such active capillary interactions are notable for their long range and their rich physics – particularly on curved interfaces and for large disturbances. In this section, we briefly review some basic concepts of capillary interactions and discuss how they can be tuned using external fields. We highlight several experimental studies in which capillary interactions are used to propel particles and their assemblies through meniscus climbing or magnetocapillary swimming.

1.5.1 Capillary Interactions

Capillary interactions have been the subject of considerable theoretical and experimental study [102, 103, 104, 50]. For small deformations of an otherwise planar interface, the Young-Laplace equation governing the interface height is well approximated by the Laplace equation, and there is a close analogy between capillary hydrostatics and electrostatics in two dimensions. Under these conditions, the disturbance due to a single particle can be expressed in a multipole expansion, which is often truncated after only few terms. The leading order contribution – the monopole – arises when there is a net force acting on the particle normal to the interface (e.g., due to gravity [105, 106]). The next contribution – the dipole – arises when there is a net torque acting on the particle (Fig. 1.4a). For colloidal

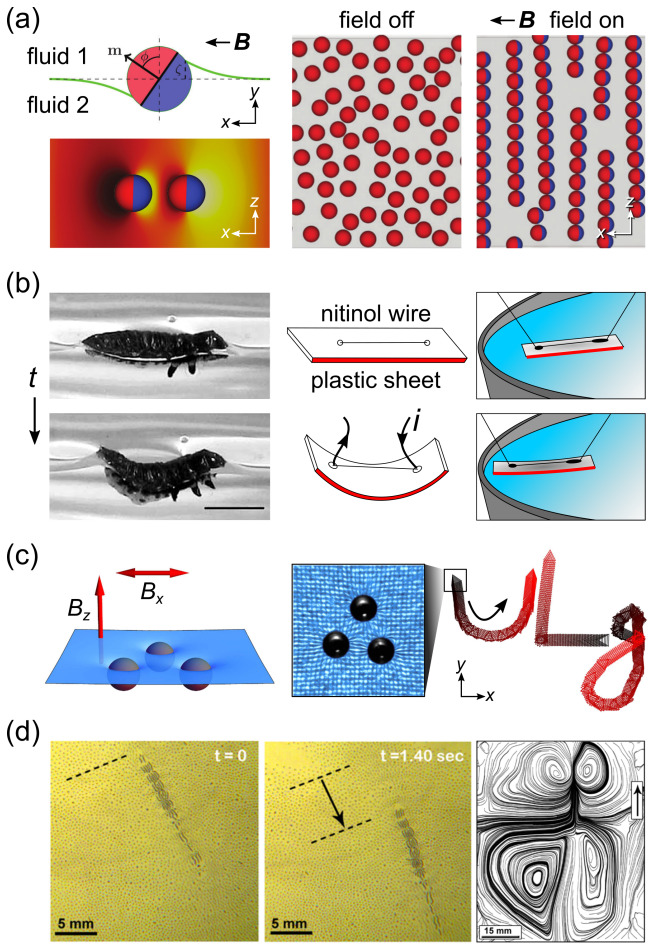

Figure 1.4: (a) A magnet Janus particle at a fluid-fluid interface rotates in an external field to create a capillary disturbance (left) [9]; the resulting capillary interactions guide the assembly of particle chains (right) [10]. (b) The beetle larva *Pyrrhalta* bends to create a quadupolar disturbance (left) [11] (Modified with permission from the Annual Review of Fluid Mechanics, Volume 38 ©2006 by Annual Reviews, http://www.annualreviews.org); an engineered meniscus climber deforms itself and moves to the edge of the petri dish (right) [12]. (c) Magnetic spheres floating at a liquid interface are driven by external fields to perform nonreciprocal motions that propel the clusters along programmable trajectories [13]. (d) Magnetic spheres activated by a oscillating magnetic field excite local capillary waves to form dynamic snake-like assemblies that propel themselves via asymmetric flows. (Adapted with permission from Ref. [14]. Copyrighted by the American Physical Society.)

particles at liquid interfaces, there are often no significant forces or torques, in which case the leading order contribution is that of a capillary quadrupole. Such quadrupolar disturbances arise naturally for particles of anisotropic shape [104, 107] but are also observed for spherical particles due to deviations from the ideal circular contact line (e.g., due to surface roughness [102] or irregular Janus boundaries [108, 109]). These disturbances give rise to long ranged interactions that can lead to aggregation or assembly of particles at interfaces.

At curved interfaces, the interfacial topography can serve as an external field by which to orient and position colloidal particles [110, 111, 112]. Such particles experience capillary forces and torques that act to minimize the excess area contributed by the particle-induced deformations. Particles characterized by quadrupolar disturbances quickly align their principal axes with those of the interface and subsequently move toward regions of high deviatoric curvature[1] [112]. In this way, rod-shaped particles are attracted to the meniscus surrounding a cylindrical post [112]. Curved interfaces can also induce capillary interactions among otherwise non-interacting particles, thereby directing their assembly [113]. By modulating the type and/or magnitude of capillary disturbance surrounding a particle, it becomes possible both to navigate curved interfaces and to propel dynamic particle assemblies. We first consider the different strategies proposed to control capillary interactions using external fields.

1.5.2 Field-responsive Capillary Interactions

A recent series of simulation studies have begun to explore how external fields might be used to induce or modify the capillary disturbances of particles at fluid interfaces. Magnetic fields applied to ellipsoidal particles [114] or amphiphilic Janus spheres [9] with permanent

[1]The deviatoric curvature refers to the difference between the two principal curvatures of the interface.

magnetic moments act to rotate the particles away from their initial orientations (Fig. 1.4a). Ultimately, the particles adopt a new equilibrium orientation, in which the magnetic torques are balanced by capillary torques accompanying the formation of dipolar disturbances in the interface. Shear flows directed parallel to a fluid-fluid interface can also rotate Janus particles to create similar capillary disturbances [115]. For weak fields, the magnitude of the disturbance (i.e., the height of the deformed interface) scales as $\Delta h \sim \tau/\gamma a$, where τ is the applied torque and a is the particle size [9]. For context, a common type of magnetic Janus particle [116] ($a = 1$ μm, $m = 10^{-14}$ A m^2) positioned at an oil-water interface ($\gamma = 50$ mN/m) and subject to a field strength of $B = 10$ mT should deform the interface by only $\Delta h \sim 1$ nm. Realizing these effects in experiment will likely require the use of larger particles with stronger magnetic moments.

Field-induced capillary dipoles can lead to long-range capillary interactions among particles that can be tuned by the external field [117, 10, 118]. Such interactions can guide the formation of particle assemblies, in which particles align into ordered chains (Fig. 1.4a). Depending on the orientation of the field (parallel [10] or perpendicular [117] to the interface), these chains can align in a common direction or meander within disordered networks. Within the chains, the particles' capillary dipoles prefer to align side-to-side as opposed to head-to-tail as expected by analogy to electrostatic dipoles. This discrepancy is caused by the failure of the small slope approximation to accurately describe large deformations or small particle separations [50]. One must therefore return to the full Young-Laplace equation, which is often solved numerically using the lattice-Boltzmann method [117, 10, 118]. Interestingly, chain formation is only observed for sufficiently large fields and high particle densities, despite the absence of Brownian motion or other forces opposing assembly. This observation suggests that particles are easily trapped in local energy minima, which might

be avoided by modulating the field. The effect of interface curvature on such field-induced assemblies is also an interesting direction for future study.

1.5.3 Meniscus Climbing

The ability to modulate capillary disturbances provides a means by which to move particles along curved interfaces. This strategy is inspired by biological organisms such as the beetle larva *Pyrrhalta* that change shape to create quadrupolar disturbances, which enable them to "climb" the meniscus and escape from the interface [11] (Fig. 1.4b, left). Similar meniscus climbing of an engineered "particle" was demonstrated using a rectangular plastic sheet actuated by a thermally-responsive nitinol wire [12] (Fig. 1.4b, right). Ohmic heating of the wire caused the sheet to bend, inducing capillary interactions that propelled it quickly to the boundary of the petri dish. In principle, an particle capable of dynamic deformations could also repel itself from regions of high deviatoric curvature. Such a particle could navigate structured interfaces at high speeds (ca. cm/s) by controlling its local capillary disturbance. If this idea sounds far fetched, consider the recent report of an interfacial robot that serves as a programmable source of fluid curvature to collect passive cargo [119].

In addition to particles that modulate capillary disturbances, there are also tunable interfaces, in which the curvature of the interface is varied dynamically to modify the capillary forces and torques acting on passive particles. One approach uses electrowetting on a dielectric (EWOD) to modulate the height of the meniscus at a the interface boundary [120]. Using a traveling wave of meniscus actuation, one can transport macroscopic objects (capillary monopoles) by way of time-varying capillary interactions [120]. Another strategy relies on arrays of independently addressable bubbles positioned beneath a water-air interface [121]. The bubbles are inflated and deflated to modulate the interface topography

and thereby direct the motion of passive particles. The exploration and application of dynamic (time varying) capillary interactions among field responsive particles or on tunable interfaces remains an exciting direction for further study.

1.5.4 Magnetocapillary Swimming

Capillary interactions are not inherently *active*: they arise even among passive particles at thermodynamic equilibrium. However, when such interactions are modulated in time, they provide means by which to channel external energy inputs into steady dissipative motions of particles and their assemblies. In this way, spatially uniform but time-varying magnetic fields can be used to power magnetocapillary swimmers along fluid fluid interfaces [23, 122]. Such swimmers are typically assembled from ferromagnetic spheres (ca. 100 μm in diameter) held by surface tension at a horizontal interface. Two fundamentally distinct mechanisms for self-propulsion have been explored: one based on low frequency ($f = 1$ Hz), low Reynolds number swimming of small clusters [123, 13, 122] (Fig. 1.4c); another on high frequency ($f = 100$ Hz), finite Reynolds number swimming of structure-induced surface waves [124, 14, 23] (Fig. 1.4d).

The first mechanism uses attractive capillary interactions combined with repulsive magnetic interactions to assemble stable particle clusters at liquid interfaces [125] (Fig. 1.4c). Application of a magnetic field parallel to the interface induces additional dipolar interactions among the particles that perturb the assembly. By modulating this component of the field, the assemblies execute periodic motions under the influence of magnetic, capillary, and hydrodynamic interactions. Importantly, particle motions within clusters of three or more spheres are nonreciprocal – that is, they lack time reversal symmetry. Consequently, the low Reynolds number flows induced by particle motions allow for the directed translation

of the dynamic clusters [123]. The swimming direction depends on the orientation of the applied magnetic field, which is easily rotated within the plane of the interface. In this way, it is possible to direct magnetocapillary swimmers along trajectories of arbitrary complexity at speeds of order af (ca. 100 μm/s in experiment) [13] (Fig. 1.4c).

At higher driving frequencies, the periodic motions the magnetic particles can excite capillary waves that further guide the formation of dynamic snake-like assemblies [124] (Fig. 1.4d). The "snakes" that emerge contain multiple segments, each comprised of many particle chains held together by magnetic dipole-dipole interactions. The field-induced rotation of these particle chains couple to standing capillary waves along the length of the snake. Importantly, these wave-particle structures generate large-scale flows characterized by a pair of counter-rotating vortices at each end of the snake (Fig. 1.4d, right) [126]. Breaking of the fore-aft symmetry, which occurs spontaneously or by addition of a larger "head" particle, results in asymmetric vortex flows that propel the steady swimming motions [14] (Fig. 1.4d, left).

1.6 Conclusions & Outlook

The examples covered in this Review highlight some of the fascinating phenomena that emerge when active particles move and interact at fluid-fluid interfaces. This emerging area is rich with fundamental questions to explore and unique characteristics to apply. It can and should be pursued by researchers from all fronts – in particular, those interested in active colloids and in (passive) particles at interfaces. We hope that this Review can help to further stimulate interest in this growing field. In this spirit, we close by offering a selection of fundamental and applied topics for future study that we find particularly interesting – namely, the study of active matter within curved 2D environments, the application of

Marangoni surfers to enhance mass tranport, and the development of dynamically tunable biphasic materials.

Interfacial curvature has the potential to steer the motion of active particles and guide their collective behaviors; however, our understanding of curvature effects in active matter remain limited. Indeed, the influence of curvature on the assembly of passive particles at fluid interfaces was explored only recently [127]. Similar systems of active colloids at fluid interfaces can provide useful experimental models for the study of active matter. Consider the motion of a Marangoni surfer on a non-planar interface (Fig. 1.5a). How does the curvature and topology of the interface influence its motion? In addition to passive capillary forces, local interface curvature can influence the chemical and hydrodynamic fields surrounding the particle and thereby its motion. Additionally, motion along closed interfaces such as spheres allows for a surfer to interact with its own wake of surface active species. As such particles are typically pulled toward regions of higher surface tension, surfers are expected to avoid their own wake, resulting in complex self-avoiding trajectories.

Fluid flows accompanying the motion of active colloids can serve to accelerate the rates of mass transfer with potential implications for biphasic catalysis and the degradation of interfacial contaminants. For non-motile catalytic particles, the reaction rate is often limited by the diffusive transport of reactants or products to or from the surface of the particle. Particle activity can function to alleviate such transport limitations by introducing convective flows at the level of individual particles. Significant enhancements in the rates of mass transfer require large Péclet numbers ($\gg 1$) [128], which is difficult to achieve using common propulsion mechanisms (e.g., self-phoresis). By contrast, Marangoni surfers readily achieve Péclet numbers of ca. 1000 [88], making them ideal candidates for certain applications. In the context of heterogeneous catalysis at liquid interfaces, active catalytic particles moving

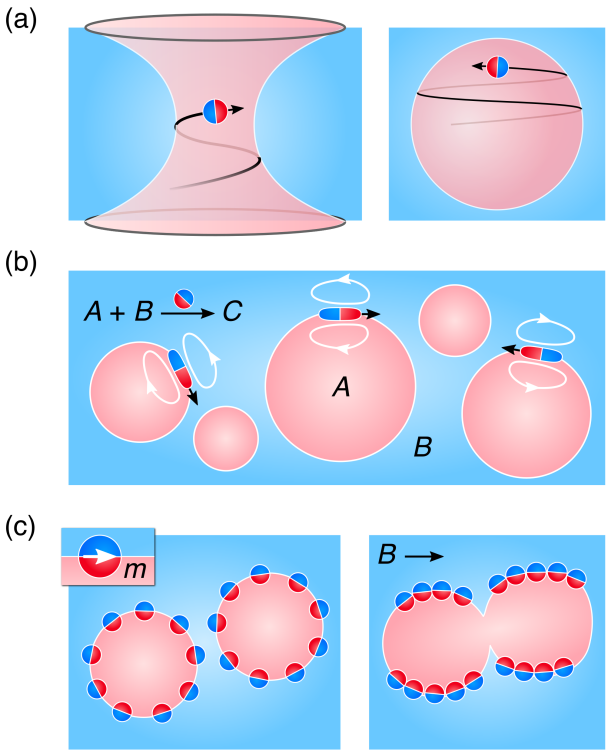

Figure 1.5: (a) Marangoni surfing on curved interfaces. (b) Enhancing mass transfer for biphasic catalysis. (c) Tuning emulsion morphology using external fields.

on the interface can serve to accelerate the reaction by increasing the rate of transport to/from the interface (Fig. 1.5b). Even when active particles are not themselves catalytic, the flows they create can serve to mix fluids at small scales (e.g., that of emulsion drops). The use of active particles at fluid interfaces also benefits from their 2D environment and the tendency for certain chemicals to accumulate therein. In the context of water remediation, the accumulation of organic contaminants at the interface can facilitate their degradation or removal by active particles moving within that environment. In contrast to analogous strategies based on non-motile catalysts or sorbents, active particles have the potential to concentrate in contaminant-rich regions through chemotatic responses that enhance their effectiveness [32].

Particle activity based on external fields provides a basis for responsive emulsions and foams, for which the stability, drop size, and morphology can be tuned dynamically [129, 130]. Emulsions [131, 132, 133] and foams [134, 135] stabilized by magnetic particles can be broken on-demand by the application of magnetic field (gradients) that physically remove particles from the fluid-fluid interface. Looking forward, active capillary interactions have the potential to enable even greater control over emulsion stability and morphology. Figure 1.5c shows one possible example whereby a uniform magnetic field guides the accumulation of magnetic particles at certain regions of an emulsion drop. The directed coalescence of such drops along a certain preferred directions could lead to interesting emulsion morphologies determined by the magnetic stimulus. Another possible challenge in this area is active emulsification, whereby particle activity induces the spontaneous formation of particle-stabilized emulsion droplets. This process could be facilitated by use of field-responsive Janus particles, for which emulsification is thermodynamically favored [136]. In this way, the external field would serve to assist and direct the kinetics of emulsification to achieve

the desired drop sizes and morphology.

We look forward to seeing these and other explorations of active colloids at fluid interfaces grow and develop in the near future.

1.7 Acknowledgements

This work was supported as part of the Center for Bio-Inspired Energy Science, an Energy Frontier Research Center funded by the U.S. Department of Energy, Office of Science, Basic Energy Sciences under Award DE-SC0000989.

Chapter 2

Fabrication and actuation of magnetic Janus particles

2.1 Magnetism Overview

Magnetic materials are divided into paramagnets, diamagnets, and ferromagnets according to their magnetic property. The magnetic moment of paramagnets and diamagnet is linear with an applied magnetic field [137]:

$$\boldsymbol{m} = \frac{V}{\mu_0}\chi \boldsymbol{B} \tag{2.1}$$

where χ is the (volumetric) dimensionless magnetic susceptibility, $\boldsymbol{m}$ is the magnetic moment and $\boldsymbol{B}$ is the magnetic field, V is the material volume, and μ_0 is the magnetic permeability of vacuum. Diamagnetic materials (χ <0) develops a magnetic moment antiparallel to $\boldsymbol{B}$. In a field gradient, it experiences a force toward field minima and repels from the strong field. Many materials are weak diamagnetic, such as water, proteins, DNA, cells, wood, glass [138] and Nylon fibers [139]. Paramagnetic materials (χ <0) develops a magnetic moment parallel to $\boldsymbol{B}$ and experience a force towards higher field strength in the field gradient. Materials that are paramagnetic includes manganese(II) salts, oxygen, and

platinum. A diamagnetic or paramagnetic object can have susceptibility difference χ between the main axis due to shape anisotropy [137]. When a rod-like object is placed in a uniform field, it develops highest magnetic susceptibility along its longest axis and rotates such that its longest axis aligns with the field. Ferromagnetic materials have memory to the external magnetic field, that is, they retain their magnetic moments after the field has been removed. Common ferromagnetic materials include iron, nickel, and cobalt. Ferromagnetic samples are composed of small regions called magnetic domains [140]. Before magnetization, the domains are randomly orientated, leading to a zero net magnetization. When a magnetic field is applied, the domains tend to orient align with the magnetic field. When the field is removed, the net magnetization does not return to zero [137]. Ferromagnetic particle property varies by size. As its size increase, the material transit through three characteristic states: superparamagnetic state, single-domain ferromagnetic particles, multidomain ferromagnetic particles [141]. If the external magnetic field is sufficiently small, the magnetic moment of a ferromagnetic object is modeled as a constant. Superparamagnetic materials are typically very small sized iron oxides or ferromagnets. Since their sizes are so small, thermal energy is able to tune over the direction of the magnetization. Thus, they have a similar magnetic response to paramagnetic materials, but a much higher susceptibility. They are typically modeled as paramagnetic materials. Due to the strong field response and paramagnetic characteristics, superparamagnetic nanoparticles can be used for cell separation and diagnostics by embedded into surface functionalized polymer beads [142, 143, 144].

2.1.1 Methods to generate magnetic fields

A simple method to produce a magnetic field is to use permanent magnets. Strong field gradient can be achieved with alloys such as samarium cobalt (SmCo) or neodymium iron boron (NdFeB) [138]. However, it is experimentally difficult to change the field direction or strength variability, as it requires motion and re-position of permanent magnets. Electromagnets generate fields in which direction and strength can be rapidly changed without mechanically moving the magnets. Typically, uniform field or field gradients are generated by a set of stacked coils separated with some distance and has a commonly shared axis. Helmholtz coils, which their radius and separation distance is identical, produce uniform fields at the geometrical center when current directions in the two coils are the same. Producing and controlling fields in three dimensions can be achieved using three orthogonal coil pairs.

2.1.2 Proportion of magnetic particles

In the Stocks regime, magnetic particles can be actuated by magnetic force $\boldsymbol{F} = \boldsymbol{m} \cdot \nabla \boldsymbol{B}$ using field gradient. This strategy has been demonstrated for micro-motor steering, micro-rheological studies, and separation. Alternatively, one can use a uniform time-varying field to make particle swim by applying torque $\boldsymbol{L} = \boldsymbol{m} \times \boldsymbol{B}$. Oscillating fields induce reciprocal motion of flexible filaments. Due to drag anisotropy, flexible structures swim in viscous fluids [145, 146, 147, 148]. Rotating magnetic fields induce steady torque on the particle that used for translation by designing particle shape or approximate to a boundary [149, 150].

2.1.3 Characterize particle magnetic property

Superconducting quantum interference device (SQUID) is a sensitive tool for magnetic property characterization. It measures the magnetic moment of the sample by applying a field and monitor the very small changes in magnetic flux [151]. However, it needs the sample in the powder or thin film form and making the characterization of individual particle impossible. Alternatively, one can measure the individual particles property by observing its response to uniform time-varying field. In a typical experiment, particles are first dispersed and settled near a glass substrate with separation distance h. Magnetic field rotating about the axis parallel to the substrate is applied and makes particle to spin. Due to the presence of a solid boundary, particles rotational motion leads to their translation. At low frequencies, the particle rotates synchronously with the field, and the translational velocity increases linearly with driving frequency. A ferromagnetic particle with a static magnetic moment has a critical frequency, above which rotational rate decrease with the driving frequency since the particle cannot follow the field. At critical frequency ω_c, the magnetic torque $\boldsymbol{L_m} = \boldsymbol{mB}\sin\phi_{lag}$ equals to the viscus torque exerted on the particle $\boldsymbol{L_v} = 8\pi\eta a^3 f(a/h)\omega$ and the following expression is obtained:

$$\omega_c = \frac{\boldsymbol{mB}}{8\pi\eta a^3 f(a/h)} \tag{2.2}$$

where $\boldsymbol{B}$ is the applied field and ϕ_{lag} is the phase lag between the magnetic moment and the external field, η is the fluid viscosity, a is the particle radius, ω is the driving frequency, and $f(a/h)$ is a function that describes the hydrodynamic interactions with the wall $f(\frac{a}{h} = (1 - \frac{15}{48}\frac{a^3}{h^3})^{-1}$ to leading order[152]. Thus, one can obtain the particle magnetic moment from the critical frequency. Fluidic flow induced by the driven motion of magnetic particle transports energy through the dispersing medium [153, 154, 155]. Simple

interactions among a large number of active particles can form dynamic collective behaviors. Micro-rollers described previously form fingering instabilities by hydrodynamic interactions. Such instability emergence into motile critters. New dynamic special structures with within one colloidal system can also be produced by hydrodynamic synchronization [156, 157, 116, 142, 67]. With a precessing field, magnetic Janus particles form diverse structures such as 2-d crystals and micro-tubes [156]. Peanut-shaped hematite particles were programmed into liquid, chain, vortex, and ribbon-like microrobotic swarms by oscillating, rotating, and precessing fields. The swarms states can be transformed fast and reversibly, which provides a basis of adaptive, multifunctional micro-robots.

2.2 Fabrication of magnetic Janus particles

Janus particles, similar to the god Janus, have two sides different from each other chemically or optically [158]. Micro-sized Janus particles can be observed by optical microscopy and are useful for active matter studies. Janus particles with one side been fluorescent aids visualizing particle orientation [159, 160, 161, 162]. Janus particle surface chemistry controls its absorbance at a liquid-liquid interface and harnesses interfacial energy for assembly or propulsion. This section reviews two common methods to fabricate Janus particles: phase separation method and surface modification method.

2.2.1 Phase separation method

The phase separation method is to use interacted forces, surface tension, or elastic forces of the polymer interactions to separate polymer blends or magnetic particle grains, and then obtain Janus property [163]. Although it has not been used to produce Janus particles in this thesis (i.e. Chapter 3 and Chapter 4), phase separation method allows one to

mass produce Janus particles that is useful for industrial applications or scaling up. Particle morphology is typically characterized by SEM, TEM, optical microscopy, and confocal laser scanning. One simple example is to use commercially available homopolymer blends to fabricate Janus particles. Utilizing surfactant tunes particle morphology and shape. Okubo et al. demonstrated this method and investigated the phase behavior of hydrophobic and hydrophilic PS/PMMA homopolymer mixtures within micrometer-sized emulsion droplets [164, 165, 166, 166]. These droplets were made by PS and PMMA monopolymers dissolved in toluene and stabilized by surfactants. The droplets were suspended in water. As toluene evaporates, phase separation occurs between PS and PMMA phase and fully isolated. Fine tuning polymer/polymer and polymer/water interfacial tension changes particle shape and structure. For instance, the author found that SDS surfactant makes spherical particles while increasing surfactant concentration changes particle from core-shell structure (with PS being the core) to a Janus structure. Since SDS helps to decrease the differences between the interfacial tensions of PS and PMMA with the water phase and promotes the formation of Janus structure. Ellipsoidal or bowl-shaped particles can be formed by introducing more powerful non-ionic surfactants, which reduces the interfacial tension between water and toluene(polymer) phase. Furthermore, an increase in molecular weight raises the interfacial tension between the two homopolymers during polymerization, and yield Janus type structure. Magnetic Janus particles can be fabricated by dispersion polymerization of homopolymer blends containing magnetic nanoparticles. Nanoparticles are concentrated in polymer emulsion droplet [167] by sedimentation or external field gradient [168]. Hu and Gao [167] made mini-emulsion droplets chloroform with an excess amount of PVA as stabilizer in water. Both organo-soluble magnetic nanoparticles and low molecular weight PA-bpoly(allyl alcohol) block copolymer dispersed in chloroform phase. As chloroform

evaporates, magnetic nanoparticles precipitate and aggregates to one side of the droplet due to Van der Waals interaction, resulting in magnetic Janus spheres. The concentration of magnetic nanoparticles influences the size of both magnetic compartment and also the Janus particle itself. Nanoparticles in commercially available uncrosslinked paramagnetic polymerbeads (iron oxide nanoparticles embedded in PS particle) can be concentrated to one side of the particle using external field gradient [168] . Particles were first dispersed in PVA solution and cast into a thin film. The film was then solidified after water evaporation and immersed in toluene to liquefy polymer. A strong cubic NdFeB rare earth magnet was used make nanoparticle accumulated at one side of the polymer particle. The particles are then solidified and washed in water. The asymmetric location of magnetic nanoparticles inside polymer beads was confirmed using TEM and particle dynamics under a rotating magnetic field. Last but not least, the magnetic compartment can be embedded in the polymer particle using seeded polymerization reaction [169]. First, an oil-in-water emulsion is synthesized via polycondensation reaction between metastable water-soluble silanols to produce insoluble silsesquioxane, which phase separate nucleating monodisperse droplets. Magnetic cubes suspended in water phase acts as a nucleation site for the formation of oil droplets and is trapped at the interface by interfacial tension. Last, a radical polymerization hardens the oil phase and creates magnetic patchy particles. Resulting particles are monodispersed (polydispersity <5%) and their sizes can be controlled accurately due to this nucleation and growth mechanism.

2.2.2 Surface modification method

Janus particles can be made from bare particles using chemical surface modification or metal deposition. Before modification, part of the raw particle is hidden from modification site by

curved or planar templates. Janus balance can be readily tuned by template particle interaction. Depending on the modification technique and chemicals involved, bare particles can be metallic or non-metallic (silica or polymer). Pickering emulsion can be used as a template to chemically modifying particles. Granick et al. reported a method to fabricate amphiphilic Janus particles by first making wax-in-water Pickering emulsion with silica particle adsorbed at the interface [170]. Emulsion droplets were then transferred to methanol solution containing charged (aminopropyl)triethoxysilane. After that, functionalized silica particles are released form wax surface by dissolving the wax in chloroform. The other unmodified side of silica particle is allowed to react with hydrophobic n-octadecanetrichlorosilane. This method can produce a large quantity of amphiphilic Janus particles and their Janus balance can be tuned by adding molecular surfactants in wax-in-water emulsion [171]. Janus balance is determined by characterizing three-phase contact angles of the particle at the interface by SEM. Glass slides or silicon wafers can be used as planar substrates. Particles are typically for monolayers by spin coating [172] or syringe pump assisted deposition [173]. Particle surface facing away from the substrate can be modified by microcontact printing [174, 175] , or metal deposition [176, 177, 178, 179, 172, 173, 180, 181, 182, 160, 183]. Alternatively, part of the particles can be embedded in a sacrifice layer such as PDMS after forming monolayers on planar substrate. The exposed portion is then modified by direct immersion into solution containing silane [184] or nanoparticle suspension [185, 186, 187]. Janus particles in this thesis (i.e. Chapter 3 and Chapter 4) is produced by evaporating metal on sub-monolayers of polystyrene beads on a planar substrate. The wafer containing sub-monolayers of bare particles are loaded into a vacuum chamber of an evaporator. Metal is then deposited and the thickness is monitored using a crystal thickness monitor. Sometimes it is necessary to first deposit Cr or Ti as an adhesive layer before evaporation of other metal [156, 109]. After

that, magnetic materials, such as Ni and iron oxides [185, 173, 156, 109] can be evaporated to render the particle magnetic. For metals with high melting temperatures (such as Pt), one shall first deposit an adhesive layer (with Ti or Cr) on polymer particles or use silica particle to prevent particle deformation. To enable surface functionality, gold can be the last layer deposited on the particle. The gold side of the Janus particle can be rendered hydrophilic or hydrophobic using suitable ligands [109, 172]. Asynchronous magnetic bead rotation (AMBR) method [67, 188] confirms that magnetic Janus particles made by this technique have uniform magnetic property [172].

Chapter 3

Magneto-capillary dynamics at curved liquid interfaces

3.1 Abstract

A homogeneous magnetic field can exert no net force on a colloidal particle. However, by coupling the particle's orientation to its position on a curved interface, even static homogeneous fields can be used to drive rapid particle motions. Here, we demonstrate this effect using magnetic Janus particles with amphiphilic surface chemistry adsorbed at the spherical interface of a water drop in decane. Application of a static homogeneous field drives particle motion to the drop equator where the particle's magnetic moment can align parallel to the field. As explained quantitatively by a simple model, the effective magnetic force on the particle scales linearly with the curvature of the interface. For particles adsorbed on small droplets such as those found in emulsions, these magneto-capillary forces can far exceed those due to magnetic field gradients in both magnitude and range. This mechanism may be useful in creating highly responsive emulsions and foams stabilized by magnetic particles.

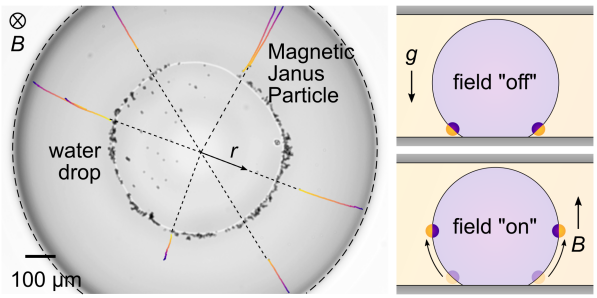

Static homogeneous fields drive motions of magnetic particles along curved liquid interfaces.

3.2 Introduction

The actuation of microscale particles by magnetic fields provides a basis for the development of responsive materials [131, 134, 135], active particle assemblies [116, 67], and colloidal robots [189, 190] with increasing functionality. In contrast to electric and optical fields, magnetic fields are not screened or scattered by common materials and can therefore act remotely, instantaneously, and specifically on magnetic particles introduced for a desired purpose. Such particles are characterized by a magnetic dipole moment $\boldsymbol{m}$, which determines their response to an applied field $\boldsymbol{B}$. Notably, a homogeneous field induces no force on a magnetic particle but rather a torque, $\boldsymbol{L} = \boldsymbol{m} \times \boldsymbol{B}$, that acts to align the moment parallel to the field. The generation of magnetic forces requires spatial gradients in the field, $\boldsymbol{F} = \boldsymbol{m} \cdot \nabla \boldsymbol{B}$, which allow for three-dimensional positioning of magnetic particles [191]. In practice, however, this approach is limited by the complexity of the required fields and by the magnitude of the forces generated. As a result, other strategies for positioning or propelling magnetic particles have been explored using time-varying homogeneous fields [192, 193]. In particular, rotating fields induce steady torques that couple to particle translation in viscous fluids through the design of particle shape[194, 195] or the proximity

of fluid boundaries [2, 67]. The use of hydrodynamics to couple magnetic torque to particle translation suggests that other physics might be used to enable new forms of magnetic positioning in static homogeneous fields.

One approach to coupling the orientation and position of a colloidal particle is to confine its motion along a curved interface. Particles of asymmetric shape [107] or surface chemistry [46] are known to adsorb spontaneously at fluid-fluid interfaces in a preferred orientation that minimizes the interfacial energy. Particle motion along a curved interface is therefore accompanied by particle rotation as to maintain this orientation. By exploiting the coupling between particle position and orientation, it should be possible to translate applied torques into particle motions across curved interfaces. In particular, magnetic particles could be driven to move by application of static homogeneous fields [196]. This idea was recently investigated using numerical simulations [197]; however, it has yet to be demonstrated in experimental practice. The use of homogeneous fields to redistribute magnetic particles at liquid interfaces has important implications for the design of field-responsive emulsions [131] and foams [134, 135].

Here, we investigate the motion of magnetic Janus particles (MJPs) [198, 179, 172, 199, 156] along curved decane-water interfaces in response to static homogeneous fields. Owing to their amphiphilic surface chemistry, the MJPs adsorb onto spherical water drops with their magnetic nickel hemisphere positioned in the aqueous phase. Application of the magnetic field causes the particles to move along the drop surface to align their magnetic moments parallel to the field. These motions are captured quantitatively by a simple model that accounts for the magnetic torque on the particle and the constraints imposed by the interface. We show how the particle velocity increases with increasing field strength and with decreasing drop radius R. Notably, the effective magnetic force, $F \sim mB/R$, experienced

by particles adsorbed on small drops can be many orders of magnitude larger than those due to field gradients. This result suggests that asymmetric magnetic particles may be useful for creating highly responsive emulsions and foams with tunable morphology and stability.

3.3 Experiment

Our experiments were based on magnetic Janus particles (MJPs) with amphiphilic surface chemistry (Fig. 4.1a, inset). To prepare the particles, we first deposited successive layers of metal – 5 nm Ti adhesive layer, 25 nm Ni magnetic layer, and 20 Au functionalization layer – onto monolayers of 4 μm fluorescent sulfonated polystyrene (PS) particles by e-beam evaporation [172]. The gold hemispheres of the MJPs were rendered hydrophilic by chemical functionalization with 3-mercaptopropionic acid (MPA) ligands [109]. Such particles were observed to adsorb at the decane-water interface with their MPA-functionalized hemispheres directed toward the aqueous phase in agreement with previous reports (Fig. S1) [109]. Additionally, the nickel layer gave the particles a permanent magnetic moment $m \approx 3 \times 10^{-14}$ A m^2 directed parallel to the Janus equator [116, 200]. The particles' magnetic properties were determined from measurements of particle translation along a solid substrate ("rolling") in a rotating magnetic field as a function of the applied frequency (Fig. 3.5) [67].

MJPs were spread onto the curved interface of a water drop in decane supported between two hydrophobic glass slides (Fig. 4.1a). A drop of water (˜0.5 μL) was first deposited onto a cover slip treated with a hydrophobic silane. Amphiphilic MJPs suspended in a mixture of water and isopropyl alcohol (7:3 ratio) were spread onto the interface using a micropipette. The cover slip was then incorporated as the base of a glass chamber, into which decane was flowed [78]. The chamber was sealed with UV-curable epoxy (NOA 68) and positioned on the stage of an inverted microscope for imaging. The particles settled under gravity to the

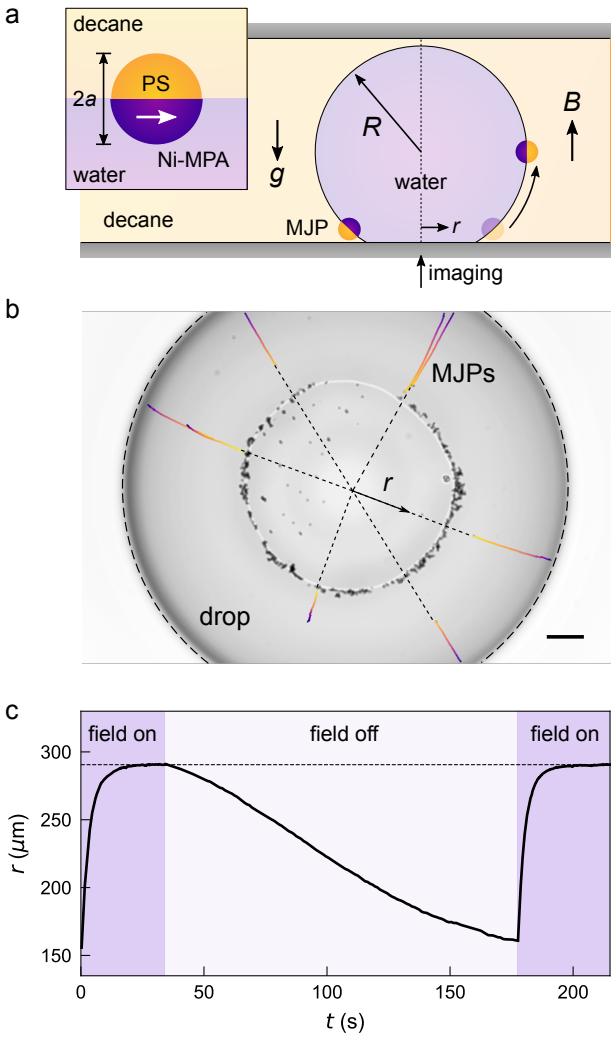

Figure 3.1: (a) Schematic illustration of a magnetic Janus particle (MJP) moving on the curved interface of a water drop in decane due to a homogeneous magnetic field $\boldsymbol{B}$. The inset shows the preferred orientation of the MJP at the interface and its magnetic moment (white arrow). (b) Optical micrograph of the water drop showing the radial trajectories of six different MJPs; scale bar is 100 μm. (c) Projected radial position of an MJP as a function of time for successive applications of the magnetic field. Here, the field strength is $B = 15$ mT, and the drop radius is $R = 291$ μm.

three-phase contact line at the bottom of the drop (Fig. 4.1b).

Application of a magnetic field $\boldsymbol{B}$ antiparallel to the gravity direction caused the particles

to migrate to the drop equator along radial trajectories (Fig. 4.1b). Two electromagnet coils positioned above and below the drop created a spatially uniform field with variations of less than 0.5% within the 0.4 cm^3 region of interest (Fig. 3.6). Upon application of the field, some particles moved radially outward from the axis of symmetry along the interface of the drop. Others remained pinned at the three-phase contact line and did not move (Fig. 4.1b), perhaps due to attractive surface forces with the hydrophobic substrate. Particle motions were captured by fluorescent video microscopy, during which the focal plane was manually adjusted to keep the particle in focus as it moved to the drop equator. Particle trajectories projected onto the imaging plane were reconstructed from the videos using standard particle tracking algorithms (Trackpy v0.3.2). When the field was switched off, the mobile particles slowly settled back toward the three-phase contact line. By cycling the the magnetic field on and off, we captured multiple trajectories of a single particle moving on the interface of single drop (Fig. 4.1c).

3.4 Results and Discussion

The experimental observations are explained by a simple model that accounts for the magnetic torque on the particle and the constraints imposed by its amphiphilic surface chemistry. The magnetic energy of the system is minimal when the particle's magnetic moment $\boldsymbol{m}$ is aligned parallel with the applied field $\boldsymbol{B}$. Similarly, the interfacial energy of the system is minimal when the symmetry axis of the amphiphilic MJP is aligned perpendicular to the interface. For the particles described here, both conditions are satisfied only when the particle is located at the drop equator. At other locations, magnetic and interfacial torques compete with one another to drive rotational and translational particle motions.

The characteristic scale of the magnetic torque mB is much smaller than that of the

interfacial torque γa^2 where γ is the interfacial tension; here, $mB/\gamma a^2 \sim 0.002 \ll 1$. Consequently, the applied field does little to change the preferred orientation of the particle axis relative to the interface [9]; such rotations are effectively prohibited by the particle's amphiphilic surface chemistry. By contrast, the particle is free to rotate about its symmetry axis and to translate across the surface of the drop without changing the interfacial energy. Importantly, the constraints imposed by the interface allow one to translate magnetic torques applied to the particle into translational motions along the drop surface.

The position and orientation of an MJP adsorbed at the interface of a spherical drop can be specified by three angles: the polar angle θ, the azimuthal angle φ, and the orientation angle β that describes the direction of the particle's magnetic moment in the plane of the interface (Fig. 3.2). The angle α between the particle's magnetic moment and the unit vector normal to the interface is assumed to be constant (Fig. 3.2); $\alpha = \pi/2$ in our experiments. In a uniform magnetic field $\boldsymbol{B} = B\boldsymbol{e}_z$, the magnetic energy of a single ferromagnetic particle is $U = -\boldsymbol{m} \cdot \boldsymbol{B}$. By differentiating this expression with respect to each coordinate, we obtain the generalized forces that act to move and rotate the particle on the drop interface. At low Reynolds numbers, these forces are balanced by the viscous drag, resulting in the following overdamped dynamics

$$\dot{\theta} = -\frac{1}{\lambda_t R^2}\frac{\partial U}{\partial \theta} = \frac{mB}{\lambda_t R^2}\left(\sin\alpha\cos\beta\cos\theta + \cos\alpha\sin\theta\right), \tag{3.1}$$

$$\dot{\beta} = -\frac{1}{\lambda_r}\frac{\partial U}{\partial \beta} = -\frac{mB}{\lambda_r}\sin\alpha\sin\beta\sin\theta, \tag{3.2}$$

where $\lambda_t \approx 6\pi\eta a$ and $\lambda_r \approx 8\pi\eta a^3$ are drag coefficients for translation and rotation, respectively, and $\eta = 9.1 \times 10^{-4}$ Pa s is an effective fluid viscosity at the interface. For spherical drops, there is no particle motion in the azimuthal direction since $\partial U/\partial\varphi = 0$.

These dynamics can be solved analytically when the particle is much smaller than the

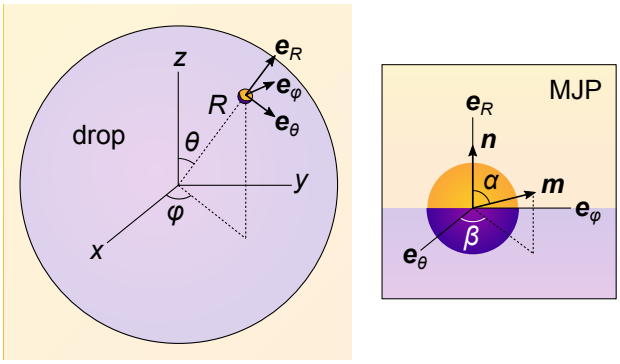

Figure 3.2: The position and orientation of an amphiphilic Janus particle on a spherical drop can be described by the angles θ, φ, and β. The angle α between the particle's permanent magnetic moment $\boldsymbol{m}$ and the unit normal vector $\boldsymbol{n}$ is held constant by interfacial forces.

drop ($a \ll R$). Under these conditions, the orientation angle β relaxes quickly to a stable value of $\beta = \pi$, and the particle moves slowly to its stable position. Integrating Eq. 4.4 with $\alpha = \pi/2$ and $\beta = \pi$, we obtain the following expression for the projected radial position measured in experiment

$$r(t) = R \sin\left\{2 \tan^{-1}\left[\tanh\left(\tfrac{1}{2} k_m t + C\right)\right]\right\}. \tag{3.3}$$

Here, $C > 0$ is a constant that determines the position of the particle at $t = 0$, and $k_m \equiv mB/\lambda_t R^2$ is the characteristic rate for magnetic particle actuation. Physically, the particle moves to the equator of the drop ($r \to R$) to align its magnetic moment with the applied field. This model can be generalized to include the effects of gravity as detailed in section 3.8.

The model predicts that the rate of magnetic actuation should increase with decreasing drop size as $k_m \propto R^{-2}$. To evaluate this prediction, we measured the field-induced particle trajectories on droplets of different sizes (Fig. 3.3a). For each drop, we tracked the motion of a single particle during several cycles of magnetic actuation and sedimentation under

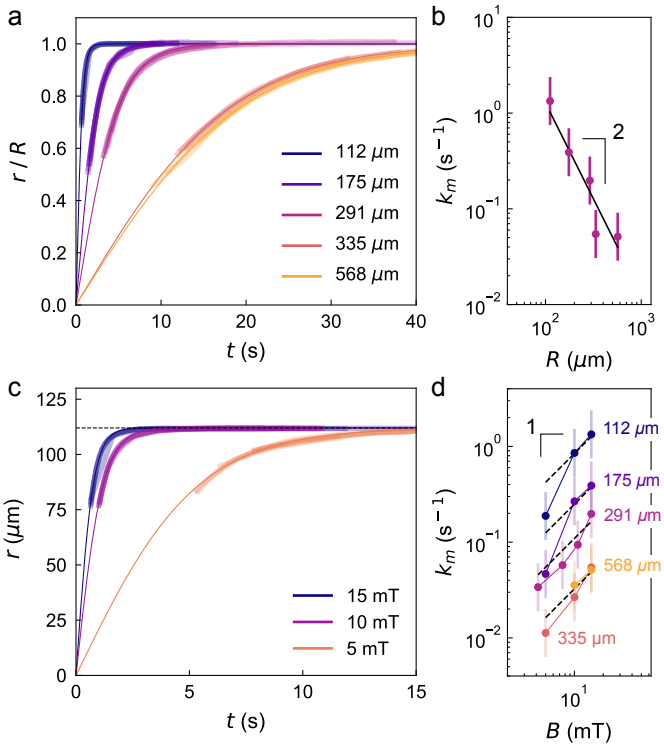

Figure 3.3: (a) Projected radial trajectories of MJPs on drops of different radii for $B = 15$ mT. For each drop, the wide curves show multiple tracks from a single particle superimposed over the model prediction (thin curve). (b) Rate parameter vs. drop radius inferred from the data in (a). (c) Projected radial trajectories of a single MJP moving on a drop of radius $R = 112$ μm at different field strengths. (d) Fitted rate parameter vs. field strength for different drop radii. Error bars denote one standard deviation above and below the mean.

gravity. For each particle, we used Bayesian inference [201] with Markov chain Monte Carlo (MCMC) sampling [202] to estimate the rate parameter k_m from the reconstructed trajectories (see section 3.8 for details). Figure 3.3b shows the inferred rate parameter as a function of the drop radius for a constant field strength of $B = 15$ mT.

The experimental results agree with the model predictions of eq. (3.12) when accounting for the observed variability in the motions of different particles. For each particle, the root-mean-square (rms) error in the rate parameter was small (ca. 0.6% of the mean),

indicating good reproduciblility during successive applications of the field. In the rare cases when multiple mobile particles were present on the same drop, we analyzed each particle separately to assess the variability in the rate parameter from one particle to the next. The motions of different particles subject to identical conditions varied by ca. 60%, perhaps due to differences in their magnetic moments, their orientation at the interface, or their resistance to motion.[74] The error bars in Figure 3.3 represent this larger variability in the motions of different particles. Using the data in Figure 3b, we infer the average magnetic moment of the particles to be $m = 2.9 \times 10^{-14}$ A m^2, which agrees well with independent estimates from our magnetic characterization (Fig. 3.5).

The model also predicts that the rate parameter k_m should increase linearly with the magnitude of the applied field. To test this prediction, we varied the applied field over the experimentally accessible range of $B = 4 - 15$ mT. Larger fields were inaccessible due to significant Joule heating of the electromagnet coils; smaller fields led to weak magnetic forces that struggled to compete with those due to gravity. Figure 3.3b shows the projected radial trajectories for a single MJP adsorbed on a drop of radius $R = 112$ μm for three different field strengths. From these data, we inferred the rate parameter k_m for each field strength assuming the validity of eq. (3.12). The inferred rate increased monotonically with increasing field strength but deviated from the expected linear dependence – particularly at weak fields (Fig. 3.3d).

The failure of the model at weak fields is likely caused by other forces due to gravity, light-induced Marangoni stresses, or gradients in the drop curvature. The predicted dynamics of MJPs moving under the influence of both magnetic and graviational fields is derived in section 3.8. This augmented model is characterized by an additional dimensionless parameter, $G \equiv MgR/mB$, which measures the relative importance of gravitational

and magnetic forces (here, M is the bouyant mass of the particle, and g is the acceleration due to gravity). At low fields, this parameter is $G = 0.2$, and the effects of gravity cannot be neglected. However, even when accounting for gravitational forces, the inferred rate parameter k_m was still considerable smaller than that predicted by theory (Fig. 3.11).

In addition to gravity, spatial variations in the interfacial curvature and tension give rise to other forces that may alter magneto-capillary particle motions. MJPs adsorbed at liquid interfaces are known to induce capillary disturbances that interact with the curvature field imposed by the interface [109, **?**, 112]. Such capillary forces are absent for particles adsorbed at spherical interfaces, which have zero deviatoric curvature (i.e., equal principal curvatures, $c_1 = c_2 = 1/R$). However, it is possible that the drops used here deviate slightly from their ideal spherical shape (e.g., due to gravity or pinning of the three-phase contact line) resulting in nonzero capillary forces. A more likely explanation for the anomalous behavior at low field strengths is motion due to Marangoni stresses caused by light-induced heating of the particles. Particles at liquid interfaces are known to move via self-generated surface tension gradients when heated by irradiation with visible light [6]. Under bright illumination (5.4 mW/mm^2), the field-induced motions of our MJPs were observed to deviate significantly from those at low illumination (0.15 mW/mm^2) detailed above. At low field strengths, magneto-capillary forces may compete with light-powered Marangoni propulsion in directing the motion of MJPs along curved interfaces (Fig. 3.8).

3.5 Conclusions

The constraints imposed by a liquid interface on the motions of magnetic Janus particles enables uniform magnetic fields to induce strong magnetic forces of order $F_m \sim mB/R$. For particles adsorbed on small droplets such as those found in emulsions, these magneto-

capillary forces can far exceed those due to magnetic field gradients in both magnitude and range. This mechanism may therefore be useful in controlling the stability, drop size, and morphology of emulsions and foams stabilized by magnetic particles [131, 134, 40]. For example, the application of a uniform magnetic field could drive the redistribution of MJPs on the surface of emulsion drops, thereby altering their stability to coalescence along specified directions (e.g., at the drop poles). In this context, further work is required to understand the impact of interfacial rheology on field-induced particle motions at complex fluid interfaces [203, 204]. We emphasize that the magneto-capillary forces described here are not limited to magnetic Janus particles, which provide a convenient model system. Similar behaviors are also expected for other anisotropic particles that adsorb at liquid interfaces in a preferred orientation [107] and respond to external magnetic fields (e.g., hematite ellipsoids [205]). Beyond the simple dynamics described here, more complex particle motions are possible using spatially uniform fields with time-varying magnitude and direction.

3.6 Conflict of interest

There are no conflicts to declare.

3.7 Acknowledgements

This work was supported as part of the Center for Bio-Inspired Energy Science, an Energy Frontier Research Center funded by the U.S. Department of Energy, Office of Science, Basic Energy Sciences under Award DE-SC0000989.

3.8 Supporting Informaton

3.8.1 Orientation of MJPs at Planar Interfaces

Magnetic Janus particles adsorb at the oil-water interface in a preferred orientation with their MPA-functionalized metal hemisphere in water and their PS hemisphere in oil. We confirmed the particles' orientation using a combination of bright field and fluorescence imaging of MJPs adsorbed at a planar decane-water interface (Fig. 3.4).

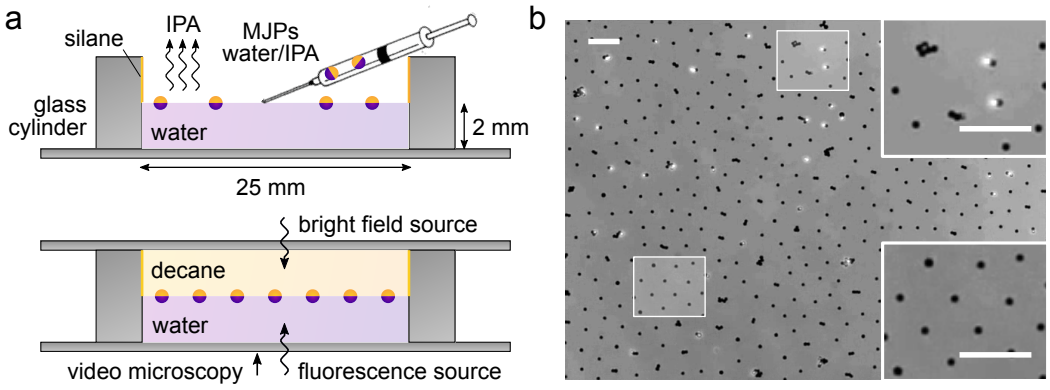

Figure 3.4: (a) Spreading MJPs on a planar decane-water interface. (b) Combined bright field and fluorescence image of MJPs adsorbed at planar decane-water interface; scale bar is 50 μm

The particles were spread onto the decane-water interface following a literature protocol [109] (Fig. 3.4a). First, water was added to a cylindrical glass cell mounted on a microscope slide. The top half of the glass cell was treated with a hydrophobic silane to pin the water-decane contact line along a prescribed circular boundary [206]. The volume of water was varied to achieve a nearly planar interface. MJPs were dispersed in a 7:3 mixture of water and isopropyl alcohol (IPA) and injected onto the water-air interface using a Hamilton syringe. Decane was added, and the cell sealed by a glass cover slip using silicon grease.

The particles were imaged from below by an inverted microscope using a combination

of bright field and fluorescence imaging modes. Figure 3.4b shows a characteristic image of MJPs at the decane-water interface. Particles appear dark when their metal hemispheres are oriented "down" toward the aqueous phase and the microscope objective. Alternatively, particles appear bright when oriented "up" such that their fluorescent core is visible. MJPs and small clusters thereof repel one another through electrostatic dipole-dipole interactions to form stable configurations at the interface. Singlet particles are nearly always oriented with their metal hemisphere "down" in agreement with previous reports [109] (Fig. 3.4b, bottom right). Particle clusters, however, often contain individual particles in other orientations (e.g., the two doublets in Fig. 3.4b, top right). The application of a uniform magnetic field directed normal to the interface ($B = 15$ mT) had no observable effect on the orientation of the adsorbed MJPs; the magnetic torques were much smaller than those due to interfacial forces.

3.8.2 Magnetic Rolling Experiments

To provide an independent estimate of the magnetic moment of the Janus particles, we quantified their translational "rolling" motion above a solid planar substrate due to a rotating magnetic field [67]. As illustrated in Figure 3.5a, a rotating magnetic field in the xz-plane with magnitude B and frequency ω caused the particle to rotate about the y-axis and simultaneously translate in x-direction. Figure 3.5b shows the measured particle velocity V as a function of the applied frequency. The velocity increases linearly with frequency up to some critical value ω^*, above which it begins to decrease.

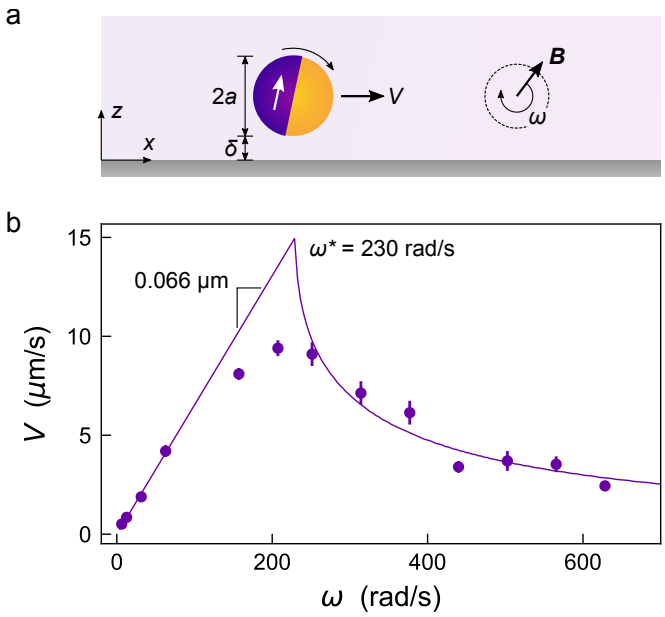

Figure 3.5: (a) A rotating magnetic field $\boldsymbol{B}(t)$ drives the rotation and translation of a magnetic Janus particle along a solid wall. (b) Measured particle velocity V as a function of the applied frequency ω (markers). The particle radius was $a = 2$ μm, and the field strength $B = 1.7$ mT. Error bars denote the standard error of the measured velocity based on about 100 particles. The solid curve shows the predicted velocity of a ideal ferromagnetic sphere with magnetic moment $m = 3.1 \times 10^{-14}$ A m^2.

This observed behavior is captured quantitatively by a model that accounts for the magnetic and viscous torques acting on the particle and for the hydrodynamic coupling between particle rotation and translation near the solid substrate [67]. Below the critical frequency, the particle's magnetic moment rotates in lock step with the applied field such that the angular velocity of the particle is equal to that of the field. At low Reynolds numbers, the resulting particle velocity is given by

$$V = a\omega \frac{Y^B(\xi)}{Y^A(\xi)} \quad \text{for } \omega < \omega^*, \tag{3.4}$$

where Y^A and Y^B are components of the hydrodynamic resistance tensor for a sphere separated from a plane wall by a scaled distance $\xi = \delta/a$ [207, 149]. From the experimental data, the fitted slope of the particle velocity versus applied frequency is 0.066 μm for $a = 2$ μm. Using these values, eq. (3.4) implies that the effective surface separation is $\xi = 0.21$. At the critical frequency, the viscous torque on the particle is equal to the maximum magnetic torque such that

$$6\pi\eta a^3 \omega^* Y^C(\xi) = mB, \tag{3.5}$$

where the coefficient Y^C describes the torque on a sphere rotating about an axis parallel to the surface [208] (here, $Y^C = 1.69$ for the estimated surface separation $\xi = 0.21$). Using the known viscosity ($\eta = 8.90 \times 10^{-4}$ Pa s) and field strength ($B = 1.7$ mT), eq. (3.5) implies that the particle magnetic moment is $m = 3.1 \times 10^{-14}$ A m^2.

3.8.3 Characterization the Uniform Magnetic Field

We designed and built a two-coil electromagnet for manipulating MJPs on the stage of an inverted optical microscope. Each coil was prepared by winding 131 m of copper wire with an insulating coating (24 AWG) around a 3D-printed ABS scaffold with an inner diameter of 3.4 cm, outer diameter of 9.4 cm, and height of 1.2 cm. The wrapped wire had an inner diameter of 3.6 cm, outer diameter of 9.3 cm, and height of 0.8 cm. The two coils were 1.8 cm apart from each other and placed above and below an acrylic sample holder mounted on the microscope stage (Fig. 3.6a). The water drops on which the particles moved were positioned at the center of the two coils. DC currents of 0.25 to 0.9 A were applied to the coils using a sourcemeter unit (Keithely 2410). The resulting magnetic field was measured at different locations using a gaussmeter (AlphaLab Inc. Model GM2). Figures 3.6b and 3.6c show the two components, B_z and B_r, of the axially symmetric magnetic field for an applied current of 0.9 A. Within the 0.4 cm^3 region of interest (Fig. 3.6a, red region), variations in the applied field were ca. 0.5% of the maximum field strength.

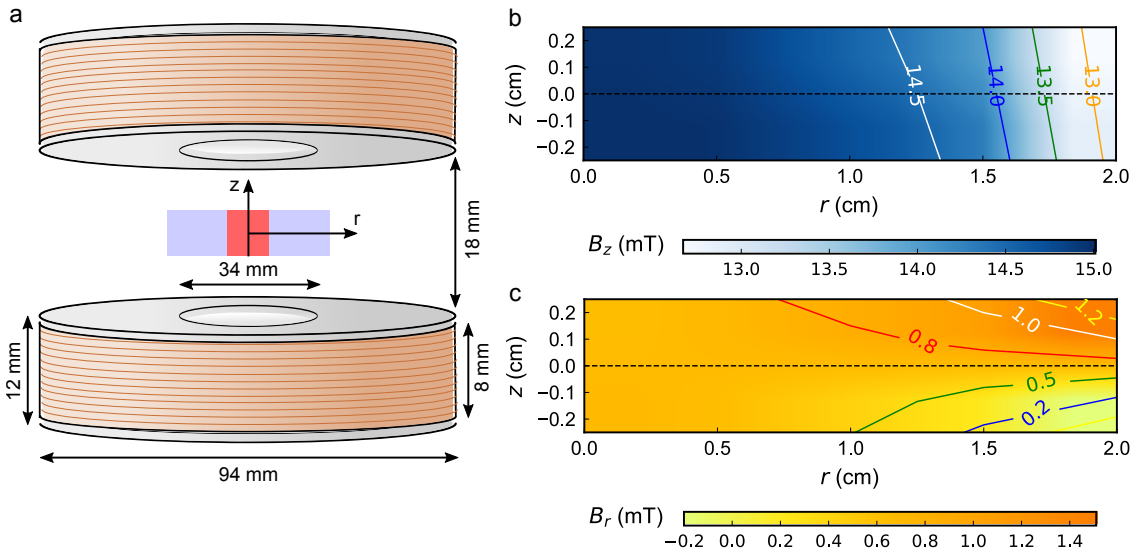

Figure 3.6: (a) Schematic illustration of the electromagnet design. The center of the drop was located at $r = 0$ cm and $x = 0$ cm during each experiment. The measurement region is colored in blue and the region of interest in red. (b,c) Measured components of the magnetic field (b) B_z and (c) B_r as a function of position between the two coils. The component B_r was measured along one direction perpendicular to the z-axis.

3.8.4 Model of Particle Dynamics with Gravity

As in the main text, we consider an amphiphilic Janus sphere of radius a with permanent magnetic moment $\boldsymbol{m}$ adsorbed at the interface of a spherical drop of radius R (Fig. 2). We now consider the effects of a gravitational field pointing in the positive z-direction, parallel to the applied magnetic field $\boldsymbol{B}$.[1] Using a spherical coordinate system centered on drop, the total energy of the particle in these two fields is approximated as

$$U = mB\left(\cos\beta\sin\alpha\sin\theta - \cos\alpha\cos\theta\right) - MgR\cos\theta, \tag{3.6}$$

where m and M are, respectively, the magnetic moment and buoyant mass of the particle, and g is the acceleration due to gravity. From this expression, we derive the generalized forces that act to move and rotate the Janus particle on the drop interface. In the over-damped regime, the resulting particle dynamics are expressed as

$$\dot{\theta} = -\frac{1}{\lambda_t R^2}\frac{\partial U}{\partial\theta} = -\frac{mB}{\lambda_t R^2}(\sin\alpha\cos\beta\cos\theta + \cos\alpha\sin\theta) - \frac{Mg}{\lambda_t R}\sin\theta, \tag{3.7}$$

$$\dot{\beta} = -\frac{1}{\lambda_r}\frac{\partial U}{\partial\beta} = \frac{mB}{\lambda_r}\sin\alpha\sin\beta\sin\theta, \tag{3.8}$$

For small particles ($a \ll R$) with magnetic moments oriented parallel to the interface ($\alpha = \pi/2$), the orientation angle β relaxes quickly to a stable value of $\beta = \pi$. The dynamics of the particle position, characterized by the polar angle θ, can be approximated as

$$\dot{\theta} = k_m\cos\theta - k_g\sin\theta, \tag{3.9}$$

where $k_m \equiv mB/\lambda_t R^2$ and $k_g \equiv Mg/\lambda_t R$ are characteristic rates due to magnetic and gravitational forces, respectively. These dynamics are characterized by a stable particle

[1] It is only for mathematical convenience that the gravitational field is directed in the positive z-direction and not the negative z-direction as in experiment. This choice confines the relevant particle motions to the region $0 < \theta < \pi/2$ (as opposed to $\pi/2 < \theta < \pi$).

position θ_s at which gravitational and magnetic forces are balanced, $\theta_s = \cot^{-1}(k_g/k_m)$. The system approaches this final position with a characteristic rate constant $k = (k_m^2 + k_g^2)^{1/2}$. When the particle starts from the position of lowest gravitational energy ($\theta(0) = 0$), the approximate dynamics of eq. (4.2) can be integrated to obtain

$$\theta(t) = -2\tan^{-1}\left\{G - \sqrt{G^2+1}\tanh\left[\frac{1}{2}kt + \tanh^{-1}\left(\frac{G}{\sqrt{G^2+1}}\right)\right]\right\}, \tag{3.10}$$

where $G \equiv k_g/k_m = MgR/mB$ is a dimensionless parameter characterizing the relative importance of gravitational and magnetic forces. The projected radial position measured experimentally is $r(t) = R\sin\theta(t)$. Figure 3.7 shows the computed dynamics for different gravitational strengths G.

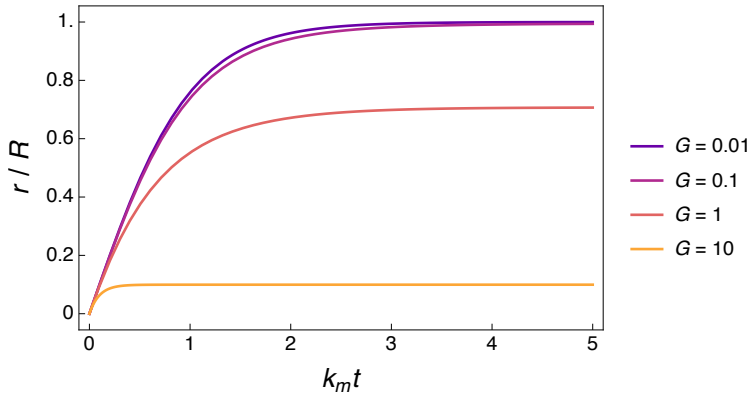

Figure 3.7: Projected radial position as a function of time for different gravitational strengths, $G = MgR/mB$. Initially, the particle is positioned at gravitational energy minimum $\theta(0) = 0$. Here, the radial position is scaled by the drop radius R; time is scaled using the magnetic rate constant $k_m = mB/\lambda_t R^2$.

3.8.5 Data Analysis

3.8.5.1 Parsing Raw Track Data

As discussed in the main text, other forces acting on the MJPs can become significant when the magneto-capillary forces are sufficiently weak. Even at the highest field strengths of $B = 15$ mT, magnetic forces become progressively weaker as the particle approaches its equilibrium position at the drop equator. As a result, particles were often observed to deviate from their expected radial trajectories near the drop equator (Fig. 3.8). Such behaviors are not described by our magneto-capillary model and can interfere with our estimate of the rate parameter k_m. The track data were therefore cropped to exclude these anomalous portions of the particle trajectory.

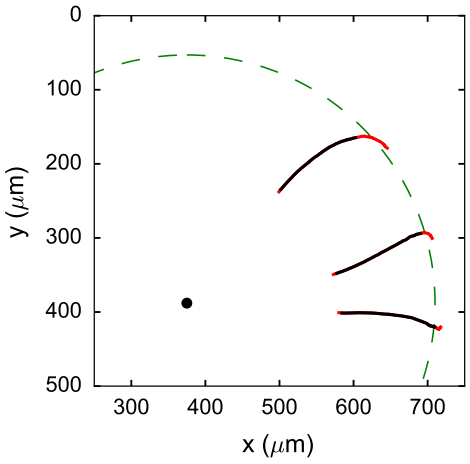

Figure 3.8: Three trajectories of a single MJP projected onto the xy-plane (red). The dashed circle shows the perimeter of the drop centered on the black dot with radius $R = 335$ μm. Only the black portions of the trajectories are used to fit the model parameter.

3.8.5.2 Parameter Estimation of k_m

To estimate the magnetic rate parameter k_m, we use the following model for the projected particle position as a function of time,

$$\begin{aligned} x(t) &= x_o + r(t)\cos\varphi + \varepsilon, \\ y(t) &= y_o + r(t)\sin\varphi + \varepsilon. \end{aligned} \tag{3.11}$$

Here, (x_o, y_o) and φ are, respectively, the origin and the angle the radial trajectory, and ε is a normally distributed random variable with zero mean and standard deviation Δ. The radial position of the particle is given by

$$r(t) = R\sin\left\{2\tan^{-1}\left[\tanh\left(\frac{1}{2}k_m t + C\right)\right]\right\}, \tag{3.12}$$

where R is the drop radius, and $C > 0$ is a positive constant that specifies the radial position at time $t = 0$.

During each experiment, we measure the particle position (x_k, y_k) at successive times t_k following the application of the magnetic field. From these data $\boldsymbol{D}$, we use Bayes theorem to estimate the probability distribution for the unknown parameters $\boldsymbol{X}$ as

$$(\boldsymbol{X} \mid \boldsymbol{D}) \propto (\boldsymbol{D} \mid \boldsymbol{X})(\boldsymbol{X}). \tag{3.13}$$

The posterior distribution, $(\boldsymbol{X} \mid \boldsymbol{D})$, is sampled using Markov Chain Monte Carlo (MCMC) in pyMC3 [202]. The likelihood function, $(\boldsymbol{D} \mid \boldsymbol{X})$, assumes that the observed quantities (x_k, y_k) are independent, normally distributed random variables with unknown standard deviation Δ due to measurement error. The prior probability distribution, $(\boldsymbol{X})$, captures our knowledge of the unknown parameters before analyzing the tracking data.

Specifically, the prior for the rate constant k_m is chosen as a log-normal distribution with parameters $\mu = \ln k'_m$ and $\sigma = 0.5$, where k'_m denotes the theoretical prediction. This

choice implies that the rate parameter is positive and within an order-of-magnitude of the model prediction. The prior for C is also log-normal with $\mu = \ln C'$ and $\sigma = 0.5$, where $C' = 0.27$ such that $r(0) = 0.5R$. The prior for the noise Δ is log-normal with $\mu = \ln \Delta'$ and $\sigma = 0.5$, where $\Delta' = 1$ μm. The drop radius R is measured from an image focused on the drop equator using the Hough circle transformation in ImageJ. This procedure also provides an estimate for the drop center (x_o', y_o'), which differs somewhat from the origin of the radial particle trajectories. The priors for x_o and y_o are normal distributions with standard deviation $\sigma = 30$ μm about the measured drop center (x_o', y_o'). The prior for the angle φ is also normal with standard deviation $\sigma = \pi/4$.

For each drop, particle, and field strength, we obtained several particle trajectories (typically, 3 to 9). The rate parameter k_m, drop center (x_o, y_o), and noise Δ were assumed to be common to all of these trajectories; however, the constant C and the angle ϕ were allowed to vary one trajectory to the next (see Fig. 3.8). The parameters were sampled from the distribution (3.13) using 2000 iterations of the No-U-Turn Sampler (NUTS) implemented in pyMC3. The mean values of the sampled parameters were used to collapse the data shown in Figures 3a and 3c; the markers in Figures 3b and 3d represent mean values of the sampled rate parameter.

3.8.5.3 Sedimentation

To assess the effects of gravity on the motion of MJPs, we first consider the sedimentation of the particles along the drop interface in the absence of the magnetic field. Following the approach of section 3.8.4, the position of a particle on the drop surface will evolve under gravity as

$$\dot{\theta} = -k_g \sin\theta, \tag{3.14}$$

where $k_g = Mg/\lambda_t R$ is the gravitational rate parameter. Note that this expression assumes that the gravitational energy minimum occurs at $\theta = 0$ (not $\theta = \pi$ as in our experiments); this difference does not affect the projected radial position $r = R\sin(\theta)$. Integrating eq (3.14), we obtain the predicted radial trajectory

$$r(t) = R \text{ sech}(k_g t + C), \tag{3.15}$$

where $C > 0$ is a positive constant that determines the particle position at time $t = 0$.

Using this model, we analyzed the multiple trajectories of four different particles sedimenting along the interface of four drops of different sizes (Fig. 3.9a-d). The model agrees with the data at early times, but deviates significantly at later times as the particle begins to interact with the underlying substrate, the three-phase contact line, and any other particles pinned there. Therefore, we focus our analysis exclusively on the data in this early time period. Figure 3.10 shows that the inferred rate parameter k_g decreases with increasing drop size. Accounting for variability in the rate parameter from particle-to-particle (see discussion below), the data agree with the model predictions. The buoyant mass inferred from the fit in Figure 3.10 is $M = 6.3 \times 10^{-15}$ kg, which is roughly two times smaller than the calculated buoyant mass 1.4×10^{-14} kg.

3.8.5.4 Magnetic actuation with gravity

To assess the role of gravity in explaining our experimental observations, we analyzed the data from Figure 3 using the augmented model described Section 3.8.4. In this analysis, the gravitational rate parameter k_g was taken directly from our analysis of the sedimentation in Section 3.8.5.3. We used the same Bayesian MCMC approach detailed in Section 3.8.5.2. Figure 3.11 shows the inferred rate parameter k_m accounting for effects due to gravity force. Even at the weakest fields, the forces due to gravity are still much smaller than those due

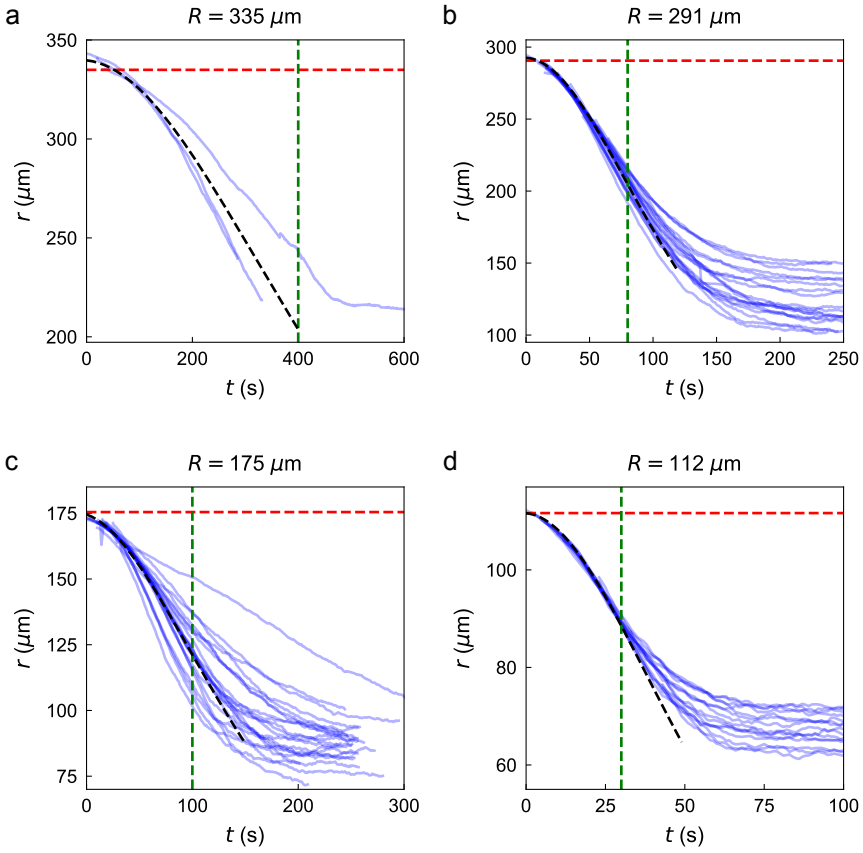

Figure 3.9: Projected radial position as a function of time for four particles sedimenting along the interface of four droplets of different sizes. The model fit (black curve) is based only on data at early times (green line); the red line denotes the drop radius.

to the magnetic field ($G = 0.2 \ll 1$). Consequently, there is only a small change in the inferred rate parameter as compared to that derived using the simpler model that neglects gravitational effects.

3.8.5.5 Variability in Rate Parameter

The variability in particle motions from one particle to the next was assessed using three independent data sets. First and perhaps most directly, we examined the dynamics of multiple particles migrating simultaneously on the same drop when subject to the applied

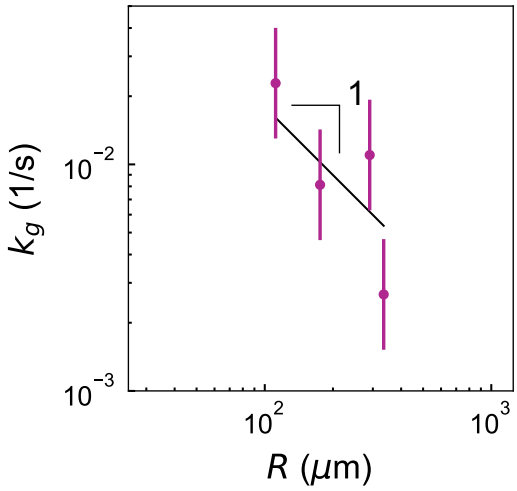

Figure 3.10: Gravitational rate parameter k_g as a function of drop radius as infer from the data in Fig. 3.9. Error bars denote the standard deviationf of the measured rate constant k_g based on 3 to 19 particle trajectories.

field (Supporting Video[2] in Reference [209]). For each of the six particles, we estimated the rate parameter k_m from the reconstructed particle trajectory as described in Section 3.8.5.2. To facilitate the comparison of rate parameters for different conditions spanning orders of magnitude, we will assume that variations in the rate parameter are log-normally distributed with parameters μ_0 and σ_0. Taking the standard deviation of the logarithm of estimates for k_m, we estimate that $\sigma_0 = 0.55$.

Additionally, we analyzed the data in Figure 3b and Figure 3.11 to provide additional estimates of the particle-to-particle variability. Specifically, we modelled the rate parameters k_m in Figure 3b as log-normally distributed with parameters $\mu_1 = C_1/R^2$ and σ_1, where R is the drop radius, and C_1 and σ are unknown constants to be determined by the fitting procedure. Similarly, we modelled the gravitational rate parameters k_g in Figure 3.11 as

[2]This video was captured in bright-field mode in contrast to the other videos we analyzed, which were captured using fluorescence imaging.

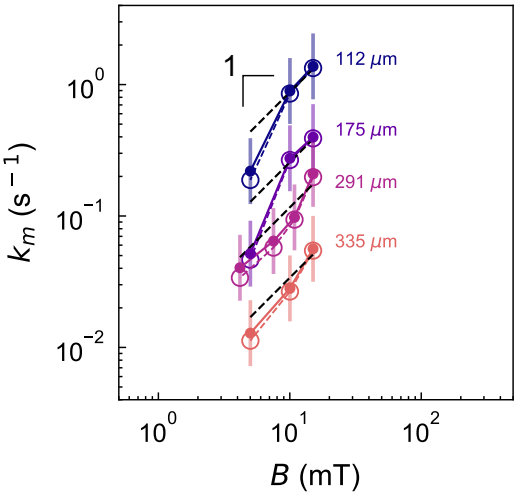

Figure 3.11: Magnetic rate parameter k_m inferred using a model that accounts for magnetic and gravitational forces on the particle. Open markers shows the rate constants k_m from Figure 3, where gravity was not considered.

log-normally distributed with parameters $\mu_2 = C_2/R$ and σ_2. Using Bayesian inference with MCMC sampling, we derived the following estimates for the parameters $\sigma_1 = 0.47$ and $\sigma_2 = 0.63$. These estimates are very similar to that obtained from multiple particles under identical conditions. Ultimately, we conclude that the dynamics of different particles can vary by a factor of $e^{\sigma} = 1.7$. Interestingly, this conclusion applies to particle dynamics driven by magnetic fields and by gravity alone, which suggests that the variations in the drag coefficient λ_t might be responsible (e.g., due to fluctuations in the three-phase contact line [74]).

Chapter 4

Mixing Droplets with Magnetic Janus Particles

4.1 Abstract

When adsorbed at curved liquid interfaces, magnetic particles can be moved by static uniform field due to capillary confinement. A particle moves on the interface such that its magnetic moment aligns with the field. Here, we use precessing magnetic fields to actuate amphiphilic magnetic Janus particles adsorbed at a curved water-decane interface. Depending on the precession angle and frequency, particles orbit the drop poles or zig-zag around the drop equator. We developed a model to explain these complex motions based on the forces and torques exerted on the particle. As shown by simulation and experiment, the particle's orbiting velocity is maximal when the driving frequency equals the characteristic relaxation rate. Commercially available carbonyl iron particles adsorbed at curved liquid interfaces are shown to produce similar complex motions. Particle motion induces fluidic flows inside the droplets, which may be useful for enhancing mass transport in droplet micro-reactors.

4.2 Introduction

Emulsions are dispersions of two immiscible fluids that are kinetically stabilized by surfactants and/or colloidal particles. They can be used as microreactors that allow immiscible reactants to react at the liquid-liquid interface. Reactions can also occur in the dispersed phase such that it reduces the use of organic solvents, mitigates harsh chemical conditions, and enhances heat transfer. The rates of interfacial reactions can be further enhanced by utilizing catalytic particles at the liquid-liquid interface. However, the reaction rate is typically limited by the diffusive transport of reactants or products onto or from the catalyst at the solid-liquid surface [59, 210, 211].

Mixing is an important process to introduce convective flows and increase transport. At the microscale, there exist a number of active or passive methods to improve mixing [212, 213]. Magnetic stirring has advantages over other actuation mechanisms due to its rapid manipulation, contactless control, and biocompatibility [214, 215, 131, 216, 135]. Much of the prior work on micro-mixing has been focused on using self-assembled micro-stir bar [217, 218, 219, 220] or magnetic bacteria [221] inside micro-droplets to induce convective flows. However, the fluid velocity induced by the magnetic stir bars decreases rapidly with distance and limits interfacial mixing.

Here, we demonstrate droplet mixing using particles adsorbed at liquid-liquid interfaces. In a previous paper, we used weak homogeneous magnetic fields to induce particle motion on curved liquid interfaces by magneto-capillary force [209]. Magnetic Janus particles with amphiphilic surface chemistry were used as a model system. The amphiphilic Janus particle binds irreversibly to the interface of water drop in decane due to surface chemistry. Particle rotation normal to the interface is prohibited by strong capillary forces. Application of

weak static uniform field creates torque to the magnetic particle. Due to the interfacial confinement, magnetic torque causes magneto-capillary force that moves particle rapidly across the interface. This force increases linearly with droplet size decreases.

We further investigate magneto-capillary dynamics using time-varying uniform fields and use particle motion for droplet mixing. Application of precessing field causes a particle to perform two dynamic states: zig-zag around the drop equator and pole-orbiting near the drop pole. These two states can be switched reversibly by changing the angle and frequency of the precessing field. We constructed a model that quantitatively describes particle motion in each state. The model matches well with experimental observation. Since larger Péclet numbers ($\boldsymbol{Pe} = \frac{\boldsymbol{uL}}{\boldsymbol{D}}$) are required to significantly enhance rates of mass transfer, we identified experimental conditions maximize the particle velocity. Droplet mixing is demonstrated using commercially available carbonyl iron particles and quantified by the distribution of fluorescent tracers suspended inside the droplet. This droplet mixer may be useful for biphasic reactions and chemical analysis [59, 222, 223, 224].

4.3 Methods

4.3.1 Experiment

Our experiments for quantifying magneto-capillary dynamics were based on magnetic Janus particles (MJPs) with amphiphilic surface chemistry. As previously described [209], successive layers of metal—5 nm Ti adhesive layer, 25 nm Ni magnetic layer, and 20 Au functionalization layer—were deposited onto monolayers of 4 μm fluorescent sulfonated polystyrene (PS) particles by e-beam evaporation [172]. The gold hemispheres of the MJPs were chemically functionalized with 3-mercaptopropionic acid (MPA) to direct their preferred orientation at the decane-water interface [109, 209]. The nickel layer gave the particles

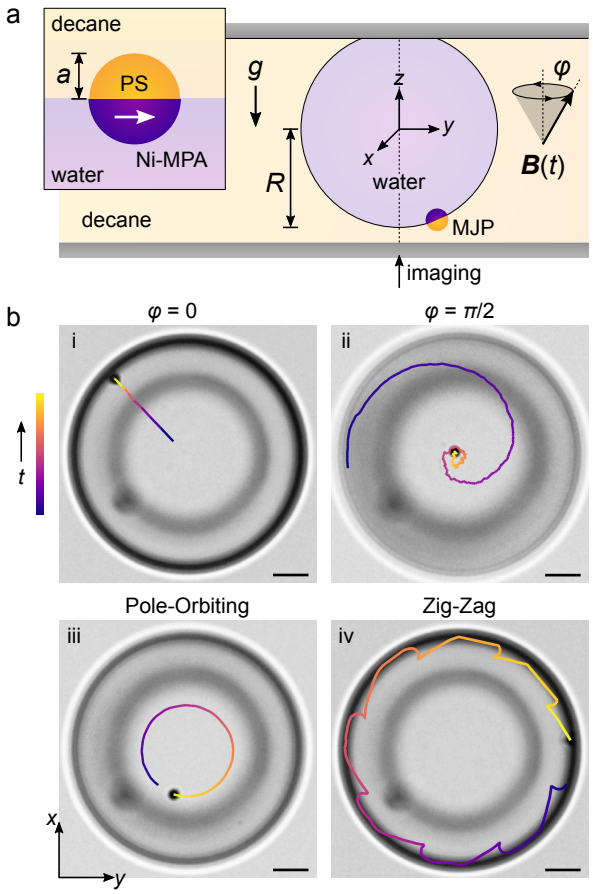

Figure 4.1: (a) Schematic illustration of a magnetic Janus particle (MJP) moving on the curved interface of a water drop in decane due to a precessing magnetic field $\boldsymbol{B}(t)$. The inset shows the preferred orientation of the MJP at the interface and its magnetic moment (white arrow). (b) Optical micrographs of the water drop showing the different types particle trajectories: (i) a static field ($\varphi = 0$) drives the particle to the drop equator; (ii) a rotating field ($\varphi = \pi/2$, $f = 0.028$ Hz) drives the particle to the bottom pole; (iii) a precessing field ($\varphi = 1.0$ rad, $f = 0.35$ Hz) drives the particle to orbit the bottom pole; (iv) a precessing field ($\varphi = 0.8$ rad, $f = 0.35$ Hz) drives the particle to zig-zag across the equator as it orbits the drop. Scale bars are 15 μm.

a permanent magnetic moment $m \approx 3 \times 10^{-14}$ A m^2 directed parallel to the Janus equator [209].

MJPs were deposited onto the interface of a water drop in decane supported between two hydrophobic glass slides (Fig. 4.1a). The particles were first suspended in a mixture of water and isopropyl alcohol (3:1 v/v ratio) and sprayed onto a coverslip treated with a hydrophobic silane to produce small droplets (20 to 200 μm) each containing few particles. The coverslip was incorporated as the ceiling of a glass chamber into which decane was flowed. The chamber was sealed with UV-curable epoxy (NOA 68) and positioned on the stage of an inverted microscope for imaging.

We identified drops containing a single MJP adsorbed at the water-decane interface for use in our investigation. Particles within the pendant drops settled under gravity to the bottom pole. To confirm that a particle was adsorbed at the interface (and not resting above it), we applied a static magnetic field parallel to the gravity direction ($\boldsymbol{B} = B\boldsymbol{e}_z$ with $B = 5$ mT) and monitored the motion of the particle. As described previously [209], particles adsorbed at the interface moved rapidly to the drop equator; those resting above the interface rotated in the field without translation. The orientation of the particle and its response to the applied field was also monitored using a combination of brightfield and fluorescent imaging to visualize both the metal and fluorescent hemispheres, respectively.

Application of a precessing magnetic field $\boldsymbol{B}(t)$ caused the particles to move steadily across the drop interface (Fig. 4.1b). The field was generated using a custom triaxial electromagnet[67] with the following waveform

$$\boldsymbol{B}(t) = B\sin(\varphi)\left[\cos(\omega t)\boldsymbol{e}_x + \sin(\omega t)\boldsymbol{e}_y\right] + B\cos(\varphi)\boldsymbol{e}_z, \tag{4.1}$$

where B is the field strength, ω is the rotation frequency, and φ is the precession angle. In experiment, the magnitude of the field was held constant with $B = 5$ mT as measured by a gaussmeter. The precession angle was varied from $\varphi = 0$, corresponding to a static field in

the z-direction, to $\varphi = \pi/2$, corresponding to a rotating field in the xy-plane. The applied frequency $f = \omega/2\pi$ was varied over three orders of magnitude from $f = 0.023$ to 23 Hz.

4.3.2 Model of MJP Dynamics

We consider the motion of an MJP moving at the interface of a spherical drop under the influence of a time varying field $\boldsymbol{B}(t)$. Three types of forces and torques acts on the particle. In the absence of inertial effect, these forces and torques sum to zero. First the uniform field $\boldsymbol{B}$ imposes a torque $\boldsymbol{L}_m = \boldsymbol{m} \times \boldsymbol{B}$ on particle with magnetic moment $\boldsymbol{m}$. Ideally, the magnetic force equals to zero $\boldsymbol{F}_m = 0$. Strong capillary force $\boldsymbol{F}_c$ and torque $\boldsymbol{L}_c$ forbids particle rotation against the interface and maintain the preferred orientation and location of the particle. As particle move in viscous fluid, its linear $\boldsymbol{U}$ and angular velocity $\boldsymbol{\Omega}$ is related to a hydrodynamic force $\boldsymbol{F}_h$ and torque $\boldsymbol{L}_h$ by the hydrodynamic resistance tensor $[\boldsymbol{F}_h, \boldsymbol{L}_h] = -\boldsymbol{\mathcal{R}} \cdot [\boldsymbol{U}, \boldsymbol{\Omega}]$. Since the particle adsorbs at a spherical interface, its translation is related to the rotation by the kinematic constraint $\boldsymbol{U} = \boldsymbol{\Omega} \times \boldsymbol{x}_p$, where $\boldsymbol{x}_p$ is the particle position measured from the drop center. The work given by magnetic torque is dissipated through the motion in viscous surroundings. Here, the capillary force and torque provide kinetic constraint but no work. Thus, the magnetic torque is dissipated to hydrodynamic torque and force $\boldsymbol{L}_m \cdot \boldsymbol{\Omega} + \boldsymbol{F}_h \cdot \boldsymbol{U} + \boldsymbol{L}_h \cdot \boldsymbol{\Omega} = 0$ for any magnetic torque $\boldsymbol{L}_m$. Together, these relations specify the motion of the particle on the drop surface.

The resistance tensor is approximated by a sphere in an unbounded fluid with an effective viscosity equal to the average viscosity of the two liquids. This approximation neglects the viscosity contrast between the two liquids as well as the effects of drop curvature on the resistance tensor, which is appropriate for spherical particles adsorbed on large drops ($R \gg a$). We use a body-fixed coordinate system centered on the particle to express

equations of motion(Fig. 4.2) [225]. In this reference frame, the angular velocity of the particle $\boldsymbol{\Omega}'$ is related to the magnetic torque $\boldsymbol{L}'_m$ in the following manner

$$(\lambda_t R^2 + \lambda_r)\Omega'_x = L'_{m,x}, \quad (\lambda_t R^2 + \lambda_r)\Omega'_y = L'_{m,y}, \quad \lambda_r \Omega'_z = L'_{m,z}, \tag{4.2}$$

where $\lambda_t = 6\pi\eta a$ and $\lambda_r = 8\pi\eta a^3$ are the resistance coefficients for sphere translation and rotation. The MJP's magnetic moment $\boldsymbol{m}'$ is constant and aligns the x'-direction parallel to the interface (Fig. 4.2) [209]. Together with the kinematics of rigid body motion, equation (4.2) fully specify the particle dynamics in the applied field $\boldsymbol{B}(t)$.

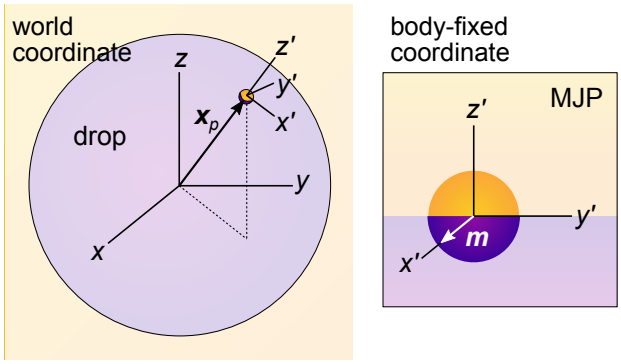

Figure 4.2: Coordinate systems used in the formulation of the dynamical model.

The particle dynamics is characterized by multiple length and time scales. Upon application of the field, the particle rotates quickly about the z' axis with a characteristic rate $mB/8\pi\eta a^3$. For the experimental conditions ($a = 2$ μm, $\eta = 0.001$ Pa s, $m = 3 \times 10^{-14}$ A m^2, and $B = 10$ mT), this rate is estimated to be 1500 s^{-1}, which is considerably faster than the frequency ω of the applied field. Additionally, the particle moves across the surface of the drop with a characteristic rate $\omega_o = mB/6\pi\eta a R^2$, which is slower by a factor of $(R/a)^2$ [209]. For a particle moving on a drop of radius $R = 100$ μm, this rate is estimated to be 0.60 s^{-1}. We anticipate qualitatively different dynamics depending on the magnitude of the applied frequency relative to this time scale. Scaling lengths by R and time by ω_o^{-1},

the model is fully characterized by three dimensionless parameters: the size of the particle $\alpha = a/R$, the frequency of the field $\beta = \omega/\omega_o$, and the precession angle φ. We focus our analysis on small particles ($\alpha \ll 1$) subject to applied fields of different angles φ and frequencies β.

4.4 Results and Discussions

4.4.1 Single Particle Dynamics

Depending on the rotation frequency and the precession angle, we observed four types of particle motion on the spherical interface. In static fields ($\varphi = 0$), the MJP moved along a great circle to rest at the drop equator (Fig. 4.1b,i) [209]. In rotating fields ($\varphi = \pi/2$), the particle moved along a spiral trajectory to the bottom pole of the drop, where it rotated steadily about the z-axis (Fig. 4.1b,ii). The addition of a small static component to the rotating field ($\varphi < \pi/2$) caused the particle to move in a circular orbit about the bottom pole (denoted "pole orbiting" in Fig. 4.1b,iii). Decreasing the precession angle further, the particle began to zig-zag back and forth across the equator as it slowly orbited drop (denoted "zig-zag" in Fig. 4.1b,iv).

The conditions under which each motion was observed are summarized by the dynamical phase diagram of Figure 4.3a. The particle was initially positioned at the bottom pole of the drop. Application of a precessing field with frequency ω and angle φ caused the particle to move in time towards a stable periodic orbit about the drop pole (pole orbiting) or the drop equator (zig-zag). For comparison with the model, the frequency is presented using the dimensionless parameter, $\beta = \omega/\omega_o$, which measures the applied frequency relative to the characteristic relaxation rate at which the MJP approaches its stable orbit. The data suggests that the pole orbiting behavior is observed only at high frequencies ($\beta > 1$) and

for precession angles greater than 45° ($\varphi > \pi/4$).

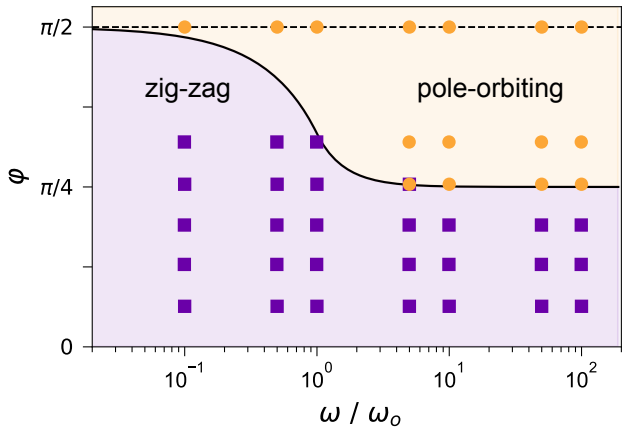

Figure 4.3: Dynamical phase diagram showing the type of particle motion as a function of the rotation frequency ω and the precession angle φ. The frequency is scaled by the characteristic relaxation rate $\omega_o = mB/6\pi\eta aR^2$. Markers represent data from four experiments with the particle initialized at the bottom pole of the drop. The black curve shows the stability boundary for the pole-orbiting solution as predicted by the model. For $\varphi = \pi/4$ and $\omega/\omega_0 = 5$, three of four particles showed the pole-orbiting motion while one showed the zig-zag motion.

Interestingly, the particle dynamics exhibited bistability whereby different initial conditions led to different motions in the same applied field. Figure 4.7 shows a second phase diagram in which the particle is initially positioned at the drop equator by application of a static field. For the rotation frequencies and precession angles explored, the pole orbiting motions are no longer observed; instead, the particle exhibits zig-zag motions around the drop equator. We note that some regions of the phase diagram could not be explored in experiment. In particular, for large precession angles, the particle zig-zagged back and forth across the drop equator with large amplitudes. Such large excursions onto the top hemisphere of the drop led the particle to adsorb irreversibly at the three-phase contact line, thereby preventing further experiments.

The pole-orbiting and zig-zag motions observed in experiment are reproduced by the mathematical model. Figure 4.4 shows two particle trajectories computed numerically for different precession angles ($\varphi = 1.2$ and $\varphi = 0.7$) with $\alpha = 0.02$ and $\beta = 1$. To better understand the origins of these motions, we note that the particle dynamics become dramatically simpler when viewed from a different perspective that follows the motion of the precessing field (Fig. 4.4, bottom). This view corresponds to a rotating coordinate system centered on the drop and related to the world coordinates as

$$\boldsymbol{x}'' = \boldsymbol{R}'\boldsymbol{x} \quad \text{with} \quad \boldsymbol{R}' = \begin{bmatrix} -\cos(\varphi)\cos(\omega t) & -\cos(\varphi)\sin(\omega t) & \sin(\varphi) \\ \sin(\omega t) & \cos(\omega t) & 0 \\ -\cos(\omega t)\sin(\varphi) & \sin(\varphi)\sin(\omega t) & \cos(\varphi) \end{bmatrix} \tag{4.3}$$

In the rotating coordinates, the applied field is stationary $\boldsymbol{B}'' = B\boldsymbol{e}_z''$, while the fluid rotates steadily with an angular velocity $-\omega(\sin\varphi\boldsymbol{e}_x'' + \cos\varphi\boldsymbol{e}_z'')$. In this frame of reference, the pole-orbiting motion corresponds to a stable fixed point and the zig-zag motion to a steady periodic orbit.

The position of the particle with respect to the rotating coordinates is conveniently parameterized by the polar angle θ and the azimuthal angle ϕ in the rotating frame (Fig. 4.4). In the limit of small particles ($\alpha \to 0$), the orientation of the particle about its z'-axis evolves quickly to a stationary value. The slower dynamics of θ and ϕ can then be expressed as

$$\dot{\theta} = \cos\theta + \beta\sin\varphi\sin\phi, \tag{4.4}$$

$$\dot{\phi} = \beta\sin\varphi\cos\phi\cot\theta - \beta\cos\varphi, \tag{4.5}$$

where time is scaled by ω_o^{-1}, β is the dimensionless frequency, and φ is the precession angle. For static fields ($\beta \to 0$), these dynamics simplify to those derived previously: the particle moves along a great circle to the drop equator in the $x''y''$ plane [209]. The rotation of the

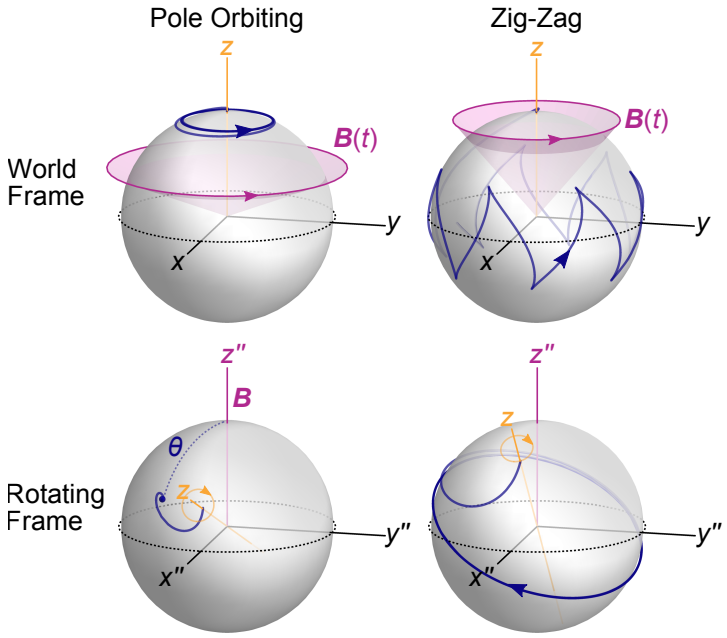

Figure 4.4: Computed particle trajectories (navy) in the world coordinates (top) and the rotating coordinates (bottom) for the two types of particle motions: pole orbiting (left) with $\varphi = 1.2$ and zig-zag (right) with $\varphi = 0.7$. The dimensionless particle size is $\alpha = 0.02$; the frequency parameter is $\beta = 1$. Initially, the particles is located near the north pole of the droplet.

fluid about an axis oblique to the field displaces the particle from the drop equator, either to a new stable position (the pole orbiting solution) or to a periodic orbit (the zig-zag solution). Below, we analyze the approximate dynamics of equations (4.4) and (4.5) to identify the necessary conditions for these solutions as well as their distinguishing characteristics.

4.4.1.1 Pole Orbiting Solutions

The pole orbiting behaviors observed in experiment correspond to stable fixed points of the dynamics (4.4) and (4.5) denoted (θ_o, ϕ_o). The particle does not move from these locations $(\dot{\phi} = \dot{\theta} = 0)$ and returns if perturbed. These stable solutions exist when the precession

angle is larger than some critical value,

$$\varphi > \varphi^*(\beta) = \begin{cases} \frac{1}{2}\arccos\left[\frac{1}{2}(-2+\beta^2)\right] & \text{for } \beta \leq 1, \\ \frac{1}{2}(-2\beta^2) & \text{for } \beta > 1, \end{cases} \tag{4.6}$$

as illustrated in the dynamical phase diagram (Fig. 4.3; see also Fig.4.8). For purely rotating fields ($\varphi = \pi/2$), the particle is always stable at the two poles of the drop along the axis of rotation ($\theta_o = \pi/2$ in the rotating frame). The addition of a static field component in the z-direction (i.e., for $\varphi < \pi/2$) causes a displacement of the particle from the poles by an angle $\varphi - \theta_o$, which is greatest for precession angles approaching the stability boundary $\varphi = \varphi^*(\beta)$. Under these conditions, the polar angle $\varphi - \theta_o$ of the particle orbit increases from zero at low frequencies ($\beta \ll 1$) to a maximum value of $\pi/12$ at $\beta = 1$ before returning to zero at high frequencies ($\beta \gg 1$; Fig.4.9).

4.4.1.2 Zig-Zag Solutions

To better understand the zig-zag behavior, we consider first the small frequency regime ($\beta \ll 1$) for which approximate solutions can be derived using perturbation analysis. Under these conditions, the polar angle θ evolves to a constant value, $\theta = \pi/2 + O(\beta)$, as the particle moves to the drop equator (in the rotating frame). At first order in β, the azimuthal angle ϕ decreases at a steady rate, $\dot{\phi} = -\beta\cos\varphi + O(\beta^2)$, as the particle orbits the drop equator. Such orbital motion in the rotating frame corresponds to zig-zag motion in the world frame with an angular amplitude of φ above/below the equator, an oscillation frequency of $\beta\cos\varphi$, and an angular velocity of $\Omega_z = \beta(1-\cos\varphi)$ about the z-axis. During each orbit of the drop, the particle performs $\cos\varphi/(1-\cos\varphi)$ zig-zag cycles, which decreases monotonically with increasing precession angle.

To test these predictions in an experiment, we measured the average angular velocity of

the particle about the z-axis $\langle \Omega_z \rangle$ as a function of the driving frequency ω and the precession angle φ. This velocity measures the number of times that the particle orbits the drop equator per unit time. Figure 4.5 shows that the average angular velocity increases linearly with increasing ω at small frequencies ($\omega \ll \omega_o$) with larger precession angles corresponding to faster orbital motions. The experimental results are in quantitative agreement with the approximate solution derived for low frequencies ($\omega \ll \omega_o$, solid curves). The orbital velocity reaches a maximum value for frequencies $\omega \sim \omega_o$ and decays toward zero at higher frequencies.

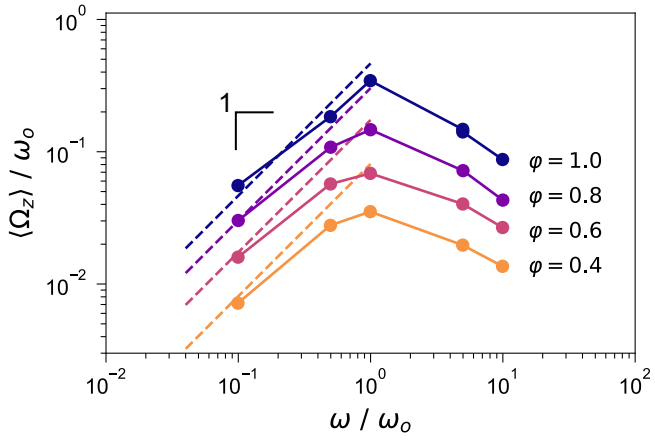

Figure 4.5: Average angular velocity of the particle about the z-axis $\langle \Omega_z \rangle$ as a function of the driving frequency ω and the precession angle φ. Both $\langle \Omega_z \rangle$ and ω is scaled by the characteristic relaxation rate ω_o.

4.4.2 Mixing

We used commercially available paramagnetic carbonyl iron particles (Sigma-Aldrich, C3518) and 2 μm fluorescent polystyrene particles (Thermo Fisher, F8826) to demonstrate droplet mixing. Aqeuous solution containing magnetic and tracer particles were mixed with isopropyl alcohol in 3:1 v/v ratio. The mixture was then sprayed on the hydrophobic coverslip

and incorporated into a chamber filled with decane, as previously described. Static uniform field parallel to the gravity direction was used to confirm carbonyl iron particles adsorbtion at the interface. Distribution of fluorescent tracer particles indicates fluid flow in the water droplet. Between each experiment, the field was off for at least 1 hour to let tracers settle. Steady motions of magnetic particles at curved liquid cause fluidic flow. Fundamental studies of dynamic motion by magneto-capillary force are performed using a modeling system with magnetic Janus particles. However, it is challenging to mass produce Janus particles by the current surface modification technique. Instead, we use commercially available superparamagnetic carbonyl iron particles with high susceptibility to demonstrate mixing droplets.

When adsorbed at the interface, carbonyl particles form aggregated "rafts" possibly due to magnetic dipole or capillary attractions. These particles are superparamagnetic and develop magnetic moment proportional to the applied field $\boldsymbol{m} = \boldsymbol{\chi} \cdot \boldsymbol{B}$ where $\boldsymbol{\chi}$ is the magnetic susceptibility tensor. Presence of uniform static field rotates the magnetic "rafts" such that their major axis is parallel to the field and the "rafts" move radially toward water drop equator by magneto-capillary forces (Fig.4.10). The "rafts" can be modeled as disks, with stronger magnetic susceptibility parallel to the interface than that perpendicular to the interface ($\chi_{\parallel}<\chi_{\perp}$). As time goes by, projected radial displacement is

$$r(t) = R[1 + \exp(-2k_m t + C)]^{-1/2} \tag{4.7}$$

where $k_m = (\chi_{\parallel} - \chi_{\perp})B^2/\lambda_t R^2$ is the rate constant, η_t is the resistance coefficient that describes a circular disk with radius b moving parallel to its major axis: $\lambda_t \approx \frac{32}{3}\eta b$ [66], and C is a constant that relates to particle's initial position. The model quantitatively agrees with the experiment and shows that paramagnetic particles have sigmoidal trajectories,

which is different from ferromagnetic Janus particles.

The carbonyl iron aggregates perform zig-zag or pole-orbiting motion with the presence of a precessing field. Precessing field with $f = 0.67Hz$ and $\varphi = \pi/3$ was applied to move carbonyl iron particle at the drop interface. The motion of tracer particles inside the drop was observed using fluorescent microscopy. Mixing was quantified by monitoring image standard deviation (I_{std}) as a function of time. At the beginning of the experiment, tracer particles settled at the drop bottom (fig.4.6a). In a mixed drop, tracers distributed evenly inside the drop and the image standard deviation was lowered (fig.4.6b). We compared mixing efficiency in three experimental conditions: a) two aggregates in a continues precessing field, b) one aggregate in a continues precessing field, and c) one aggregate in the precessing field that was off for 2.7 seconds and on for 50 seconds (denoted "w/ breaks" in figure 4.6c). The sum of two magnetic aggregates volume in experiment (a) equals to the one aggregate's volume in experiment (b) and (c). In experiment (a), the smaller aggregate orbited about the south pole while the larger aggregate zig-zagged around the drop equator. Precessing field made the one particle in experiment b and c preform zig-zag motion. When the field was on, image standard deviation decreased as time goes by until it reached steady-state (fig. 4.6c). The steady states values showed that one aggregate with zig-zag motion alone was not efficient in mixing the drop since its motion couldn't mix regions near the south pole. This shortcoming was alleviated by using two aggregates or letting the field take "breaks". When the field was off (i.e. taking "breaks"), iron aggregate settled to the south pole by gravity. Re-application of precessing field made the aggregate move from drop bottom to drop equator and thereby mix fluid near the south pole.

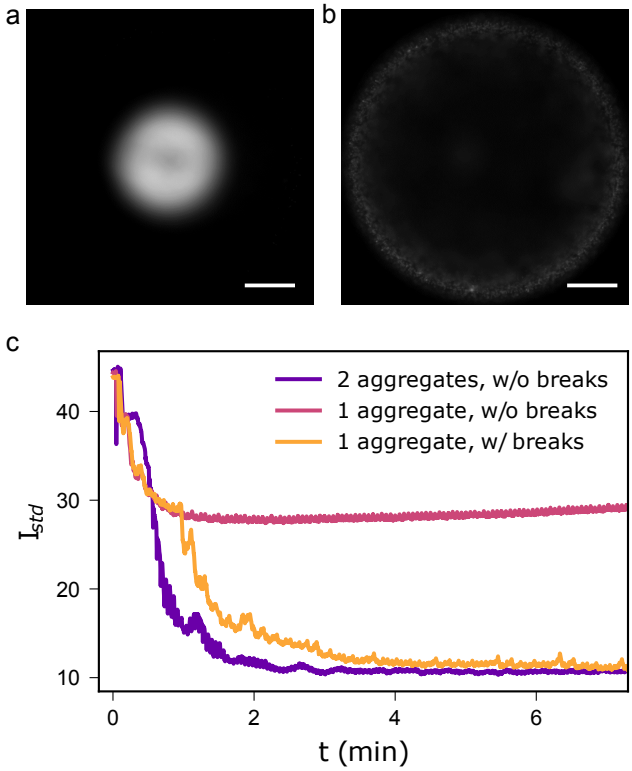

Figure 4.6: Fluorescent images of water drop contain tracer particles (a) before and (b) after applying the precessing field. Scale bar is 100μm. (c) The standard deviation of microscopy image (I_{std}) decreases as a function of time due to magnetic particle motion. In the precessing field with "breaks", the field was on for 50 s, then off for 2.7 s to let magnetic aggregates to settle.

4.5 Conclusions

Precessing magnetic fields induce pole-orbiting or zig-zag particle motion at the interface of water drop in decane. Considering torques and forces on the particle, we constructed a model that fully specifies the particle dynamics in the applied field. Both the model and experimental data suggests that particle presents a zig-zag motion about the drop equator when precessing angle is smaller than a critical value. At a critical precessing frequency and angle, particle orbit velocity and amplitude are maximized in the zig-zag motion. Carbonyl

iron particles form rafts at the interfaces and present both zig-zag and pole-orbiting motion by precessing field. The steady motion agitates nearby fluids and causes fluidic flow in the bulk fluids. Flows are monitored using fluorescent tracer particles inside the water droplet. Two magnetic aggregates in one drop can present the zig-zag and pole-orbiting motion at the same time by precessing field. Tracks from these two aggregates cover a high surface fraction of the droplet and enhance mixing inside the drop. We will simulate the particle dynamics and the induced flows on spherical interfaces in the near future. Carbonyl iron particles used here are commercially available and mixing induced by dynamic magneto-capillary motion can be easily scaled up for industrial use in enhancing the rate of organic synthesis, bisphasic catalysis, and chemical analysis [59, 222, 223, 224].

4.6 Acknowledgements

This work was supported as part of the Center for Bio-Inspired Energy Science, an Energy Frontier Research Center funded by the U.S. Department of Energy, Office of Science, Basic Energy Sciences under Award DE-SC0000989.

4.7 Supplimentary Information

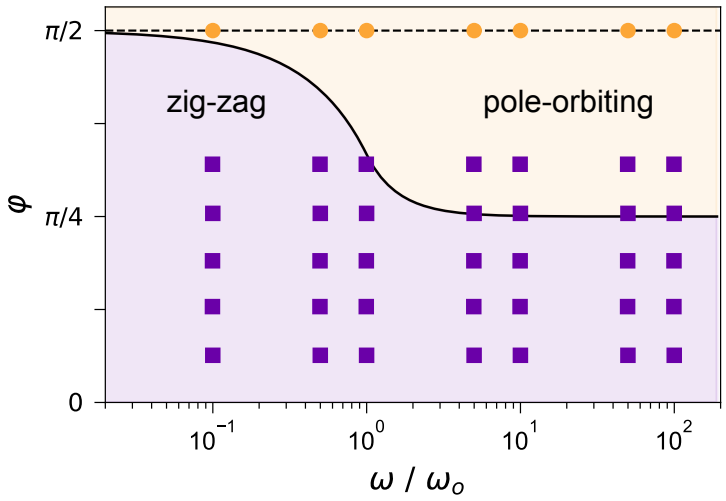

Figure 4.7: Dynamical phase diagram showing the type of particle motion as a function of the rotation frequency ω and the precession angle φ. The frequency is scaled by the characteristic relaxation rate $\omega_o = mB/6\pi\eta aR^2$. Markers represent data from four experiments with the particle initialized **at the drop equator**. The black curve shows the stability boundary for the pole-orbiting solution as predicted by the model.

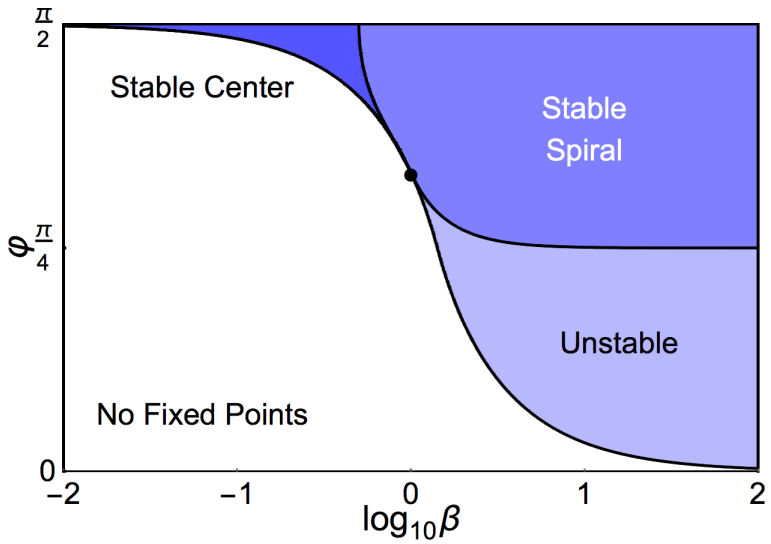

Figure 4.8: Dynamical phase diagram showing the existence and stability of fixed points for equations (4) and (5) as a function of the rotation frequency $\beta = \omega/\omega_o$ and the precession angle φ.

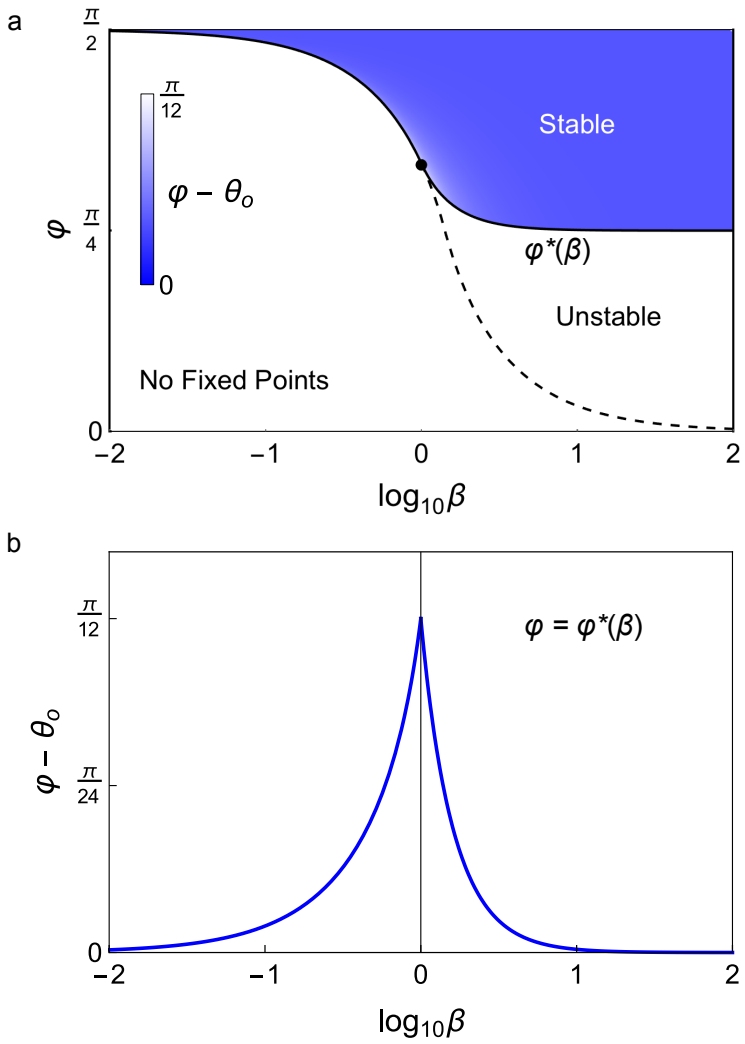

Figure 4.9: In the dynamics of equations (4) and (5), pole-orbiting motions are characterized by the polar angle $\varphi - \theta_o$ measured from the z-axis of the world frame to the particle center. (a) This angle is close to zero for most frequencies β and precession angles φ, reaching a maximum value of $\pi/12$ for $\beta = 1$ and $\varphi = \varphi^*$. (b) For precession angles equal to the critical value $\varphi^*(\beta)$, the angle $\varphi - \theta_o$ is maximal at the frequency $\beta = 1$.

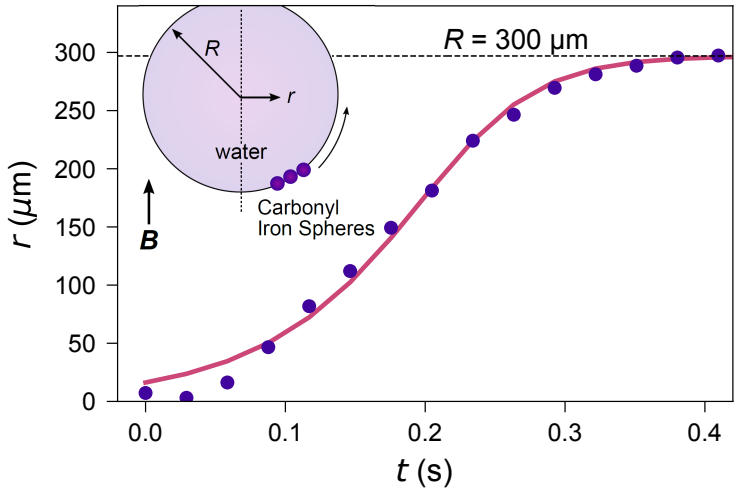

Figure 4.10: Radial trajectories of paramagnetic particles on a water/decane interface. Markers show the experimental data; the solid curve shows the prediction of equation (7) with $k_m = 13\ \mathrm{s}^{-1}$.

Chapter 5

Conclusion and Future Outlook

5.1 Conclusion

Fluid-fluid interface influences active particles motion due to confinement, viscosity contrast and curvature, and rise new physics for propulsion such as Marangoni effect and capillary interactions. Motion of active colloidal particles at the fluidic interface is different from their motion in the bulk, both qualitatively and quantitatively. Interface confines the particles orientation and limit their trajectories. Viscosity contrast and curvature influences particle response to external fields. Interfacial tension difference drives the particle or fluid motion. Interfacial disturbance created by particle adsorption induces their attractive or repulsive motion.

Magnetic manipulation is favored in the active colloid community since it controls active particles rapidly and remotely, and has minimal effect to the surrounding media. Such properties are useful for microsurgery, drug-delivery, and water remediation [30, 32] . Magnetic particles can be steered by field gradient, static or time-varying uniform fields. Depending on the particle and its immersed fluid material, they can be categorized as ferromagnetic, paramagnetic, or diamagnetic. Equations expressing magnetic force and torques are sum-

marized in chapter 2.

Amphiphilic Janus particles are commonly used as model systems to study particle dynamics at liquid-liquid interfaces. Due to surface chemistry anisotropy, Janus particles bind irreversibly at an oil-water interface with hydrophilic side facing water. Methods to fabricate Janus particles includes phase separation and surface modification. Particles used in chapter 3 and 4 are fabricated by template assisted metal deposition method. Their magnetic properties are quantified by spinning them near a solid planar boundary using rotating magnetic field. Balancing magnetic and hydrodynamic torque on the particle reveals its magnetic moment.

Chapter 3 demonstrates magneto-capillary effect that drives particles rapid motion on curved liquid interfaces using static uniform field. Ferromagnetic amphiphilic Janus particle adsorbs at the interface of spherical water drop immersed in decane. Strong interfacial tension forbids particle rotation normal to the interface and thus couples its position and direction. Thus, magnetic torque supplied by static uniform field drives particle motion at curved liquid interface such that particles magnetic moment aligns with the field. This magneto-capillary forces scales linearly with field strength and drop curvature as $F \sim mB/R$. For small droplets, the magneto-capillary force can be many orders stronger to that induced by field gradient. Furthermore, this effect is broader than model system of magnetic Janus particles. Anisotropic magnetic particles adsorb at curved liquid interfaces with preferred orientation are expected to have similar responses.

Time-varying field on magnetic particles adsorbed at curved liquid interfaces causes dynamic response and can be used to mix micro droplet reactors. Particularly, precessing field makes the particle to present two dynamical states: zig-zag motion and pole-orbit motion. Particles motion can be switched from one state to the other by varying field

precessing angle and/or frequency. These behaviors are explained by a simple physical model based on applied magnetic torque, interfacial constraint, and hydrodynamic dissipation as the particle moves in the fluid. The periodic particle motion at the curved interface induces fluidic flow both at the interface and far from the interface. Besides Janus particles, superparamagnetic carbonyl iron particles present similar zig-zag and pole-orbiting motion at the curved liquid interface when induced by precessing field. Due to their high magnetic material content, these particles have a high relaxing rate constant than that of the Janus particles and move rapidly at the interface. Fluidic flow induced by carbonyl iron particles was visualized using tracers particles suspended inside the aqueous drop. Zig-zag motion along is not sufficient enough to disperse tracer particles due to the absence of active particles moving near the drops south pole. It is found that mixing is most efficient when two magnetic carbonyl iron aggregates present in the drop, with one zig-zag along the interface and the other pole-orbit near the bottom. In this way, trajectory from the active particle covers higher fraction of the surface area. Mixing droplets with magneto-capillary dynamics will be useful for enhance reaction rates in droplet micro-reactors, emulsion reactions, and chemical analysis.

5.2 Future Works

5.2.1 Shape induced auto motion

In this thesis we analyzed motion of spherical particles at curved interface induced by static and time-varying uniform fields quantitatively using simple physical models. There exist other design variables to broadens the single particle motion. First is the magnetic property. As demonstrate in chapter 4, paramagnetic carbonyl iron aggregates have different response to static uniform fields compared to the ferromagnetic Janus particles. Secondly,

shape anisotropy could change particles magnetic response and hydrodynamic resistance and thereby control particle motion in the magnetic field. Investigations of how shape anisotropy influence the particle motion could enable programmable particle motors by simply designing their shape. It would be interesting to use both experiments and theory to explore the parameter space and map out possible particle motion in dynamic field as time evolves. Such behavior can be used for programmable magnetic robots. Similar idea has been demonstrated in a previous simulation study of categorizing anisotropic particle motion actuated by induced-charge electrophoresis (ICEP) [226]. This study inspired the discovery of helical motions in experiments [227].

5.2.2 Non-spherical liquid interface

Magneto-capillary dynamics demonstrated in chapter 3 and 4 are performed on spherical drops. For any arbitrary point on a spherical drop, two principle radii of curvature (R_1 and R_2) equals to drop radius due to symmetry. The deviatoric curvature, which is defined as $\Delta c = c_1 - c_2 = 1/R_1 - 1/R_2$, is everywhere zero. Particle adsorbs and disturbs the liquid-liquid interface and forms capillary quadrupole. When adsorbs at non-spherical (i.e. non-zero deviatoric curvature) interface, particle moves to the region with higher deviatoric curvature by capillary force to reduce interfacial energy. It is interesting to explore how this capillary force compete with magnetic force. Experimentally, non-spherical interfaces can be created by micro-posts following procedure demonstrated by Stebe et al. [112]. Magnetic Janus particles can be used in this model system. When the field is absent, particle accumulate near the micro-posts theoretically, where the deviatoric curvature is highest [112]. Application of static uniform field parallel to the interfacial curvature minima could make the particle take off from the pole such that its magnetic moment align with the

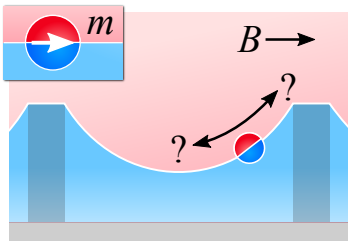

Figure 5.1: Motion of magnetic Janus particles on capillary 'landscapes' created by micro-posts.

field (Fig. 5.1). The interfacial curvature will be tuned to make the capillary force in the same order of magnitude of the magnetic force provided by the uniform field. Furthermore, magnetic field orientation and strength and the geometry of curved interface can be designed and altered to program particle trajectory.

5.2.3 Active Assembly at curved interfaces

Particle assembly is one of the bottom-up approaches to fabricate functional materials [197]. Dynamics of multiple particles at curve interface induced by uniform magnetic field has yet to be explored. Rich behavior of particles is expected since many interparticle interactions, such as magnetic, capillary, electrostatic, hydrodynamic, and steric interactions can influence particles distribution. In chapter 3 we observed orientation and assembly of magnetic Janus particles at planar liquid interfaces. Particles repel from one and another and form closely packed hexagonal lattice due to strong electrostatic dipole. Similar method can be used to make particles monolayer at curved liquid interfaces. In a simple static uniform field, particles are expected to form a ring near the drop equator (Fig. 5.2). To ensure magnetic manipulation is reversible for a long timeframe, particles magnetic content or magnetic field strength needs to be carefully tuned. Meanwhile, field direction, droplet size and particle surface chemistry are expected to influence particle assembly at drop

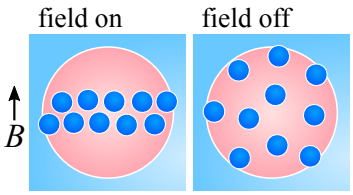

Figure 5.2: Reversible assembly induced by weak static uniform field.

surface. Understanding dynamics and assembly of particles at curved liquid interface will be useful for developing sensors [30] and stimuli responsive materials [130, 25, 38, 42].

Bibliography

[1] Konstantin V Tretiakov, Kyle J M Bishop, and Bartosz A Grzybowski. The dependence between forces and dissipation rates mediating dynamic self-assembly. *Soft Matter*, 5:1279–1284, 2009.

[2] Fernando Martinez-Pedrero, Antonio Ortiz-Ambriz, Ignacio Pagonabarraga, and Pietro Tierno. Colloidal Microworms Propelling via a Cooperative Hydrodynamic Conveyor Belt. *Phys. Rev. Lett.*, 115:138301, 2015.

[3] Xiaolu Wang, Martin In, Christophe Blanc, Maurizio Nobili, and Antonio Stocco. Enhanced active motion of Janus colloids at the water surface. *Soft matter*, 11:7376–7384, 2015.

[4] Rastko Sknepnek and Silke Henkes. Active swarms on a sphere. *Phys. Rev. E - Stat. Nonlinear, Soft Matter Phys.*, 91:022306, 2015.

[5] Eric Lauga and Anthony M. J. Davis. Viscous Marangoni propulsion. *J. Fluid Mech.*, 705:120–133, 2012.

[6] Claudio Maggi, Filippo Saglimbeni, Michele Dipalo, Francesco De Angelis, and Roberto Di Leonardo. Micromotors with asymmetric shape that efficiently convert light into work by thermocapillary effects. *Nat. Commun.*, 6:7855, 2015.

[7] Satoshi Nakata, Hiroya Yamamoto, Yuki Koyano, Osamu Yamanaka, Yutaka Sumino, Nobuhiko J. Suematsu, Hiroyuki Kitahata, Paulina Skrobanska, and Jerzy Gorecki. Selection of the rotation direction for a camphor disk resulting from chiral asymmetry of a water chamber. *J. Phys. Chem. B*, 120:9166–9172, 2016.

[8] Siowling Soh, Michal Branicki, and Bartosz A. Grzybowski. Swarming in shallow waters. *J. Phys. Chem. Lett.*, 2:770–774, 2011.

[9] Qingguang Xie, Gary Davies, Florian Günther, and Jens Harting. Tunable dipolar capillary deformations for magnetic Janus particles at fluid-fluid interfaces. *Soft Matter*, 11:3581–3588, 2015.

[10] Qingguang Xie, Gary B Davies, and Jens Harting. Controlled capillary assembly of magnetic Janus particles at fluid-fluid interfaces. *Soft Matter*, 12:6566–6574, 2016.

[11] John W.M. Bush and David L. Hu. Walking on water: Biolocomotion at the interface. *Annu. Rev. Fluid Mech.*, 38:339–369, 2006.

[12] David L. Hu, Manu Prakash, Brian Chan, and John W. M. Bush. Water-walking devices. *Exp. Fluids*, 43:769–778, 2007.

[13] G. Grosjean, G. Lagubeau, A. Darras, M. Hubert, G. Lumay, and N. Vandewalle. Remote control of self-assembled microswimmers. *Sci. Rep.*, 5:16035, 2015.

[14] A. Snezhko, M. Belkin, I. S. Aranson, and W. K. Kwok. Self-assembled magnetic surface swimmers. *Phys. Rev. Lett.*, 102:118103, 2009.

[15] Samuel Sánchez, Lluis Lluís Soler, and Jaideep Katuri. Chemically powered micro- and nanomotors. *Angew. Chemie Int. Ed.*, 54:1414–1444, 2015.

[16] Krishna Kanti Dey, Flory Wong, Alicia Altemose, and Ayusman Sen. Catalytic motors-quo vadimus? *Curr. Opin. Colloid Interface Sci.*, 21:4–13, 2015.

[17] S. J. Ebbens. Active colloids: Progress and challenges towards realising autonomous applications. *Curr. Opin. Colloid Interface Sci.*, 21:14–23, 2016.

[18] Clemens Bechinger, Roberto Di Leonardo, Hartmut Löwen, Charles Reichhardt, Giorgio Volpe, and Giovanni Volpe. Active particles in complex and crowded environments. *Rev. Mod. Phys.*, 88:045006, 2016.

[19] Andreas Zöttl and Holger Stark. Emergent behavior in active colloids. *J. Phys.: Condens. Matter*, 28:253001, 2016.

[20] Jeffrey L. Moran and Jonathan D. Posner. Phoretic self-propulsion. *Annu. Rev. Fluid Mech.*, 49:511–540, 2017.

[21] Corinna C. Maass, Carsten Krüger, Stephan Herminghaus, and Christian Bahr. Swimming droplets. *Annu. Rev. Condens. Matter Phys.*, 7:171–193, 2016.

[22] Jinxing Li, Isaac Rozen, and Joseph Wang. Rocket science at the nanoscale. *ACS Nano*, 10:5619–5634, 2016.

[23] Alexey Snezhko. Complex collective dynamics of active torque-driven colloids at interfaces. *Curr. Opin. Colloid Interface Sci.*, 21:65–75, 2016.

[24] J Elgeti, R G Winkler, and G Gompper. Physics of microswimmers–single particle motion and collective behavior: A review. *Rep. Prog. Phys.*, 78:056601, 2015.

[25] K. Jagajjanani Rao, Fei Li, Long Meng, Hairong Zheng, Feiyan Cai, and Wei Wang. A force to be reckoned with: A review of synthetic microswimmers powered by ultrasound. *Small*, 11:2836–2846, 2015.

[26] Alison E. Patteson, Arvind Gopinath, and Paulo E. Arratia. Active colloids in complex fluids. *Curr. Opin. Colloid Interface Sci.*, 21:86–96, 2016.

[27] Hong Wang and Martin Pumera. Fabrication of micro/nanoscale motors. *Chem. Rev.*, 115:8704–8735, 2015.

[28] Stefano Sacanna and David J. Pine. Shape-anisotropic colloids: Building blocks for complex assemblies. *Curr. Opin. Colloid Interface Sci.*, 16:96–105, 2011.

[29] M. Cristina Marchetti, Yaouen Fily, Silke Henkes, Adam Patch, and David Yllanes. Minimal model of active colloids highlights the role of mechanical interactions in controlling the emergent behavior of active matter. *Curr. Opin. Colloid Interface Sci.*, 21:34–43, 2016.

[30] Jinxing Li, Berta Esteban-Fernández de Ávila, Wei Gao, Liangfang Zhang, and Joseph Wang. Micro/nanorobots for biomedicine: Delivery, surgery, sensing, and detoxification. *Sci. Robot.*, 2:eaam6431, 2017.

[31] Bahareh Kherzi and Martin Pumera. Self-propelled autonomous nanomotors meet microfluidics. *Nanoscale*, 8:17415–17421, 2016.

[32] Wei Gao and Joseph Wang. The environmental impact of micro / nanomachines : A review. *ACS Nano*, pages 3170–3180, 2014.

[33] Virendra V. Singh and Joseph Wang. Nano/micromotors for security/defense applications. A review. *Nanoscale*, 7:19377–19389, 2015.

[34] Bernard P Binks. Particles as surfactants–similarities and differences. *Curr. Opin. Colloid Interface Sci.*, 7:21–41, 2002.

[35] Bernard P. Binks and T.S. Horozov, editors. *Colloidal particles at liquid interfaces*. Cambridge University Press, 2006.

[36] Bernard P. Binks. Colloidal particles at a range of fluid-fluid interfaces. *Langmuir*, 33:6947–6963, 2017.

[37] Robert Aveyard, Bernard P. Binks, and John H. Clint. Emulsions stabilised solely by colloidal particles. *Adv. Colloid Interface Sci.*, 100-102:503–546, 2003.

[38] Jie Wu and Guang Hui Ma. Recent studies of pickering emulsions: Particles make the difference. *Small*, pages 4633–4648, 2016.

[39] Tommy S. Horozov. Foams and foam films stabilised by solid particles. *Curr. Opin. Colloid Interface Sci.*, 13:134–140, 2008.

[40] Stephanie Lam, Krassimir P. Velikov, and Orlin D. Velev. Pickering stabilization of foams and emulsions with particles of biological origin. *Curr. Opin. Colloid Interface Sci.*, 19:490–500, 2014.

[41] Michael E. Cates and Paul S. Clegg. Bijels: A new class of soft materials. *Soft Matter*, 4:2132, 2008.

[42] Tobias Bollhorst, Kurosch Rezwan, and Michael Maas. Colloidal capsules: Nano- and microcapsules with colloidal particle shells. *Chem. Soc. Rev.*, 46:2091–2126, 2017.

[43] Edward Bormashenko. Liquid marbles: Properties and applications. *Curr. Opin. Colloid Interface Sci.*, 16:266–271, 2011.

[44] M Lee, E Y Lee, D Lee, and B J Park. Stabilization and fabrication of microbubbles: Applications for medical purposes and functional materials. *Soft Matter*, 11:2067–2079, 2015.

[45] Venkateshwar Rao Dugyala, Santosh V. Daware, and Madivala G. Basavaraj. Shape anisotropic colloids: Synthesis, packing behavior, evaporation driven assembly, and their application in emulsion stabilization. *Soft Matter*, 9:6711–6725, 2013.

[46] Ankit Kumar, Bum Jun Park, Fuquan Tu, and Daeyeon Lee. Amphiphilic Janus particles at fluid interfaces. *Soft Matter*, 9(29):6604–6617, 2013.

[47] Valeria Garbin, John C. Crocker, and Kathleen J. Stebe. Nanoparticles at fluid interfaces: Exploiting capping ligands to control adsorption, stability and dynamics. *J. Colloid Interface Sci.*, 387:1–11, 2012.

[48] Omkar S. Deshmukh, Dirk van den Ende, Martien Cohen Stuart, Frieder Mugele, and Michel H.G. Duits. Hard and soft colloids at fluid interfaces: Adsorption, interactions, assembly & rheology. *Adv. Colloid Interface Sci.*, 222:215–227, 2015.

[49] Armando Maestro, Eduardo Guzmán, Francisco Ortega, and Ramón G. Rubio. Contact angle of micro- and nanoparticles at fluid interfaces. *Curr. Opin. Colloid Interface Sci.*, 19:355–367, 2014.

[50] Lorenzo Botto, Eric P. Lewandowski, Marcello Cavallaro, and Kathleen J. Stebe. Capillary interactions between anisotropic particles. *Soft Matter*, 8:9957–9971, 2012.

[51] M. Oettel and S. Dietrich. Colloidal interactions at fluid interfaces. *Langmuir*, 24:1425–1441, 2008.

[52] Alexander Böker, Jinbo He, Todd Emrick, and Thomas P. Russell. Self-assembly of nanoparticles at interfaces. *Soft Matter*, 3:1231–1248, 2007.

[53] Samuel G. Booth and Robert A W Dryfe. Assembly of nanoscale objects at the liquid/liquid interface. *J. Phys. Chem. C*, 119:23295–23309, 2015.

[54] Alma J. Mendoza, Eduardo Guzman, Fernando Martinez-Pedrero, Hernan Ritacco, Ramon G. Rubio, Francisco Ortega, Victor M. Starov, and Reinhard Miller. Particle laden fluid interfaces: Dynamics and interfacial rheology. *Adv. Colloid Interface Sci.*, 206:303–319, 2014.

[55] Leonard M C Sagis and Peter Fischer. Nonlinear rheology of complex fluid-fluid interfaces. *Curr. Opin. Colloid Interface Sci.*, 19:520–529, 2014.

[56] M. Karbaschi, M. Lotfi, J. Krägel, A. Javadi, D. Bastani, and R. Miller. Rheology of interfacial layers. *Curr. Opin. Colloid Interface Sci.*, 19:514–519, 2014.

[57] Eric Dickinson. Food emulsions and foams: Stabilization by particles. *Curr. Opin. Colloid Interface Sci.*, 15:40–49, 2010.

[58] Yves Chevalier and Marie Alexandrine Bolzinger. Emulsions stabilized with solid nanoparticles: Pickering emulsions. *Colloids Surf., A.*, 439:23–34, 2013.

[59] Marc Pera-Titus, Lo??c Leclercq, Jean Marc Clacens, Floryan De Campo, and V??ronique Nardello-Rataj. Pickering interfacial catalysis for biphasic systems: From emulsion design to green reactions. *Angew. Chemie - Int. Ed.*, 54:2006–2021, 2015.

[60] Bartosz A Grzybowski, Howard A Stone, and George M Whitesides. Dynamic self-assembly of magnetized, millimetre-sized objects rotating at a liquid-air interface. *Nature*, 405:1033–1036, 2000.

[61] Eric Climent, Kyongmin Yeo, Martin R. Maxey, and George E. Karniadakis. Dynamic self-assembly of spinning particles. *J. Fluids Eng.*, 129:379–387, 2007.

[62] Yang Wang, Rose M. Hernandez, David J. Bartlett, Julia M. Bingham, Timothy R. Kline, Ayusman Sen, and Thomas E. Mallouk. Bipolar electrochemical mechanism for the propulsion of catalytic nanomotors in hydrogen peroxide solutions. *Langmuir*, 22:10451–10456, 2006.

[63] J. L. Moran, P. M. Wheat, and J. D. Posner. Locomotion of electrocatalytic nanomotors due to reaction induced charge autoelectrophoresis. *Phys. Rev. E*, 81:065302, jun 2010.

[64] Nicolas Mano and Adam Heller. Bioelectrochemical propulsion. *J. Am. Chem. Soc.*, 127:11574–11575, 2005.

[65] Suk Tai Chang, Vesselin N. Paunov, Dimiter N. Petsev, and Orlin D. Velev. Remotely powered self-propelling particles and micropumps based on miniature diodes. *Nat. Mater.*, 6:235–240, 2007.

[66] Sangtae Kim and Seppo J. Karrila. *Microhydrodynamics: Principles and selected applications*. Dover, New York, 2005.

[67] Michelle Driscoll, Blaise Delmotte, Mena Youssef, Stefano Sacanna, Aleksandar Donev, and Paul Chaikin. Unstable fronts and stable "critters" formed by microrollers. *Nat. Phys.*, 13(April):375–380, 2017.

[68] Antoine Bricard, Jean-Baptiste Caussin, Nicolas Desreumaux, Olivier Dauchot, and Denis Bartolo. Emergence of macroscopic directed motion in populations of motile colloids. *Nature*, 503:95–98, nov 2013.

[69] Daisuke Takagi, Jeremie Palacci, Adam B. Braunschweig, Michael J. Shelley, and Jun Zhang. Hydrodynamic capture of microswimmers into sphere-bound orbits. *Soft Matter*, 10:1784–1789, 2014.

[70] Sambeeta Das, Astha Garg, Andrew I. Campbell, Jonathan Howse, Ayusman Sen, Darrell Velegol, Ramin Golestanian, and Stephen J. Ebbens. Boundaries can steer active Janus spheres. *Nat. Commun.*, 6:8999, 2015.

[71] W E Uspal, M N Popescu, S Dietrich, and M Tasinkevych. Self-propulsion of a catalytically active particle near a planar wall: from reflection to sliding and hovering. *Soft Matter*, 11:434–438, 2015.

[72] Ali Mozaffari, Nima Sharifi-Mood, Joel Koplik, and Charles Maldarelli. Self-diffusiophoretic colloidal propulsion near a solid boundary. *Phys. Fluids*, 28:053107, 2016.

[73] P. Malgaretti, M. N. Popescu, and S. Dietrich. Active colloids at fluid interfaces. *Soft Matter*, 12:4007–4023, 2016.

[74] Giuseppe Boniello, Christophe Blanc, Denys Fedorenko, Mayssa Medfai, Nadia Ben Mbarek, Martin In, Michel Gross, Antonio Stocco, and Maurizio Nobili. Brownian diffusion of a partially wetted colloid. *Nat. Mater.*, 14(9):908–911, 2015.

[75] Joel Koplik and Charles Maldarelli. Diffusivity and hydrodynamic drag of nanoparticles at a vapor-liquid interface. *Phys. Rev. Fluids*, 2:024303, 2017.

[76] Xiaolu Wang, Martin In, Christophe Blanc, Paolo Malgaretti, Maurizio Nobili, and Antonio Stocco. Wetting and orientation of catalytic Janus colloids at the surface of water. *Faraday Discuss.*, 191:305–324, 2016.

[77] Kilian Dietrich, Damian Renggli, Michele Zanini, Giovanni Volpe, Ivo Buttinoni, and Lucio Isa. Two-dimensional nature of the active Brownian motion of catalytic microswimmers at solid and liquid interfaces. *New J. Phys.*, 19:065008, 2017.

[78] Colm P. Kelleher, Rodrigo E. Guerra, Andrew D. Hollingsworth, and Paul M. Chaikin. Phase behavior of charged colloids at a fluid interface. *Phys. Rev. E*, 95(2):022602, 2017.

[79] F. C. Keber, E. Loiseau, T. Sanchez, S. J. DeCamp, L. Giomi, M. J. Bowick, M. C. Marchetti, Z. Dogic, and A. R. Bausch. Topology and dynamics of active nematic vesicles. *Science*, 345:1135–1139, 2014.

[80] Junqi Yuan and Sung Kwon Cho. Bio-inspired micro/mini propulsion at air-water interface: A review. *J. Mech. Sci. Technol.*, 26:3761–3768, 2012.

[81] Véronique Pimienta and Charles Antoine. Self-propulsion on liquid surfaces. *Curr. Opin. Colloid Interface Sci.*, 19:290–299, 2014.

[82] Satoshi Nakata, Masaharu Nagayama, Hiroyuki Kitahata, Nobuhiko J. Suematsu, and Takeshi Hasegawa. Physicochemical design and analysis of self-propelled objects that are characteristically sensitive to environments. *Phys. Chem. Chem. Phys.*, 17:10326–10338, 2015.

[83] Rachita Sharma, Suk Tai Chang, and Orlin D. Velev. Gel-based self-propelling particles get programmed to dance. *Langmuir*, 28:10128–10135, 2012.

[84] L. E. Scriven and C. V. Sternling. The Marangoni effects. *Nature*, 187:186–188, 1960.

[85] Alois Würger. Thermally driven Marangoni surfers. *J. Fluid Mech.*, 752:589–601, 2014.

[86] Hassan Masoud and Howard A. Stone. A reciprocal theorem for Marangoni propulsion. *J. Fluid Mech.*, 741:R4, 2014.

[87] Vahid Vandadi, Saeed Jafari Kang, and Hassan Masoud. Reverse Marangoni surfing. *J. Fluid. Mech*, 811:612–621, 2017.

[88] Hua Zhang, Wentao Duan, Lei Liu, and Ayusman Sen. Depolymerization-powered autonomous motors using biocompatible fuel. *J. Am. Chem. Soc.*, 135:15734–15737, 2013.

[89] Siowling Soh, Kyle J M Bishop, and Bartosz A Grzybowski. Dynamic self-assembly in ensembles of camphor boats. *J. Phys. Chem. B*, 112:10848–10853, sep 2008.

[90] Satoshi Nakata, Yasutaka Iguchi, Sachie Ose, Makiko Kuboyama, Toshio Ishii, and Kenichi Yoshikawa. Self-rotation of a camphor scraping on water: new insight into the old problem. *Langmuir*, 13:4454–4458, 1997.

[91] Natsuhiko Yoshinaga, Ken H. Nagai, Yutaka Sumino, and Hiroyuki Kitahata. Drift instability in the motion of a fluid droplet with a chemically reactive surface driven by Marangoni flow. *Phys. Rev. E - Stat. Nonlinear, Soft Matter Phys.*, 86:016108, 2012.

[92] J. L Anderson. Colloid transport by interfacial forces. *Annu. Rev. Fluid Mech.*, 21:61–99, 1989.

[93] Noy Bassik, Beza T. Abebe, and David H. Gracias. Solvent driven motion of lithographically fabricated gels. *Langmuir*, 24:12158–12163, 2008.

[94] David Okawa, Stefan J Pastine, Alex Zettl, and Jean M J Frechet. Surface tension mediated conversion of light to work surface tension mediated conversion of light to work. *J. Am. Chem. Soc.*, 131:5396–5398, 2009.

[95] Hiroyuki Kitahata, Keita Iida, and Masaharu Nagayama. Spontaneous motion of an elliptic camphor particle. *Phys. Rev. E - Stat. Nonlinear, Soft Matter Phys.*, 87:010901, 2013.

[96] Yui Matsuda, Nobuhiko J. Suematsu, Hiroyuki Kitahata, Yumihiko S. Ikura, and Satoshi Nakata. Acceleration or deceleration of self-motion by the Marangoni effect. *Chem. Phys. Lett.*, 654:92–96, 2016.

[97] Yuko Hayashima, Masaharu Nagayama, and Satoshi Nakata. A camphor grain oscillates while breaking symmetry. *J. Phys. Chem. B*, 105:5353–5357, 2001.

[98] Alvaro Dominguez, P. Malgaretti, M. N. Popescu, and S. Dietrich. Effective interaction between active colloids and fluid interfaces induced by Marangoni flows. *Phys. Rev. Lett.*, 116:078301, 2016.

[99] Hassan Masoud and Michael J. Shelley. Collective surfing of chemically active particles. *Phys. Rev. Lett.*, 112:128304, 2013.

[100] István Lagzi, Siowling Soh, Paul J. Wesson, Kevin P. Browne, and Bartosz A. Grzybowski. Maze solving by chemotactic droplets. *JACS*, 132:1198–1199, 2010.

[101] Kohta Suzuno, Daishin Ueyama, Michal Branicki, Rita Tóth, Artur Braun, and István Lagzi. Maze solving using fatty acid chemistry. *Langmuir*, 30:9251–9255, 2014.

[102] Dimitris Stamou, Claus Duschl, and Diethelm Johannsmann. Long-range attraction between colloidal spheres at the air-water interface: The consequence of an irregular meniscus. *Phys. Rev. E*, 62:5263–5272, 2000.

[103] Peter A. Kralchevsky and Kuniaki Nagayama. Capillary interactions between particles bound to interfaces, liquid films and biomembranes. *Adv. Colloid Interface Sci.*, 85:145–192, 2000.

[104] Krassimir D Danov, Peter A Kralchevsky, Boris N Naydenov, and Günter Brenn. Interactions between particles with an undulated contact line at a fluid interface : Capillary multipoles of arbitrary order. *J. Colloid Interface Sci.*, 287:121–134, 2005.

[105] Ned Bowden, Insung S Choi, Bartosz A Grzybowski, and George M Whitesides. Mesoscale self-assembly of hexagonal plates using lateral capillary forces : Synthesis using the "capillary bond". *J. Am. Chem. Soc.*, 121:5373–5391, 1999.

[106] Dominic Vella and L. Mahadevan. The "Cheerios effect". *Am. J. Phys.*, 73:817–825, 2005.

[107] J. C. Loudet, A. M. Alsayed, J. Zhang, and A. G. Yodh. Capillary interactions between anisotropic colloidal particles. *Phys. Rev. Lett.*, 94:018301, 2005.

[108] Teresa Brugarolas, Bum Jun Park, Myung Han Lee, and Daeyeon Lee. Generation of amphiphilic Janus bubbles and their behavior at an air-water interface. *Adv. Funct. Mater.*, 21:3924–3931, 2011.

[109] Bum Jun Park, Teresa Brugarolas, and Daeyeon Lee. Janus particles at an oil–water interface. *Soft Matter*, 7:6413–6413, 2011.

[110] Lu Yao, Nima Sharifi-Mood, Iris B. Liu, and Kathleen J. Stebe. Capillary migration of microdisks on curved interfaces. *J. Colloid Interface Sci.*, 449:436–442, 2014.

[111] N. Sharifi-mood, I. B. Liu, and K. J. Stebe. Curvature capillary migration of microspheres. *Soft Matter*, 11:6768–6779, 2015.

[112] Iris B Liu, Nima Sharifi-mood, and Kathleen J Stebe. Curvature-driven assembly in soft matter. *Philos. Trans. R. Soc. A*, 374:20150133, 2016.

[113] Dmitry Ershov, Joris Sprakel, Jeroen Appel, Martien A Cohen Stuart, and Jasper van der Gucht. Capillarity-induced ordering of spherical colloids on an interface with anisotropic curvature. *Proc. Natl. Acad. Sci.*, 110:9220–9224, 2013.

[114] Gary B Davies, Timm Krüger, Peter V Coveney, Jens Harting, and Fernando Bresme. Interface deformations affect the orientation transition of magnetic ellipsoidal particles adsorbed at fluid-fluid interfaces. *Soft matter*, 10:6742–6478, 2014.

[115] Hossein Rezvantalab and Shahab Shojaei-Zadeh. Tilting and tumbling of Janus nanoparticles at sheared interfaces. *ACS Nano*, 10:5354–5361, 2016.

[116] J. Yan, S. C. Bae, and S. Granick. Rotating crystals of magnetic Janus colloids. *Soft Matter*, 11:147–153, 2015.

[117] Gary B. Davies, Timm Krüger, Peter V. Coveney, Jens Harting, and Fernando Bresme. Assembling ellipsoidal particles at fluid interfaces using switchable dipolar capillary interactions. *Adv. Mater.*, 26:6715–6719, 2014.

[118] Hossein Rezvantalab, Kevin W. Connington, and Shahab Shojaei-Zadeh. Shear-induced interfacial assembly of Janus particles. *Phys. Rev. Fluid*, 1:074205, 2016.

[119] Denise Wong, Iris B. Liu, Edward B. Steager, Kathleen J. Stebe, and Vijay Kumar. Directed micro assembly of passive particles at fluid interfaces using magnetic robots. *2016 International Conference on Manipulation, Automation and Robotics at Small Scales (MARSS)*, pages 1–6, 2016.

[120] Junqi Yuan, Jian Feng, and Sung Kwon Cho. Cheerios effect controlled by electrowetting. *Langmuir*, 31:8502–8511, 2015.

[121] Thamarasseril Vijayan Vinay, Theneyur Narayanaswamy Banuprasad, Sajan Daniel George, Soney Varghese, and Subramanyan Namboodiri Varanakkottu. Additive-free tunable transport and assembly of floating objects at water-air interface using bubble-mediated capillary forces. *Adv. Mater. Interfaces*, 4:1601231, 2017.

[122] Galien Grosjean, Maxime Hubert, and Nicolas Vandewalle. Magnetocapillary self-assemblies: locomotion and micromanipulation along a liquid interface. *Adv. Colloid Interface Sci.*, page In press, 2017.

[123] G. Lumay, N. Obara, F. Weyer, and N. Vandewalle. Self-assembled magnetocapillary swimmers. *Soft Matter*, 9:2420–2425, 2013.

[124] A. Snezhko, I. S. Aranson, and W. K. Kwok. Surface wave assisted self-assembly of multidomain magnetic structures. *Phys. Rev. Lett.*, 96(7):078701, 2006.

[125] Guillaume Lagubeau, Galien Grosjean, Alexis Darras, Geoffroy Lumay, Maxime Hubert, and Nicolas Vandewalle. Statics and dynamics of magnetocapillary bonds. *Phys. Rev. E*, 93:053117, 2016.

[126] M. Belkin, A. Snezhko, I. S. Aranson, and W. K. Kwok. Driven magnetic particles on a fluid surface: Pattern assisted surface flows. *Phys. Rev. Lett.*, 99:158301, 2007.

[127] William T. M. Irvine, Vincenzo Vitelli, and Paul M. Chaikin. Pleats in crystals on curved surfaces. *Nature*, 468:947–951, 2010.

[128] Vanesa Magar, Tomonobu Goto, and T. J. Pedley. Nutrient uptake by a self-propelled steady squirmer. *Q. J. Mech. Appl. Math.*, 56:65–91, 2003.

[129] Anne Laure Fameau, Adrian Carl, Arnaud Saint-Jalmes, and Regine Von Klitzing. Responsive aqueous foams. *ChemPhysChem*, 16:66–75, 2015.

[130] Syuji Fujii and Yoshinobu Nakamura. Stimuli-responsive bubbles and foams stabilized with solid particles. *Langmuir*, 33:7365–7379, 2017.

[131] Sonia Melle, Mauricio Lask, and Gerald G. Fuller. Pickering emulsions with controllable stability. *Langmuir*, 21(6):2158–2162, 2005.

[132] Andreas Kaiser, Tingting Liu, Walter Richtering, and Annette M. Schmidt. Magnetic capsules and Pickering emulsions stabilized by coreshell particles. *Langmuir*, 25:7335–7341, 2009.

[133] Jun Zhou, Xiuying Qiao, Bernard P Binks, Kang Sun, Mingwen Bai, Yunlong Li, and Yi Liu. Magnetic Pickering emulsions stabilized by Fe_3O_4 nanoparticles. *Langmuir*, 27:3308–3316, 2011.

[134] Stephanie Lam, Elena Blanco, Stoyan K Smoukov, Krassimir P Velikov, and Orlin D Velev. Magnetically responsive pickering foams. *J. Am. Chem. Soc.*, 133(35):13856–13859, 2011.

[135] Elena Blanco, Stephanie Lam, Stoyan K. Smoukov, Krassimir P. Velikov, Saad A. Khan, and Orlin D. Velev. Stability and viscoelasticity of magneto-pickering foams. *Langmuir*, 29(32):10019–10027, 2013.

[136] Fuquan Tu, Bum Jun Park, and Daeyeon Lee. Thermodynamically stable emulsions using Janus dumbbells as colloid surfactants. *Langmuir*, 29:12679–12687, 2013.

[137] Roger S M Rikken, Roeland J M Nolte, Jan C Maan, Jan C M van Hest, Daniela a Wilson, and Peter C M Christianen. Manipulation of micro- and nanostructure motion with magnetic fields. *Soft matter*, 10:1295–1308, 2014.

[138] Nicole Pamme. Magnetism and microfluidics. *Lab on a Chip*, 1(6):24–28, 2006.

[139] Tsunehisa Kimura, Masashi Yoshino, Tsutomu Yamane, Masafumi Yamato, and Masayuki Tobita. Uniaxial alignment of the smallest diamagnetic susceptibility axis using time-dependent magnetic fields. *Langmuir*, 20(14):5669–5672, 2004.

[140] P. Weiss and G. Foëx. *Le Magnétisme, par Pierre Weiss et Gabriel Foëx. 69 figures. 2e édition, revue et corrigée.* libr. Armand Colin, 1931.

[141] Srikanth Singamaneni and Valery Bliznyuk. Fabrication of Ni nanoparticles and their size-selective self-assembly into chains under external magnetic field. *Applied Physics Letters*, 87:162511, 2005.

[142] Alexey Snezhko and Igor S Aranson. Magnetic manipulation of self-assembled colloidal asters. *Nature materials*, 10(9):698–703, 2011.

[143] Jeffrey M. Isner, Toyoaki Murohara, Bernhard Witzenbichler, Takayuki Asahara, Marcy Silver, Tong Li, Gina Schatteman, Rien van der Zee, and Alison Sullivan. Isolation of Putative Progenitor Endothelial Cells for Angiogenesis. *Science*, 275(5302):964–966, 2002.

[144] M. M. Davis, J. G. Berbee, W. Yu, W. Xiao, D. E. Huber, R. W. Davis, A. A. Powell, A. H. Talasaz, S. S. Jeffrey, R. F. Pease, K.-H. Roh, and M. N. Mindrinos. Isolating highly enriched populations of circulating epithelial cells and other rare cells from blood using a magnetic sweeper device. *Proceedings of the National Academy of Sciences*, 106(10):3970–3975, 2009.

[145] Christopher Brennen and Howard Winet. Fluid Mechanics of Propulsion by Cilia and Flagella. *Annual Review of Fluid Mechanics*, 9(Lehninger 1971):339–398, 1977.

[146] Eric Lauga and Thomas R. Powers. The hydrodynamics of swimming microorganisms. *Reports on Progress in Physics*, 72(9), 2009.

[147] Maria M. Tirado and José Garcia De La Torre. Rotational dynamics of rigid, symmetric top macromolecules. Application to circular cylinders. *The Journal of Chemical Physics*, 73(4):1986–1993, 1980.

[148] Manoel Manghi, Xaver Schlagberger, Yong Woon Kim, and Roland R. Netz. Hydrodynamic effects in driven soft matter. *Soft Matter*, 2(8):653–668, 2006.

[149] A.J. AJ Goldman, RG G R.G. Cox, Howard Brenner, and A J Goldmans. Slow viscous motion of a sphere parallel to a plane wallI Motion through a quiescent fluid. *Chem. Eng. Sci.*, 22:637–651, 1967.

[150] F. Martínez-Pedrero and P. Tierno. Advances in colloidal manipulation and transport via hydrodynamic interactions. *Journal of Colloid and Interface Science*, 519:296–311, 2018.

[151] Matthias Schmelz and Ronny Stolz. *Superconducting Quantum Interference Device (SQUID) Magnetometers*, pages 279–311. Springer International Publishing, Cham, 2017.

[152] James W. Swan and John F. Brady. Simulation of hydrodynamically interacting particles near a no-slip boundary. *Physics of Fluids*, 19(11), 2007.

[153] Pietro Tierno, Josep Claret, Francesc Sagués, and Andrejs Cãbers. Overdamped dynamics of paramagnetic ellipsoids in a precessing magnetic field. *Physical Review E - Statistical, Nonlinear, and Soft Matter Physics*, 79(2):021501, 2009.

[154] J. J. Abbott, K. E. Peyer, M. C. Lagomarsino, L. Zhang, L. Dong, I. K. Kaliakatsos, and B. J. Nelson. How Should Microrobots Swim? *The International Journal of Robotics Research*, 28:1434–1447, 2009.

[155] Edwin W.H. Jager, Olle Inganäs, and Ingemar Lundström. Microrobots for micrometer-size objects in aqueous media: Potential tools for single-cell manipulation. *Science*, 288(5475):2335–2338, 2000.

[156] Jing Yan, Moses Bloom, Sung Chul Bae, Erik Luijten, and Steve Granick. Linking synchronization to self-assembly using magnetic Janus colloids. *Nature*, 491(7425):578–581, 2012.

[157] Hui Xie, Mengmeng Sun, Xinjian Fan, Zhihua Lin, Weinan Chen, Lei Wang, Lixin Dong, and Qiang He. Reconfigurable magnetic microrobot swarm: Multimode transformation, locomotion, and manipulation. *Science Robotics*, 4(28):eaav8006, 2019.

[158] P G De Gennes. American Association for the Advancement of Science (Continued). *The American Naturalist*, 23(274):935–939, 2002.

[159] Stephen M. Anthony, Minsu Kim, and Steve Granick. Single-particle tracking of janus colloids in close proximity. *Langmuir*, 24(13):6557–6561, 2008.

[160] Jaehyuck Choi, Yihua Zhao, Deying Zhang, Shu Chien, and Y. H. Lo. Patterned fluorescent particles as nanoprobes for the investigation of molecular interactions. *Nano Letters*, 3(8):995–1000, 2003.

[161] Su Na Yin, Cai Feng Wang, Zi Yi Yu, Jing Wang, Si Si Liu, and Su Chen. Versatile bifunctional magnetic-fluorescent responsive Janus supraballs towards the flexible bead display. *Advanced Materials*, 23:2915–2919, 2011.

[162] Caleb J. Behrend, Jeffrey N. Anker, Brandon H. McNaughton, Murphy Brasuel, Martin A. Philbert, and Raoul Kopelman. Metal-capped brownian and magnetically modulated optical nanoprobes (MOONs): Micromechanics in chemical and biological microenvironments. *Journal of Physical Chemistry B*, 108(29):10408–10414, 2004.

[163] Andreas Walther and Axel H. E. Muller. Janus Particles : Synthesis , Self-Assembly , Physical Properties , and Applications. *Chem. Rev.*, 113:5194–5261, 2013.

[164] Takuya Tanaka, Reiko Nakatsuru, Yoshimi Kagari, Naohiko Saito, and Masayoshi Okubo. Effect of molecular weight on the morphology of polystyrene/ poly(methyl methacrylate) composite particles prepared by the solvent evaporation method. *Langmuir*, 24(21):12267–12271, 2008.

[165] Naohiko Saito, Yoshimi Kagari, and Masayoshi Okubo. Effect of colloidal stabilizer on the shape of polystyrene/poly(methyl methacrylate) composite particles prepared in aqueous medium by the solvent evaporation method. *Langmuir*, 22(22):9397–9402, 2006.

[166] Naohiko Saito, Yoshimi Kagari, and Masayoshi Okubo. Revisiting the morphology development of solvent-swollen composite polymer particles at thermodynamic equilibrium. *Langmuir*, 23(11):5914–5919, 2007.

[167] Shang Hsiu Hu and Xiaohu Gao. Nanocomposites with spatially separated functionalities for combined imaging and magnetolytic therapy. *Journal of the American Chemical Society*, 132(21):7234–7237, 2010.

[168] Oriol Güell, Francesc Sagués, and Pietro Tierno. Magnetically Driven Janus Micro-Ellipsoids Realized via Asymmetric Gathering of the Magnetic Charge. pages 3674–3679, 2011.

[169] Stefano Sacanna, Laura Rossi, and David J. Pine. Magnetic click colloidal assembly. *Journal of the American Chemical Society*, 134(14):6112–6115, 2012.

[170] Liang Hong, Shan Jiang, and Steve Granick. Simple method to produce janus colloidal particles in large quantity. *Langmuir*, 22(23):9495–9499, 2006.

[171] Shan Jiang and Steve Granick. Controlling the geometry (Janus balance) of amphiphilic colloidal particles. *Langmuir*, 24(17):2438–2445, 2008.

[172] Irene Sinn, Paivo Kinnunen, Shao Ning Pei, Roy Clarke, Brandon H. McNaughton, and Raoul Kopelman. Magnetically uniform and tunable Janus particles. *Appl. Phys. Lett.*, 98(2):024101, 2011.

[173] Bin Ren, Aleksey Ruditskiy, Jung Hun Song, and Ilona Kretzschmar. Assembly behavior of iron oxide-capped Janus particles in a magnetic field. *Langmuir*, 28(2):1149–1156, 2011.

[174] Olivier Cayre, Vesselin N. Paunov, and Orlin D. Velev. Fabrication of asymmetrically coated colloid particles by microcontact printing techniques. *Journal of Materials Chemistry*, 13(10):2445–2450, 2003.

[175] Shan Jiang and Steve Granick. A simple method to produce trivalent colloidal particles. *Langmuir*, 25(16):8915–8918, 2009.

[176] H. Takei and N. Shimizu. Gradient Sensitive Microscopic Probes Prepared by Gold Evaporation and Chemisorption on Latex Spheres. *Langmuir*, 13(7):1865–1868, 1997.

[177] Shengrong Ye and R. Lloyd Carroll. Design and fabrication of bimetallic colloidal "janus" particles. *ACS Applied Materials and Interfaces*, 2(3):616–620, 2010.

[178] Daisuke Suzuki and Haruma Kawaguchi. Janus particles with a functional gold surface for control of surface plasmon resonance. *Colloid and Polymer Science*, 284(12):1471–1476, 2006.

[179] Stoyan K. Smoukov, Sumit Gangwal, Manuel Marquez, and Orlin D. Velev. Reconfigurable responsive structures assembled from magnetic Janus particles. *Soft Matter*, 5:1285–1292, 2009.

[180] Jung Hun Song, David Harbottle, and Jae W. Lee. Rapid assembly of colloidal monolayer for the synthesis of surface anisotropic particles. *ACS Applied Materials and Interfaces*, 3(7):2393–2397, 2011.

[181] J. G. Gibbs and Y. P. Zhao. Autonomously motile catalytic nanomotors by bubble propulsion. *Applied Physics Letters*, 94(16):3–6, 2009.

[182] Byron D. Gates, Daniel B. Wolfe, George M. Whitesides, J. Christopher Love, and Kateri E. Paul. Fabrication and Wetting Properties of Metallic Half-Shells with Submicron Diameters. *Nano Letters*, 2(8):891–894, 2002.

[183] Yba Cu and O Mgo. Two- and three-dimensional arrays of magnetic microspheres. *Journal of materials research*, pages 2–5, 1999.

[184] Xing Yi Ling, In Yee Phang, Canet Acikgoz, M. Deniz Yilmaz, Mark A. Hempenius, G. Julius Vancso, and Jurriaan Huskens. Janus particles with controllable patchiness and their chemical functionalization and supramolecular assembly. *Angewandte Chemie - International Edition*, 48(41):7677–7682, 2009.

[185] Jing-qin Cui, Ilona Kretzschmar, Recei V June, In Final, and Form August. Surface-Anisotropic Polystyrene Spheres by Electroless Deposition. (18):8281–8284, 2006.

[186] Chien Chih Lin, Chu Wei Liao, Yi Cheng Chao, and Changshu Kuo. Fabrication and characterization of asymmetric Janus and ternary particles. *ACS Applied Materials and Interfaces*, 2(11):3185–3191, 2010.

[187] Marla D. McConnell, Matthew J. Kraeutler, Shu Yang, and Russell J. Composto. Patchy and multiregion Janus particles with tunable optical properties. *Nano Letters*, 10(2):603–609, 2010.

[188] Paivo Kinnunen, Irene Sinn, Brandon H. McNaughton, and Raoul Kopelman. High frequency asynchronous magnetic bead rotation for improved biosensors. *Applied Physics Letters*, 97(22):1–4, 2010.

[189] Bradley J. Nelson, Ioannis K. Kaliakatsos, and Jake J. Abbott. Microrobots for Minimally Invasive Medicine. *Annu. Rev. Biomed. Eng.*, 12(1):55–85, 2010.

[190] Koohee Han, C. Wyatt Shields, and Orlin D. Velev. Engineering of Self-Propelling Microbots and Microdevices Powered by Magnetic and Electric Fields. *Adv. Funct. Mater.*, page 1705953, 2018.

[191] Michael P. Kummer, Jake J. Abbott, Bradley E. Kratochvil, Ruedi Borer, Ali Sengul, and Bradley J. Nelson. Octomag: An electromagnetic system for 5-DOF wireless micromanipulation. *IEEE Trans. Robot.*, 26(6):1006–1017, 2010.

[192] Rémi Dreyfus, Jean Baudry, Marcus L Roper, Marc Fermigier, Howard A Stone, and Jérôme Bibette. Microscopic artificial swimmers. *Nature*, 437(7060):862–865, 2005.

[193] Koohee Han, C. Wyatt Shields, Nidhi M. Diwakar, Bhuvnesh Bharti, Gabriel P. López, and Orlin D. Velev. Sequence-encoded colloidal origami and microbot assemblies from patchy magnetic cubes. *Sci. Adv.*, 3(8):e1701108, 2017.

[194] Li Zhang, Jake J. Abbott, Lixin Dong, Bradley E. Kratochvil, Dominik Bell, and Bradley J. Nelson. Artificial bacterial flagella: Fabrication and magnetic control. *Appl. Phys. Lett.*, 94(6):064107, 2009.

[195] Ambarish Ghost and Peer Fischer. Controlled propulsion of artificial magnetic nanostructured propellers. *Nano Lett.*, 9(6):2243–2245, 2009.

[196] Wenjie Fei, Yang Gu, and Kyle J.M. Bishop. Active colloidal particles at fluid-fluid interfaces. *Curr. Opin. Colloid Interface Sci.*, 32:57–68, 2017.

[197] Qingguang Xie, Gary B. Davies, and Jens Harting. Direct Assembly of Magnetic Janus Particles at a Droplet Interface. *ACS Nano*, 11(11):11232–11239, 2017.

[198] Randall M. Erb, Nathan J. Jenness, Robert L. Clark, and Benjamin B. Yellen. Towards holonomic control of Janus particles in optomagnetic traps. *Adv. Mater.*, 21(47):4825–4829, 2009.

[199] Bin Ren, Aleksey Ruditskiy, Jung Hun Song, and Ilona Kretzschmar. Assembly behavior of iron oxide-capped Janus particles in a magnetic field. *Langmuir*, 28(2):1149–1156, 2012.

[200] Kwahun Lee, Yi Yi, and Yan Yu. Remote Control of T Cell Activation Using Magnetic Janus Particles. *Angew. Chem. Int. Ed.*, 55(26):7384–7387, 2016.

[201] D. S. Sivia and J. Skilling. *Data Analysis: A Bayesian Tutorial*. Oxford University Press, New York, 2$^{\text{nd}}$ edition, 2006.

[202] John Salvatier, Thomas Wiecki, and Christopher Fonnesbeck. Probabilistic Programming in Python using PyMC. *PeerJ Comput. Sci.*, 2:e55, 2016.

[203] D. Langevin. Influence of interfacial rheology on foam and emulsion properties. *Adv. Colloid Interface Sci.*, 88(1-2):209–222, 2000.

[204] KyuHan Kim, Siyoung Q. Choi, Joseph A. Zasadzinski, and Todd M. Squires. Interfacial microrheology of DPPC monolayers at the airwater interface. *Soft Matter*, 7(17):7782–7789, 2011.

[205] S. Sacanna, L. Rossi, and A. P. Philipse. Oil-in-water emulsification induced by ellipsoidal hematite colloids: Evidence for hydrolysis-mediated self-assembly. *Langmuir*, 23(20):9974–9982, 2007.

[206] Sven Reynaert, Paula Moldenaers, and Jan Vermant. Control over Colloidal Aggregation in Monolayers of Latex Particles at the Oil–Water Interface. *Langmuir*, 22(11):4936–4945, 2006.

[207] M. E. O'neill. A slow motion of viscous liquid caused by a slowly moving solid sphere. *Mathematika*, 11(2):67–74, 1964.

[208] WR W.R. Dean and ME M.E. O'Neill. A slow motion of viscous liquid caused by the rotation of a solid sphere. *Mathematika*, 10(6):13–24, 1963.

[209] Wenjie Fei, Michelle M. Driscoll, Paul M. Chaikin, and Kyle J. M. Bishop. Magneto-capillary dynamics of amphiphilic Janus particles at curved liquid interfaces. *Soft Matter*, 14(23):4661–4665, 2018.

[210] Changzhu Wu, Shuo Bai, Marion B. Ansorge-Schumacher, and Dayang Wang. Nanoparticle cages for enzyme catalysis in organic media. *Advanced Materials*, 23(47):5694–5699, 2011.

[211] Adrie J.J. Straathof. Enzymatic catalysis via liquid-liquid interfaces. *Biotechnology and Bioengineering*, 83(4):371–375, 2003.

[212] Gi Seok Jeong, Seok Chung, Chang-Beom Kim, and Sang-Hoon Lee. Applications of micromixing technology. *Analyst*, 135:460–473, 2010.

[213] Nam-Trung Nguyen and Zhigang Wu. Micromixers—a review. *Journal of Micromechanics and Microengineering*, 15(2):R1–R16, dec 2004.

[214] Nicole Pamme. Magnetism and microfluidics. *Lab Chip*, 6:24–38, 2006.

[215] Nam-Trung Nguyen. Micro-magnetofluidics: interactions between magnetism and fluid flow on the microscale. *Microfluidics and Nanofluidics*, 12(1):1–16, Jan 2012.

[216] Boon M. Teo, Su Kyung Suh, T. Alan Hatton, Muthupandian Ashokkumar, and Franz Grieser. Sonochemical Synthesis of Magnetic Janus Nanoparticles. *Langmuir*, 27(1):30–33, 2011.

[217] Liang Hsuan Lu, Kee Suk Ryu, and Chang Liu. A magnetic microstirrer and array for microfluidic mixing. *Journal of Microelectromechanical Systems*, 11(5):462–469, 2002.

[218] Sibani Lisa Biswal and Alice P. Gast. Micromixing with linked chains of paramagnetic particles. *Analytical Chemistry*, 76(21):6448–6455, 2004.

[219] Tamal Roy, Ashok Sinha, Sayan Chakraborty, Ranjan Ganguly, and Ishwar K. Puri. Magnetic microsphere-based mixers for microdroplets. *Physics of Fluids*, 21(2), 2009.

[220] Po Ki Yuen, Guangshan Li, Yijia Bao, and Uwe R. Mller. Microfluidic devices for fluidic circulation and mixing improve hybridization signal intensity on dna arrays. *Lab Chip*, 3:46–50, 2003.

[221] Xin Zhou, Changyou Chen, Changyan Cao, Tao Song, Hengquan Yang, and Weiguo Song. Enhancing reaction rate in a pickering emulsion system with natural magnetotactic bacteria as nanoscale magnetic stirring bars. *Chem. Sci.*, 9:2575–2580, 2018.

[222] Steven Crossley, Jimmy Faria, Min Shen, and Daniel E. Resasco. Solid nanoparticles that catalyze biofuel upgrade reactions at the water/oil interface. *Science*, 327(5961):68–72, 2010.

[223] Philip Wägli, Yu Chi Chang, Alexandra Homsy, Lubos Hvozdara, Hans Peter Herzig, and Nico F. De Rooij. Microfluidic droplet-based liquid-liquid extraction and on-chip IR spectroscopy detection of cocaine in human saliva. *Analytical Chemistry*, 85(15):7558–7565, 2013.

[224] Cong Xu and Tingliang Xie. Review of Microfluidic Liquid-Liquid Extractors. *Industrial and Engineering Chemistry Research*, 56(27):7593–7622, 2017.

[225] James Diebel. Representing attitude: Euler angles, unit quaternions, and rotation vectors. *Matrix*, 58:1–35, 2006.

[226] Allan M. Brooks, Syeda Sabrina, and Kyle J. M. Bishop. Shape-directed dynamics of active colloids powered by induced-charge electrophoresis. *Proc. Natl. Acad. Sci.*, 115(6):E1090–E1099, 2018.

[227] J. G. Lee, A. M. Brooks, W. A. Shelton, K. J. M. Bishop, and B. Bharti. Directed propulsion of spherical particles along 3D helical trajectories. *Nat. Commun.*, page revision submitted, 2019.

Appendix

Reprint Permission Letters

Chapter 1: Active colloidal particles at fluid-fluid interfaces

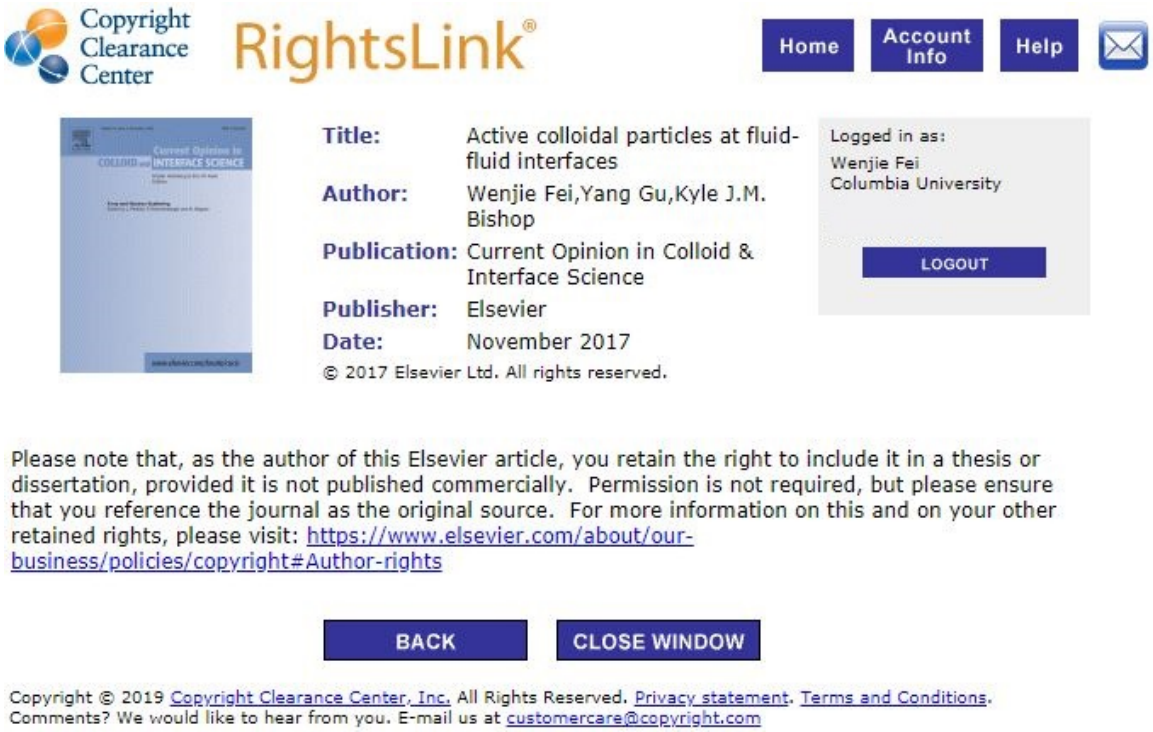

Copyright Clearance Center RightsLink®

Home | Account Info | Help

Title:	Active colloidal particles at fluid-fluid interfaces
Author:	Wenjie Fei,Yang Gu,Kyle J.M. Bishop
Publication:	Current Opinion in Colloid & Interface Science
Publisher:	Elsevier
Date:	November 2017

Logged in as:
Wenjie Fei
Columbia University

LOGOUT

Please note that, as the author of this Elsevier article, you retain the right to include it in a thesis or dissertation, provided it is not published commercially. Permission is not required, but please ensure that you reference the journal as the original source. For more information on this and on your other retained rights, please visit: https://www.elsevier.com/about/our-business/policies/copyright#Author-rights

BACK | CLOSE WINDOW

Chapter 3: Magneto-capillary dynamics of amphiphilic Janus particles at curved liquid interfaces

Magneto-capillary dynamics of amphiphilic Janus particles at curved liquid interfaces

W. Fei, M. M. Driscoll, P. M. Chaikin and K. J. M. Bishop, *Soft Matter*, 2018, **14**, 4661
DOI: 10.1039/C8SM00518D